UNIVERSITY OF CALIFORNIA
RIVERSIDE

Optical Spectroscopy of Positronium Atoms

A Dissertation submitted in partial satisfaction
of the requirements for the degree of

Doctor of Philosophy

in

Physics

by

Tomu Hisakado

December 2014

Dissertation Committee:

Dr. Harry W.K. Tom, Chairperson
Dr. Allen P. Mills Jr.
Dr. Umar Mohideen

The Dissertation of Tomu Hisakado is approved:

_____

_____

_____

Committee Chairperson

University of California, Riverside

ABSTRACT OF THE DISSERTATION

Optical Spectroscopy of Positronium Atoms

by

Tomu Hisakado

Doctor of Philosophy, Graduate Program in Physics
University of California, Riverside, December 2014
Dr. Harry W.K. Tom, Chairperson

Single shot positronium annihilation lifetime spectroscopy (SSPALS) is a technique that records 1×10^7 positronium (Ps) atoms annihilating into gamma rays in a single shot from a positron accumulator. Here, SSPALS is combined with ns tunable lasers to study the electronic structure and emission of Ps atoms from solid surfaces. In our experiment the injection of a high density positron pulse into a target surface produces Ps atoms in vacuum which interacts immediately with the pulsed dye laser at 0.16T at 243nm. In our investigation the Ps kinetic energy along the surface of the sample decreased with increasing implantation energies and a lower limit of E_x=42±3meV was discovered. The lower limit of the Ps kinetic energies corresponds to the region in which the Ps de Broglie wavelength approaches the pore diameters of the target sample. As a result a classical model can no longer be used to describe the energy

loss mechanism. Instead we find the lower limit values in agreement with the quantum confinement model.

In additional studies, the excitation of the 1S-2P transition for Ps was explored in the Paschen Back Regime (high magnetic field) of 2T. This investigation has found that Zeeman mixing of the 2P states is reduced in high magnetic fields. In the event of reduced mixing in the 2P state, which reduces conversion of triplet state Ps atoms into singlet state Ps atoms, this may result in the possibility of laser cooling Ps atoms using multiple pulsed laser events. We also measured the positronium speed distribution perpendicular to the sample using copper and silicon as our target with time of flight. We used a two step, two photon excitation to the Rydberg states to enable single Rydberg atom annihilation to be detected using a multi-channel plate located 1.7m away from the target surface. We observed the Ps atom's kinetic energy to have a thermal Maxwell-Boltzmann speed distribution centered around 350,000 m/s, which is non-monoenergetic. The kinetic energies were measured perpendicular to the sample and the data demonstrates the need for further studies of Ps kinetic energies perpendicular and parallel to the sample.

Contents

List of Tables

List of Figures

Chapter 1
Introduction

1.1 Introduction of Positronium

Antimatter is composed of particles with the same mass but opposite charge of ordinary matter. When matter and antimatter come together annihilation occurs and energy is released in the form of high energy photons, neutrinos, and other lower mass particles and antiparticles. The simplest form of antimatter is the formation of a positron and an electron, called the positronium(Ps) atom. By implanting positron's into solid surfaces the positron will thermalize and diffuse to the surface, picking up an electron at the surface/bulk and forming Ps once in vacuum. The Ps atom in the ground state is made up of different spin states, with both the electron and positron contributing its own spin value of ½ to the total spin state of the atom. With the superposition of the electron and positron spin orientations there exists only two total spin states. The longer lived triplet S=1 Ps atom and the shorter lived S=0 singlet Ps atom. The different orientations of the total spin states for S=1 are,

$$|\uparrow\uparrow\rangle$$

$$\frac{1}{\sqrt{2}}(|\uparrow\downarrow\rangle + |\downarrow\uparrow\rangle \quad \text{S=1 (Total) , Triplet}$$

$$|\downarrow\downarrow\rangle$$

and the singlet spin configuration is

$$\frac{1}{\sqrt{2}}(|\uparrow\downarrow\rangle - |\downarrow\uparrow\rangle \text{S= 0 (total) , Singlet}$$

The arrows in the bra and ket notation represent the spin orientations of the electron and the positron. The ortho-Positronium atom(S=1),o-Ps, and the para-Positronium atom (S=0),p-Ps, once in vacuum decay quickly by gamma ray annihilation within 142ns and 125ps, relatively speaking. Each decay event has a larger "chance" of producing three gamma rays for o-Ps annihilation and two gamma rays for the p-Ps annihilation. Next a brief history of the positron will be discussed.

The positron was first theoretically predicted by Dirac between 1928 and 1933 when he interpreted the possibility of having negative energies in the solution of the relativistic Dirac equation. Dirac pointed out, with the suggestion from Oppenhiemer[1], that an unoccupied state exists in the negative energy states, and this "hole" would have the same mass but opposite charge to an electron[2].

C.Y. Chao had next observed high energy gamma rays originating from heavy elements [3], but was not aware at the time the true origins of the event. In 1933 the positron was discovered by Anderson and revealed that the gamma rays were due to electron- positron annihilation. The observation took place in C. D. Anderson's cloud chamber in 1933[4] for which he won the Nobel Prize in Physics in 1936.

Later in 1951 the longer lived Ps atoms were first discovered by Martin Deutsch when he measured a slower decay rate of Ps atoms in nitrogen gas, which indicated triplet state Ps atom formation[5]. Deutsch was nominated for the Nobel Prize in Physics in 1956 for his discovery of the Ps atom. The long lifetime of Ps formation was reduced

in other gases, which indicated a low Ps formation rate. A list of most of the Ps experiments done between 1951 and 1988 is covered in a review article by Shultz and Lynn[6]. The review article has a table providing the experiments done chronologically that measured the time scales of positron interaction with surfaces, the development of a slow positron beam, positron sources and moderator efficiencies, scattering effects, and materials for Ps formation. Some of these important topics will be mentioned later in the chapter High Density Ps Pulser.

The optical experiments of Ps atoms will be reviewed next. The ground state Ps atom, upon photon excitation from the ground state to the 2p state will decay radiatively back down to the ground state with a mean lifetime of 3.2 ns. The experiments performed were mainly focused on the Alpha Lyman Transition, 1S-2P. The energy levels are half that of the hydrogen atom due to the reduced mass of the Ps atom. The expression is given as

$$E = -\frac{R}{2n^2}$$

where R is the Rydberg constant and is equal to [7].

$$R = \frac{m_e e^4}{8\varepsilon_o^2 h^3 c} = 1.097\ 373\ 156\ 8539(55) \times 10^7 m^{-1}$$

In our experiments the Ps atoms travel 6-8mm from the surface of the target before annihilation. In vacuum the Ps atoms will then quickly decay into two or three gamma rays within ~0-300ns. The light source that we used is a pulsed dye laser with a bandwidth that is relatively small and continuously tunable having a FWHM of 4-7ns.

The relative time jitter is ± 1ns between the laser pulse and the positron pulse. The high density positron pulse produces $2 \times 10^7 e^+$'s within a 20ns – 0.25ns adjustable pulse width. The positron pulse then is injected into a solid surface with a diameter of less than 0.25mm.

By performing a two step, two photon excitation into high n Rydberg states the Ps atom can be measured using a multichannel plate, and we can measure, for example, the probability of transitions approaching the term limit for n greater than 50. Another possible experiment is tuning the wavelength across the 1S-2P transition and measuring the Doppler profile along the x-axis. The x-axis is parallel to the surface of the target, and we can measure the average kinetic energy of the Ps atom and establish the thermal properties of the target.

The first spectroscopy experiments were done by Joseph Fraunhofer in 1814[8]. Fraunhofer was the first to analyze the continuous spectrum of the sun and studied the many absorption lines observed from the sun. In the mid 1900's the development of the positron pulsed source began with the invention of the laser in the mid 1960's. The invention of the laser enabled the capability of studying various gases, solids, and other material's with a spectral resolution that exceeded the traditional spectrometer. Next we will review the optical experiments done on Ps, which started in 1974 by Varghese.

1.2 Review of Optical Spectroscopy experiments with Positronium

In 1974 Varghese and associates detected, based on Positronium 2γ annihilation, the formation of *n*=2 state Positronium atoms in a gas. The optical excitation was initiated from a broadband incoherent light source with Ps atoms in the ground state[9].

In 1975 Canter et al. observed the Lyman-α radiation from positronium atoms. Excited state Ps atoms were formed when a slow positron beam was incident on a solid target and emitted slow Ps atoms from the surface. The 243nm photons were measured using a 2.0nm wide interference filter at different wavelengths. The detected photons were coincident with measured annihilation of Ps atoms in the ground state. The estimated formation efficiency of excited state Ps atoms was 1 in every 10^4[10].

In 1982 Chu and Mills observed the $1^3S_1 \rightarrow 2^3S_1$ transition using two-photon Doppler-free excitation, essentially having two 486nm pulsed laser beams aligned anticollinear to one another so that only atoms that had a zero component velocity along the axis of the photon's direction were excited. But producing a continuous source of 486nm light requires a build up cavity, and did not require two separate laser beams placed into the target chamber as just described. Transitions were induced by a pulsed dye laser, and detected by photoionization of the 2^3S_1 state using a third 486nm photon. The FWHM of the resonance profile was 1.5 GHz. The frequency that Chu and Mills measured was in close to agreement with theory to within 0.5 GHz. Chu and Mills also observed the amplitude of the signal to behave as the square of the laser's intensity due to a combination of a pulsed dye laser trapped within a build up cavity [11].

Two years later in 1984 Chu, Mills, and Hall measured the 1^3S_1-2^3S_1 interval in Ps with an improved accuracy reaching within the Mhz range, an improvement of an order of magnitude 1000 over the previous measurement. The measured value was 1 233 607 185 ± 15 MHz. This was in close agreement to within 1% of the QED prediction, $\alpha^3 R_\infty$. The measured resonance was established with respect to the Te_2 absorption line and the calibrated Te_2 line relative to the deuterium $2S_{1/2}$-$4P_{3/2}$ Balmer line[12].

In 1990 Ziock et al. were the first to measure high-n Rydberg states of Positronium atoms using a two step, two photon laser excitation process starting from the n=1 →n=2 and n=2 → n Rydberg transitions. Ziock and his team also observed the $1/n^3$ scaling of probability of the transition from n=12 to 19 [13].

Within the same year Ziock, Dermer, Howell, Magnota, and Jones measured another important parameter, the energy needed for saturating the $1S^3 - 2P^3$ transition for Ps[14].

An improvement of the 1^3S_1-2^3S_1 interval occurred in 1993 by Fee et al. Fee switched to a continuous-wave excitation rather than a pulsed laser. This was done to eliminate the problems occurring in the pulsed laser measurements since the excitation was nonlinear. Fee measured the 1^3S_1-2^3S_1interval to be 1 233 607 216.4±3.2 MHz[15].

In 2010 Cassidy et al. measured the kinetic energy of vacuum positronium (Ps) atoms using porous silica film as the target. The energies were measured via the Doppler linewidth of the Ps 1^3S-2^3P transition. A chapter is devoted to the discussion of this measurement in which we found the deeper the positrons were implanted into the

target film, the colder the emitted Ps atoms became. This result was due to the collisions in the pores that were occurring as the Ps atoms diffuse back to the surface of the film. We measured a lower limit energy in the direction of the laser of E_x=42±3meV. This value was found to be dependent on conversion of the confinement energy of Ps in 2.7-nm-diameter pores which is converted into kinetic energy once in vacuum. This was the first exploration of the 1^3S-2^3P transition and demonstration many excited Ps atoms thru optical excitation[16].

In 2011 Cassidy et al. performed the first sets of experiments that explored the Lyman-alpha (1*S*-2*P*) transition for Ps atoms inside and outside of a porous silica target. The linewidth of the Ps atoms inside the porous silica target was 0.066±0.004nm (FWHM), which is approximately half of what we expected for Ps at room temperature in vacuum. This effect is due to Dicke line narrowing within the pores of the target. This result could possibly provide additional cooling of Ps atoms further down to room temperature kT[17].

In 2011 Cassidy and Mills observed that the Zeeman mixing effect of the 2P states of Ps, which resulted in the long lived triplet state atoms converting into shorter lived singlet states, was eliminated for high magnetic fields above 2 Tesla. Previously experiments at low magnetic field we showed a single laser excitation event was measured thru the process of Zeeman mixing, but this would prevent the possibility of laser cooling since the “leakage” would eventually deplete the original population of ground state triplet Ps atoms needed for absorption and spontaneous emission after

multiple laser pulsed events. In this experiment a large splitting is created due to the high magnetic field. The amount of mixing decrease for fields greater than B=0.16T and is essentially eliminated above ~2T. This could possibly enable laser cooling of Ps at higher magnetic fields [18].

In 2012 Cassidy et al. demonstrated producing Rydberg positronium (Ps) atoms in a two-step, two photon process using incoherent laser excitation similar to Ziock in 1990 with the exception that the number of Ps atoms created increased by a factor of 200. The Rydberg states that were explored consisted of the principal quantum numbers n= 10 to n= 25. We find an efficiency of excitation from the $2P^3$ to the Rydberg levels was 90%. This efficiency may have been possible due to intermixing of Stark sublevels upon reaching the Rydberg states which would cause a shift in the induced emission needed to de-excite the Rydberg atom back down to the 2P state. This experiment provided a possibility that one might use Rydberg Ps atoms for performing antigravity measurements on Ps [19].

In 2012 Cassidy et al. measured the first Doppler-free measurements of the Lyman-α transition and observed a Lamb dip at a wavelength of λ_L=243.0218±0.0005nm. A second feature, the crossover resonance, was also measured which represented an increased amount of gamma ray annihilation. The wavelength value for the crossover resonance was λ_C=243.0035±0.0005nm. The physics behind the crossover resonance was due to an excitation from the 1^3S_1 ground state to the Zeeman mixed 2*P* states. The electron in the 2P states are then driven down by stimulated emission to the 1^1S_0

ground state. The interesting feature of this measurement is that the difference between the two resonances λ_L-λ_C was related to the Ps hyperfine interval. This was the first measurement of the ground state Hyperfine interval done thru the optical techniques. The measured hyperfine interval was E_{hfs}=198.4±4.2GHz[20].

Laser spectroscopy of Ps has advanced considerably due to the recent UCR experiments and we are in a position to explore many interesting topics, including ultrahigh precision 1^3S_1-2^3S_1, Rydberg Ps gravity, and Ps emission spectroscopy of the electronic states of metals.

1.3 Why Positronium?

Why do physicists care about Positronium? Positronium is fundamentally the simplest atomic antimatter system. It is made up of an electron and positron and when in close proximity to one another forms a metastable state, or an antimatter atom. The atom itself is not long lived and in its ground state triplet configuration, lives for 142ns. An amazing aspect of the positronium atom is that it fundamentally mirrors the hydrogen atom in the basic properties such as the charge and number of constituents that make up a two atom system. The exception is that the nucleus of the Hydrogen atom is made up of a proton, which can be broken down into three quarks, two down quarks and one up quark. The Ps atom as result, can ignore the hadronic interactions. In comparison to Ps the orbiting positive nucleus is replaced by a more fundamental lepton, the positron. The positron has a positive charge is exactly the same as the

electron with the same mass, magnitude of charge, and magnetic moment as the positron.

Scientist's can treat the positronium atom as a two body problem which has a solved analytical solution since we can use the same solutions of the Schrodinger equation applied for the Hydrogen atom case. Most fundamental measurements done with Hydrogen , 1S-2S measurement are now being done with positronium to higher and higher precisions. The theoretical energy levels now include $\propto^4 ln \propto R_\infty$[21-24].

The positron and electron are both leptonic particles. A lepton has no internal structure, i.e. up or down quarks, and the concept of a radius has no meaning, since it has no measurable dimensions. The lepton cannot be broken down to a more fundamental particle. Leptons interact by electromagnetic interactions and as result the energy levels of Ps can be calculated to a very high accuracy using the methods of QED. For this reason, there is a large interest in measuring the 1S-2S transition. The 1^3S_1-2^3S_1 transition has a 1.3Mhz natural linewidth, and also the QED corrections, of order $\propto^4 R_\infty c = 9.3Mhz$[25], is an ideal test for QED , since the corrections are of large order.

1.4 Broadening Mechanisms of the Lyman Alpha Transition

The natural linewidth is the Fourier Transform of the radiative decay time into frequency space. For the Positronium 1S-2P transition, the decay time of the excited 2p

state, has a mean lifetime of 3.2 ns. The relationship between the natural linewidth and the spontaneous radiative decay time is given as:

$$\delta\nu = \frac{1}{2\pi\tau_i}$$

Assuming the Ps atoms have zero velocity with respect to the lab frame the natural linewidth is 50Mhz. We also assume a single photonic excitation energy of 3nJ, which is the energy needed for saturating the 1S-2P transition, to avoid power broadening.

The atom's emission frequency is Doppler shifted due to the movement of the atoms to 2nd order by

$$\omega_e = \omega_o + \vec{k} \cdot \vec{v}$$

in the lab's reference frame. The 2nd order Doppler broadening effect is given by an additional third term in the same expression:

$$\Delta\omega = \omega_O + \vec{k} \cdot \vec{v} - \omega_O \frac{v_i^2}{2c^2} + \cdots$$

This third order term cannot be removed thru typical Doppler free spectropscopy experiments since the third term has no directional dependence of the photon's k-vectors with respect to the atom's velocity, and is purely a scalar term. In our spectroscopy experiments our measurements were established with the detection of gamma ray photons and not the Alpha Lyman photons through laser excitation, and this process of how and why we detect gamma rays will be discussed in Chapter 4.1. The gamma rays were emitted in a closed High Vacuum chamber since gamma rays can go through everything. In saturated laser spectroscopy experiments a photodiode or

photomultiplier tube is used to directly detect the emission of UV photons. The photon frequency in the lab's rest frame, ω, appears in the frame of the moving atom as

$$\omega' = \omega - \vec{k} \cdot \vec{v}$$

The velocity of the atom is given as, $\vec{v}$. The photon's k vector is $\vec{k}$. The Ps atoms will only absorb the resonance frequency ω_o when $\omega' = \omega_o$. Solving for the laser frequency we get

$$\omega_{absorb} = \omega_o + \vec{k} \cdot \vec{v}$$

The velocity distribution of the atoms is thermal which follows a Maxwell -Boltzmann type distribution. The expression above can be simplified using algebra and redefining the absorption frequency as, $\omega_{absorb} = \omega_o(1 + v_z/c)$. Solving for the z component of the velocity gives us the number of atoms absorbed as[26]

$$n(\omega)d\omega = N_i \frac{c}{\omega_o v_p \sqrt{\pi}} e^{-(\frac{c(\omega-\omega_o)}{\omega_o v_p})^2} d\omega$$

The Doppler width is then given as[26]

$$\delta v_D = 7.16 \times 10^{-7} v_o \sqrt{T/M}$$

Note that in the expression for the Doppler shift, we assume the light is traveling only along the z – axis, then only the atoms with a z - component in there velocity with respect to the photon's k-vector, will observe a shift. Atom's moving perpendicular to the photon will not be absorbed unless the laser's frequency is ω_o.

1.4.1 Power Broadening

The natural linewidth is related the radiative decay rate of the Ps atom during single pulsed photon excitation. The conditions for the rabi oscillations for CW light is given by the expression[27],

$$\Omega_{\mathrm{nd,2p}} = \frac{|\langle 2\mathrm{p}|\mathrm{e} * \mathrm{r}|1\mathrm{s}\rangle|}{\mathrm{h}} \sqrt{\frac{2\mathrm{I}_{\mathrm{laser}}}{\epsilon_{\mathrm{o}}\mathrm{c}}}$$

The rabi oscillations describe the population density of excited state Ps atoms over time. To illustrate the idea of Rabi oscillations we use the experiments done by Citron[28]. Citron was able to isolate the two hyperfine components in sodium's D_2 line that was isolated from the hyperfine's various sublevels and zeeman splittings. This made the atom a simple two level system and using frequency stabilized CW dye lasers he demonstrated the power broadening effect [28] by increasing the energy of the probing laser. Power broadening is well described by the following expression:

$$\gamma_{Power} = \gamma_{natural}\sqrt{1+S}$$

S is defined as $S = {M_{ab}}^2 E^2/(\hbar\gamma)^2 = (R/\gamma)^2$where M is the dipole matrix element and the E is the electric field strength associated with the laser light. The Rabi frequency, $=$ $M_{ab}E_o/\hbar$, is a parameter that determines the rate at which the electron will make the transition from the ground state to the excited state. In Fig. 1.1 is an example of how the electron population density behaves over time.

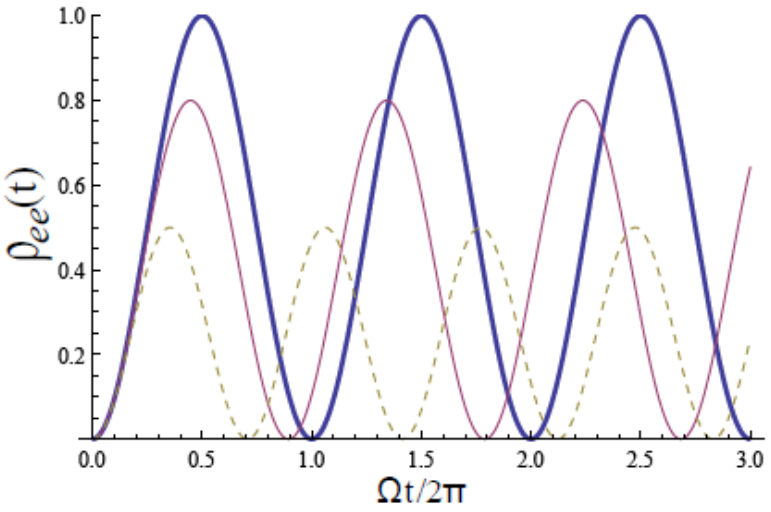

Fig. 1.1 Adapted from [29]. Rabi Oscillations for$\rho_{ee}(t)$ for a fixed Rabi Frequency, Ω, with different detuning values of $\delta = \omega_{laser} - \omega_o$. The thickest line represents $\delta = 0$.

There are two parameters involved in looking at the probability of excitation in the excited state over time: 1) The amplitude of the transition probability, which is dependent on the frequency of the laser that is used to excite the atom. If the laser is detuned slightly off resonance the probability of the electron being in the excited state decreases. 2) The rate at which the rabi oscillations occur is dependent on the energy of the probing laser. For a laser tuned to the exact resonance or $\delta = 0$, we have a higher probability that most of the electrons will be within the excited state of the atom. As we detune the laser away from resonance, ω_o, we have a lower probability of excitation to the excited state but the rate at which electron exists in the 1s state and 2p state, for example, increases.

Next we can go back to the scenario of tuning the laser to be on resonance, $\delta = 0$, and increase the Rabi frequency by increasing the electric field which means

increasing the energy of the laser. This results in the power broadening effect in that the rate of electron transition dictates the linewidth that is measured when we scan across a perfect two level system. When the natural Rabi oscillations exceed the natural linewidth, the natural radiative decay rate no longer determines the linewidth and power broadening results, as shown in Fig. 1.2 for two specific cases.

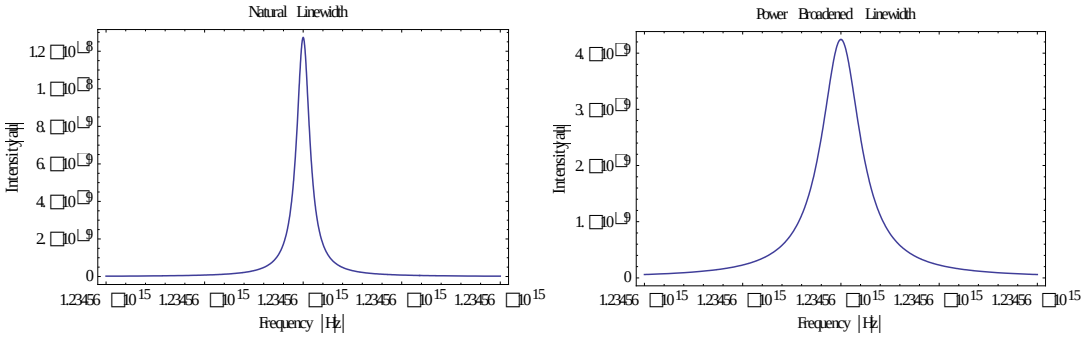

Fig. 1.2 Plot of the natural linewidth of 50Mhz for the 1S-2P transition. Plot on the right shows what happens when energy of the pulse is increased by factor of ten.

Power broadening, in context to using two laser pulses, is also is dependent on the time overlap of the two photon pulses with the Ps cloud emitted from the target. If the experiment requires a single excitation beam and a photo ionization source, the power broadening effect would most likely be pronounced if the excitation beam and photoionization beam are simultaneously arriving into the Ps target chamber, or else no broadening effect will be observed if a time delayed is introduced [30]. Another type of broadening that occurs is collisional broadening if the Ps atom approaches another atom or molecule in vacuum. At the target region, the pressures are10^{-9} torr or UHV. The mean free path at UHV conditions means that the Ps atom will travel 31 miles

before hitting another possible atom within the vacuum. Once born into vacuum the Ps atom's have no other residual gas left in the UHV chamber to collide with, hence the pressure broadening term possibly has a zero contribution, with the exception of another Ps atom.

Transit Time Broadening

Another form of line broadening occurs with the interaction time between the laser pulse and the positron source emission. The transit time broadening depends on the geometrical spatial overlap of the light and Ps cloud as shown in Fig. 1.3 below.

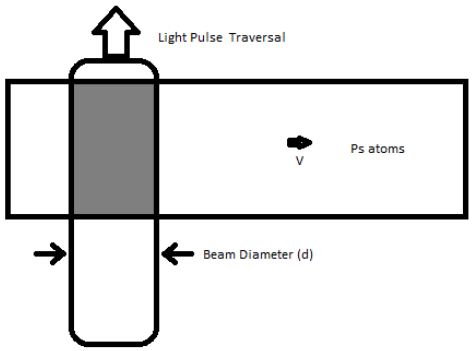

Fig. 1.3 The diagram shows the spatial overlap of the laser beam diameter with the Ps atom's emitted from the target, roughly speaking.

The interaction time is limited by the time the atoms spend in the light pulse. Assuming the energies used are below saturation and the Rabi frequency is adjusted to 50Mhz, by using approximately 10uJ, we will find that the linewidth is limited by not the spontaneous radiative lifetime, but the interaction time. We use the following expression to find the frequency component's of the amplitude of the light[26]:

$$A(\omega) = \frac{1}{\sqrt{2\pi}} \int_0^T x_o \cos(\omega_o t) e^{-i\omega t} dt$$

The field for TEM 00 is given as[26]:

$$E = E_o e^{-r^2/w^2} cos\omega t$$

The intensity is given as $I(\omega) = A^* A$, and we assume a amplitude of $x = \alpha E$ we get the flowing Gaussian line profile expression:

$$I(\omega) = I_O e^{(-(\omega-\omega_o)^2 \frac{\omega^2}{2v^2}}$$

The transit-time limited halfwidth is (FWHM) then given as[26]

$$\delta w = 2(\frac{v}{w})\sqrt{2(ln2)} \approx \frac{2.4v}{w} \rightarrow \delta v \approx 0.4v/w$$

It is known in the Boltzmann Distribution of Rydberg Ps atoms that the typical speed of the atoms emitted from the Cu 100 or Silicon sample is 230km/s. The beam diameter is 2mm so the corresponding transit time is 8ns. This leads to a line broadening of roughly $\delta v \approx 0.4 \left(\frac{230000}{0.002}\right) = 50Mhz$, which is an order of magnitude larger than the natural linewidth. As result the broadening effect is not important since the dye laser bandwidth is two orders of magnitude larger, but this additional line broadening effect is important in the 1^3S_1-2^3S_1Doppler free measurement. If one were to perform Doppler free laser spectroscopy of the 1^3S_1-2^3S_1transition one can enlarge the laser beam diameter, from 2mm to 10mm, then the transit broadening would be $\delta v \approx 0.4 \left(\frac{230000}{0.010}\right) = 9.2Mhz$, which is still larger than the natural linewidth of the 1^3S_1-2^3S_1transition.

In addition to the transit time broadening there is the radius of curvature of the laser pulse itself. The radius is typically determined by the divergence of the beam, which is 0.5-1mrad for our experiment. Since $s = r\theta$, the distance is 3m to the target chamber and the SHG beam diameter is typically 2mm at the target chamber. Using the Pythagorean Theorem we find R=$\sqrt{2mm^2 + 3m^2}$ = 300cm. Using the expression for beam curvature transit time broadening[26] we get

$$\delta w = \delta w_{tt}\left[1 + \left(\frac{\pi w^2}{R\lambda}\right)^2\right] = 50Mhz\left(1 + \left(\frac{\pi(1mm)^2}{3m * 243nm}\right)^2\right) \sim 0.75Ghz$$

As a result we find the line broadening effects are not important, but adds to the measurement of width of the Doppler profile if the laser linewidth approaches 1 Ghz.

Dicke Line Narrowing effect

The line narrowing effect was first observed by Dicke[31]. In context to Positronium this effect occurs when the atom has collisions that occur when diffusing thru the interconnected pores of the target. The porous target is talked about in Chapter 4.1 , the physics behind this result is as the Ps diffuses from pore to pore it produces a collision within the walls which slows the Ps atom down. Depending on the depth of the material and density of the target the number of collisions can vary with different implantation energies. A larger number of collisions occur within the surface of the porous film compared to no collisions outside the surface of the target, we observed two different linewidths using the 1S-2P transition of Ps. We see an effect as after entering the target, we observe a much narrower Doppler broadened linewidth[17].

Due to the lower number of Ps atoms being produced in vacuum there is no collisional partner in a 10^{-9}torr UHV system , and we assume that this form of Pressure broadening is not an effect that was measured in the lab.

Conclusion

Other forms of line broadening effects also exist including the ones mentioned in this chapter. The bandwidth of the probe laser must also have a linewidth equivalent to the natural linewidth of the Ps atom. A large bandwidth laser would show a measured spectral profile that is similar to the laser's bandwidth. Also the level's that are excited, due to the selection rules, are not constrained to only two single level's, the ground state level and the excited state level. Selection rules can be applied to the Ps's 2P excited state, which has 6 sublevels with no external field perturbations. The total width of the 2P state is approximately 25 Ghz wide. In addition for Ps it's well known how the level's shift when immersed in a static magnetic and electric field which produces a Stark, Motional Stark, and Zeeman shifts to each of the levels [32,33]. A careful budget of the line broadening effects would need to be accumulated with the help of the selection rules, which will be discussed in the next chapter, to explain the width associated with the Doppler profile.

1.5 Selection Rules

If the Ps atom was prepared in an excited state such as 3p($n = 3, l = 1$), what is the transition probability for the following two paths, $3p \rightarrow 2s or\ 3p \rightarrow 1s$? Does the $3p \rightarrow 1s$ transition produce a stronger radiative fluorescence than the $3p \rightarrow 2s$? The probability of each Ps atom's excitation or radiative decay can be determined by the following integral

$$M = \int \psi_f^* r \psi_i d\tau$$

ψ_i is the initial state and ψ_f is the final state. The probability of a particular transition can be used to explain the strength of a transition by measuring the intensity of the light from spontaneous fluorescence or absorption, for example, the experimental and theoretical values shows a fairly good agreement for detecting a lower expected number of produced Rydberg Ps atoms thru two step optical transitions[13,19,27] in between n=14 to n=25, including the bandwidth effects of the laser and stark shifting and broadening. The dipole matrix element from the integral above is

$$\langle \psi_f | r | \psi_i \rangle$$

The matrix element can be specified further using n as the quantum number, l as the angular momentum, and m_l as the z-component of the angular momentum, with all values quantized accordingly.

$$\langle n'l'm' | r | nlm \rangle$$

Applying the momentum commutation relations to the dipole matrix element leads to the following selection rules[34],

$$\Delta m = \pm 1 \; or \; 0 \quad \& \Delta l = \pm 1$$

The integral M is only non-zero when we use the selection rules. The expression$\Delta l = \pm 1$ represents a change of angular momentum of the atom after an absorption of a photon, by one unit. The conservation of momentum must occur since the photon carries a spin of S=1 where $m_s = \pm 1$ represents the photon as being circularly polarized.

Since the electron and positron also carry spin, selection rules for the total angular momentum can then be defined by both L and S components. Another selection rule is added by law of conservation of spin which is

$$\Delta S = 0$$

Since spin and the z-component of the spin is conserved the total angular momentum is defined by

$$J = L + S$$

Then it can be implied that the selection rules for J and the z-component of J are:

$$\Delta J = 0, \pm 1$$

For the $1^3S_1 \rightarrow 2^3S_1$ transition the spin is conserved and since the process is a single step two photon excitation the Ps atoms only absorb for frequencies exactly equal to the $1^3S_1 \rightarrow 2^3S_1$ transition, 1 233 607 216.4±3.2 MHz. This occurs only for atoms that are stationary along the photon's k-vector direction. Since each photon carries a spin value of $m_s = \pm 1$ in counter propagating directions the atom's angular momentum is

still conserved with the two photo absorption event since this corresponds to the same angular momentum state in the initial and final states, $l = 0, or\ S$- state.

References

[1]J.R. Oppenheimer, Phys. Rev. 35,562(1930)

[2]P.A.M. Dirac, Proc. R. Soc. Lond.A 133,60 (1931)

[3] C.Y. Chao, Proc. Nat. Acad. Am. 16, 431(1930); Phys. Rev. 36., 1519(1930)

[4]C.D. Anderson, Phys. Rev. 43, 491(1933)

[5] M. Deutsch, Physical Review. 82, 455 (1951)

[6]P.J. Schultz, K.G. Lynn. Reviews of Modern Physics, Vol. 60, No.3 July (1988)

[7]Mohr, Peter J.; Taylor, Barry N.; Newell, David B. (2012). "CODATA recommended values of the fundamental physical constants: 2010". *Reviews of Modern Physics***84** (4): 1527

[8] Joseph Fraunhofer "Determination of the refractive and color-dispersing power of different types of glass, in relation to the improvement of achromatic telescopes",Memoirs of the Royal Academy of Sciences in Munich, 5: 193-226

[9]S.L. Varghese, E.S. Ensberg, V.W. Hughes, I. Lindgren,Phys Lett A 49, 415 (1974)

[10]K.F. Canter, A. P. Mills, Jr., S. Berko, Phys. Rev. Lett. 34, 177(1975)

[11] S. Chu, A. P. Mills, Jr., Phys. Rev. Lett 48, 1333(1982)

[12] S. Chu, A. P. Mills, Jr., J.L. Hall, Phys. Rev. Lett. 52,1689(1984)

[13]K.P. Ziock, R.H. Howell, F. Magnotta, R.A. Failor, K.M. Jones, Phys. Rev. Lett 64,2366(1990)

[14] K. P. Ziock, C. D. Dermer, R. H. Howell, F. Magnota, and K. M. Jones, J. Phys. B 23, 329 (1990)

[15]M.S. Fee,A. P. Mills, Jr., S. Chu, E.D. Shaw, K. Danzmann, R.J. Chichester, D.M. Zuckerman, Phys. Rev. Lett. 70, 1397(1993)

[16] D.B. Cassidy, P. Crivelli, T.H. Hisakado, L. Liszkay V.E. Meligne, P. Perez, H.W.K. Tom, A.P.Mills Jr., Phys. Rev. A 81 012715 (Jan 2010)

[17] D.B. Cassidy, M.W.J. Bromley, L.C. Cota, T.H. Hisakado, H.W.K. Tom, A.P. Mills, Jr. , Phys. Rev. Lett. 106, 023401 (Jan 2011)

[18] D.B. Cassidy, T.H. Hisakado, H.W.K. Tom, A.P. Mills, Jr. Phys. Rev. Lett. 106, 173401 (April 2011)

[19] D.B. Cassidy, T.H. Hisakado, H.W.K. Tom, A.P. Mills, Jr. Phys. Rev. Lett. 108, 043401 (Jan 2012)

[20] D.B. Cassidy, T.H. Hisakado, H.W.K. Tom, A.P. Mills, Jr., Phys. Rev. Lett. 109 073401 (August 2012)

[21]R.A. Ferrell, Phys. Rev. 84, 858 (1951).

[22]T. Fulton, Phys Rev. A 26, 1794(1982).

[23]S.N. Gupta, W.W. Repko, and C.J. Suchyta III, Phys Rev. D 40, 4100 (1989).

[24]R.N. Fell, Phys Rev. Lett. 68,25(1992).

[25] I.B. Khriplovich, A.I.Milstein, and A.S. Yelkhovsky, Phys Lett. B 282, 237 (1992)

[26]W. Demtroder, Laser Spectroscopy (Springer-Verlag, Berlin 1996)

[27]S.D. Hogan Phys. Rev. A, 87, 063423(2013)

[28]M.L. Citron, H.R. Gray, C.W. Gabel, and C.R. Stroud, Jr. Phys. Rev. A, Vol 16, No 4. Oct. (1977) Pages. 1507-1512

[29] D. T. Stack, Ph.D Dissertation Optical Forces from Periodic Adiabatic Rapid Passage Sequences on Metastable Helium, Stony Brook University August 2012.

[30]N.V. Vitanov, B.W. Shore, L. Yatsenko, K. Bohmer, T. Halfmann, T. Rickes, K. Bergmann, Optics Communications 199 (Nov 2001) Pgs. 117-126

[31]R.H. Dicke, " The effect of collisions upon the Doppler width of spectral lines" Phys. Rev. 89, 472(1953)

[32] " Combined Zeeman and Motional Stark Effects in First Excited State of Positronium " S.M. Curry, Physical Review A. Vol 7, No 2 Feb. 1973, Pgs 447-450.

[33] " Perturbative Analysis of Simultaneous Stark and Zeeman effects on n=1->n=2 radiative transitions in Positronium" C.D. Dermer, J.C. Weisheit Physical Review A, Vol 40, No 10 Nov 15,1989 p5526-5532

[34]D. J. Griffiths, Introduction to Quantum Mechanics, 2nd Ed. Prentice Hall, 2005.

Chapter 2
Positronium Production

2.1 Source

Our positron source in the lab is a radioactive isotope, Na-22, purchased from a Facility in South Africa[35], which are placed in sealed capsules. The decay process is $^{22}Na \rightarrow {}^{22}Ne + \beta^{+} + \upsilon_e + \gamma$, which has a 90.4 percent conversion efficiency, or branching ratio into positron decay,β^{+}. The two most commonly used positron sources are the radioactive isotopes Na-22 and Co-58 [36] due to their long half life's for beta decay. Na-22 has the longest half life of 2.6 years and decays by β+ decay into extremely fast Positrons with a broad energy spectrum centered around 0.5MeV.

Isotope	Half-Life	End Point Energy/Intensity(Mev/%)	γ ray Energy
^{11}C	20.3 min	0.9608/99	-
^{13}N	9.97min	1.190/100	-
^{22}Na	2.605 years	0.545/90	1.2745/99.9
^{58}Co	70.88 Day	0.474/15	0.810755/99
^{64}Cu	12.0701 hours	0.573/19	-

Table 2.1 Most Commonly used Positron Isotopes/Sources [36].

Most of the positrons emitted from the Na-22 come out very fast, and in a working lab it's not possible to perform an experiment with fast positrons[37]. The first positron sources were slow continuous beams that had an emission rate of only a few positrons/sec[38,39,40]. One of the key discoveries came in 1974, when Canter discovered that incident slow positrons implanted on baked surfaces produces a

significant amount of Ps atoms with high efficiency[41]. In 1985-1986 it was discovered that the using a solid neon gas that is adsorbed onto a metal at temperatures less than 10 degree's Kelvin provided a way of capturing 100 eV Positrons, emitted from Na-22, and producing a slow positron emission of 0.5eV. This process is called " moderation" of fast positrons and the measured efficiencies of 0.7%, is still the highest today[42]. The Neon moderator efficiencies were advanced by the improvement of a two stage low cost, closed cycle refrigerator, which enabled the moderator to reach 6.5K routinely [43]. In the lab we have a 20mCi Na-22 source and the direction of the flow of the Research Grade neon gas, as the boiling temperature of Neon is 10 kelvin, is aimed directly onto the copper parabolic cup, during the growth phase. The neon gas is research grade at 99.9995% and is released under a pressure of 1×10^{-4} torr for 7 minutes. The base pressure is held at 10^{-10} torr. At a typical efficiency of 0.7%-1.5% the yield is approximately[44]

$$20mCurie \times 3.7 \times 10^{10} \times 0.9(BranchRatio) \times 0.7\% = 5 \times 10^{6}/sec$$

The Neon moderator is not continuously emitting slow positrons at the given rate in the expression above, and this is due to the exposure of the buffer gas coming from the adjacent differential pumping stage of the trap. The positron emission rate decreases at 5% per day. In the Fig. 1.4 is the schematic of the source assembly by Greaves and Surko.

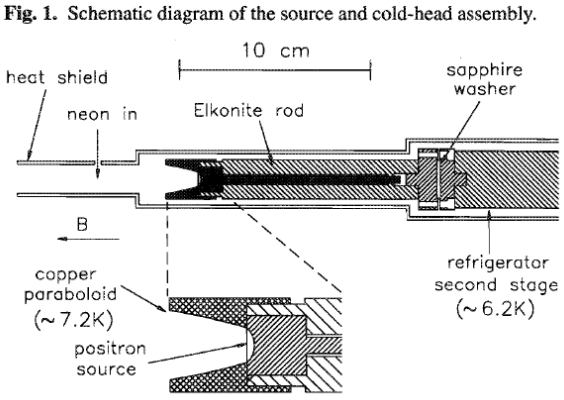

Fig. 2.1 Adapted from [43]. Diagram of the Solid Neon Moderator and cold head assembly.

The figure above shows a cross section of the experimental positron source, though not exactly the same configuration but the copper material, geometry, and temperature are the same. The installation procedure requires alignment of the copper cone to the axial magnetic field from the transfer coil that is connected between the source and the trap. The loading and unloading that occurs when obtaining access to the copper cold head is done vertically as oppose to horizontally as shown in Fig. 43. The positrons are then transferred from the moderator to the trap using a positively biased voltage applied onto the moderator. The remaining high energy unmoderated positrons that are transmitted are then filtered using a magnetic deflector which prevents them from entering the trap.

2.2 Trap

The trap we use for our High density Ps pulser system uses a nitrogen buffer gas, a three stage differential pressure, and a three stage potential well developed by Surko and Murphy [45,46] which is a modification of the Malmberg Penning trap. The

Malmberg Penning trap consists of a vacuum chamber with a negative and positive potential applied at the ends of the chamber with an axial magnetic field applied as shown in Fig. 2.2. Specifically speaking of the modification, the Malmberg Penning design is used with the addition of a three stage electrode placed within the trap and an applied differential pumping at three different sections along the z-axis of the trap[45]. A differential pressure system can be integrated by using three different diameters within the vacuum chamber at three different regions along the z-axis. The trap chamber operates at a base pressure of 1×10^{-10} torr with the Nitrogen gas[45] released at a pressure of 5×10^{-6} torr at stage I in the trap. In stage I the diameter of the cross section is 2.54cm. Within the entire trap an axial magnetic field of 500 Gauss is used with copper wire, 38 gauge, with a particular thickness of wire insulation with 30 volts applied, 30amp constant current encompassed by house chilled water, which is maintained at a temperature of 50 deg F directly from the source. The transfer of the house chilled water is optimized using thermal pipe insulation and daily replacement of the water filter. This magnetic field is not strong enough to cool trapped positrons thru cyclotron radiation so an external means is needed with the introduction of the buffer gas, Nitrogen. The magnetic field constrains the trajectory of the positron's and prevents them from hitting the walls of the chamber, or else direct annihilation will

occur, and decrease transfer efficiencies.

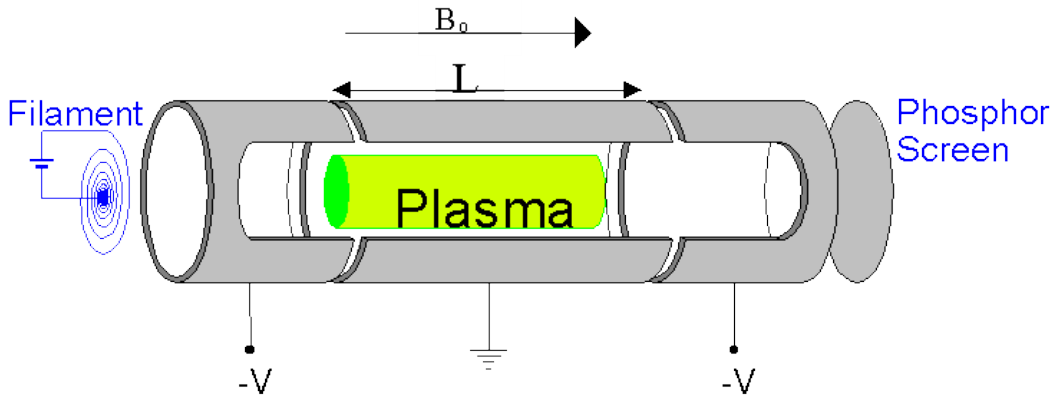

Fig. 2.2 Figure adapted from [47]. Penning Malmberg Trap.

As the positrons are transferred across the ends of the trap they encounter a three stage potential drop across the trap system in combination with previously mentioned pressure differential. In Fig. 2.3 the plot shows the three electrode configuration and the pressures applied during these three stages. Each electrode, spaced by a high vacuum electrical insulator placed on rails, is a metal cylinder with UHV electrical feedthrough connectors, with an electrical potential applied at different position's along the entire trap. Each stage uses Nitrogen gas at three different pressures 10^{-3},10^{-4}, and 10^{-6} torr. Nitrogen is well known to be the best buffer gas in capturing efficiently positrons due to its large collisional cross section for trapping positrons and also having a small cross section for Ps formation[48]. The buffer gas within stage 1 of the electrodes, ensures that a positron-molecule collision occurs with one pass through the trap [49]. In addition the electrode within the trap are tuned to maximize the chance of an electron excitation at ~8.8eV for nitrogen [49].

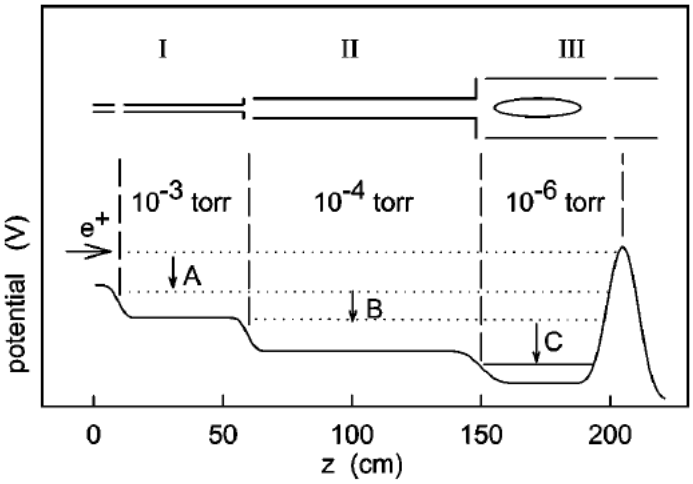

Fig. 2.3 Figure adapted from [49]. Schematic of electrode configuration used in the trap. Notice the outline drawn refers to the electrode shape, in addition the different applied pressures along the z-axis.

After capturing the positrons using the Nitrogen gas a constant buildup of a large positron plasma density accumulates at the right end of the trap or accumulator. As a result the positron plasma expands, so the positrons must then compressed radially using a "rotating wall" by applying a quadrupole electric field effect using an eight-segmented electrode at a frequency of 4 – 5Mhz. The field is generated by eight sine waves with amplitude A, and frequency f, with relative phases shifted by 90 deg for each two set's of the four segmented electrodes[50]. The inner diameter of the electrodes is 2.54cm. The spatial compression of the plasma extends the lifetime of the captured positron's by roughly 2 seconds and aids in the transfers efficiencies using a transfer coil as the positron's are shifted to the accumulator from the trap. In the compression

process the positron's exhibit heating and a neutral buffer gas is used to counteract the heating due to the rotating electric field. Transport from the trap to the accumulator occurs when the gate voltage, positioned at the end of the trap, is turned off to move the Positron pulse over to the accumulator from the trap, and the repetition rate occurs at a frequency of 4Hz. By having a pulsed system or triggered event allows us to know when the positron event starts for our Rydberg Spectroscopy experiments. In addition the Rydberg Spectroscopy experiments involved the use of only the moderator and trap, with no accumulator. We will next discuss the accumulator.

2.3 Accumulator

The accumulator is introduced to provide a better vacuum environment and is very similar to the trap system, i.e. same dimensions of the vacuum chamber, and axial 500 Gauss magnetic field, with a primary difference of operating at a lower base pressure of 3×10^{-11} Torr. The large difference between the two base pressures was developed so that a lower vacuum pressure would extend the lifetime of the positrons and produce a longer storage lifetime[49]. The accumulator electrode structure used in lab is shown in Fig. 2.4.

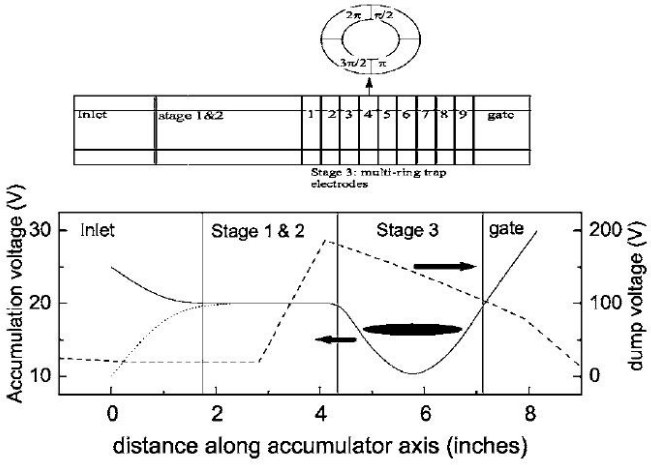

Fig. 2.4 Adapted from [49]. Schematic of the electrode's and multi-ring trap.

The first electrode starts the transmission of the positron pulse from the trap by temporarily lowering the voltage for 100ns by applying a gate pulse to the inlet. In stages 1 &2 the positron encounters the SF6 gas which is another type of gas that cools the positrons further but does not shorten the storage lifetime, considerably. In stage 3 a multi ring electrode system is used to produce a harmonic potential well and an additional rotating electric field is integrated into the 4^{th} ring of the 9 rings that make up the electrode potential well. The positrons are then confined within stages 1-3 and become trapped in the harmonic potential well within 100ms. At the transfer rate of 4hz the lower density positron pulse's are stacked and stored within the potential well of the accumulator electrodes when the inlet potential is opened for ~100ns. After the maximum number of positrons are stored within the accumulator's potential, which is limited by the space charge potential, the gate electrode is then lowered. The high density positron pulse is released with a typical pulse width of 20ns. A photo of the

entire high density Ps pulser apparatus is shown in Fig. 2.5. The distortion in the photo is caused by the “Fisheye” lense used to take a photo of the entire apparatus.

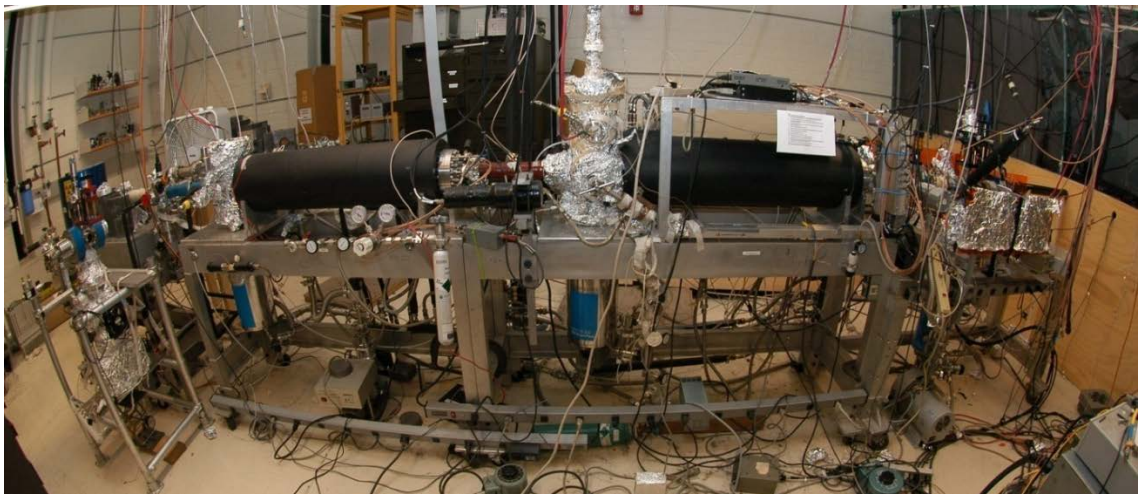

Fig. 2.5 Photo of High Density Pulser Apparatus. The source, trap, accumulator, and target chamber are shown from left to right. The PMT with scintillator is mounted in close approximation to the target.

2.4 Buncher and Target Chamber

The remaining details of the buncher and target chamber are well described in following references[44,49]. The buncher compresses the time width of the Ps pulse from a typical width of 20ns to less than one ns. The positron plasma is transferred from the buncher to the accelerator rings. The accelerator rings are connected to each other with 1MegaOhm KDI Pyrofilm vacuum compatible resistors. The left ring is placed at ground and the positron pulse is accelerated from 150eV to 10keV. The high voltage that is applied is left on for only a few ms.

The discussion of the gamma ray detection scheme will be discussed in Chapter 5. A photo of the target chamber with PMT & Scintillator, CCD camera mounted along the e^+’s beam axis, and viewport is shown in Fig. 2.6.

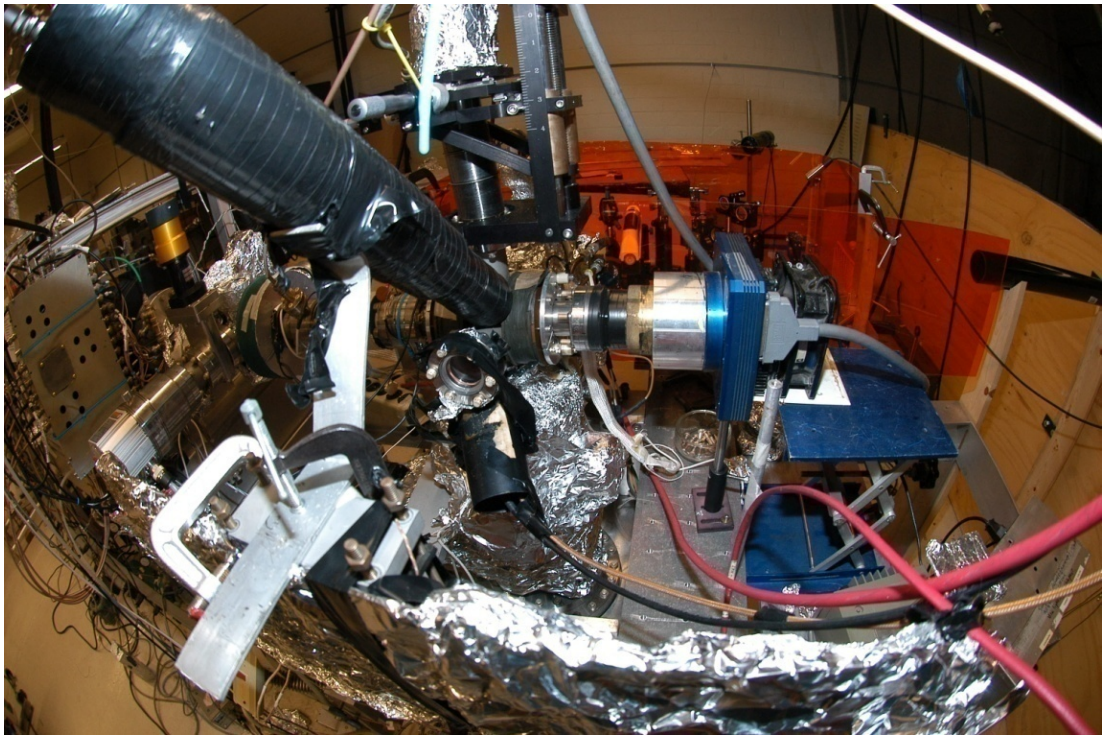

Fig. 2.6 Target Chamber with xyz translation stage for the target. The Ps apparatus includes the source, trap, accumulator, buncher, and accelerator. The PMT & Scintillator are wrapped in black tape is mounted in close distance to the target(~3.0 “). The Two Magnetic Coils on either side of the Viewport reduce the spot size of the Ps pulse to less than 0.25mm. CCD camera (Apogee. Inc) for aligning the high density positron pulse with the UV laser with a Phosphor screen. Please note the Phosphor screen does get damaged using a pulsed UV laser. Optical Setup is on the opposite side of the Viewport.

2.5 Detector: PMT &Multichannel Plate

In our Rydberg spectroscopy experiments[19] we have used the scintillator and a photomultiplier tube(PMT). The scintillator absorbs a gamma ray and fluoresces a photon in the wavelength range that is detectable in the PMT. For the experiments that required the use of the accumulator, which produced ~ 2×10^7 positrons, we used a lead tungstate (PWO) for the scintillator. There are many possible materials that can be used for the scintillator[51]. PWO is selected due to its low attenuation for 511keV

gamma rays of 0.96cm, a relative fast decay time of 5-15ns, and a light yield of 250 photons/MeV [52].

At sometime later within 2013-2014 we switched to operating with the source and the trap. This lowered the number of detected Ps atoms emitted from the target but increased the data rate by a factor of 15. The Ps atoms were converted to Rydberg Ps atoms by two photon, two step excitation using two dye laser's. The UV dye laser was tuned to the 1S-2P transition. The 2^{nd} dye laser was operating at the NIR light wavelengths, to reach then= 10 to n= 25 quantum levels.

Upon reaching the Rydberg state the binding energy is low and as result can be field ionized at the target region, due to the motional electric field resulting from the 70 Gauss magnetic field needed to transfer the positrons from the trap to the target. Rydberg atom's then traveled thru an added extension of the target chamber that reached 1.7m, diagonally away from the trap's axis. The diameter of the extension was 1.3".

The detection of the Rydberg atoms was done with a microchannel plate. A microchannel plate is a 2 dimensional sensor that detects electrons or positrons , x-rays, and amplifies the signal in a similar fashion as the PMT. The channel is made up of a thin glass disc with a large work function. A two channel MCP is made up of two glass discs with 12um diameters holes arranged in a honeycomb like structure. Each face or side of the glass plate has a large potential applied on the front and back face of glass disc. The electron or positron or ion will be drawn into the channel walls and enter into the 12um

hole and emit an electron, which is accelerated by the potential gradient. The primary electron will be drawn further down the channel to produce a secondary set of electrons after hitting the channel walls a second time. This event will repeat itself and a shower of electrons will reach the 2nd glass disc, whose channels are diverted at an angle 15 deg away from the first disc's channels to prevent space charge saturation of the electron pulse upon reaching the end of the channel. The electron pulse is then detected thru the digital oscilloscope at 20Gs/s. The threshold of detection was set at 3mV to avoid double counting events.

The micro channel plate used for detection was a F1217-21S from Hamamatsu Corporation. This model has a 48mm diameter, with 12um diameter channels. There are total of two stages with a single anode readout for the detection of single Rydberg atom events.

A diagram of the detection system is shown below. There are two fine grid wires sheets with 90% transmission. The grid sheet closest to the target is at ground. The next grid sheet has potential of -500V. The two grids allow for field ionization of the Rydberg atoms. Using a Monte Carlo Simulation provided by Dr. A.C.L. Jones, we can see what particular potential is need to provide a large signal to noise ratio for detection of Rydberg atoms. The positrons will be electrostatically focused into the channel plate with a voltage of -2.0 kV. A portion of the MCP holder & ionization grid is shown in the Fig. 2.8.The mechanical diagram is also provided by Dr. A.C.L. Jones, is shown in Fig. 2.7 generated in a CAD program.

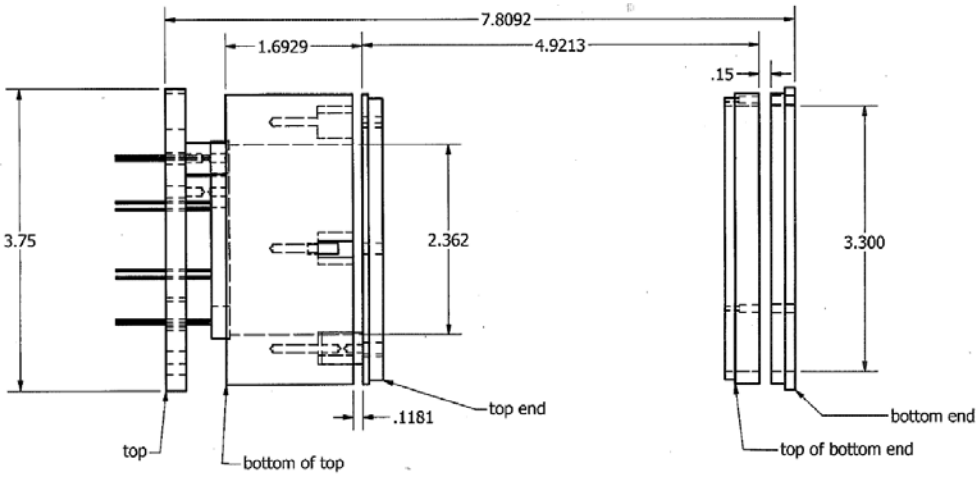

Fig. 2.7 Mechanical Dimensions for MCP holder + Ionization Section.
The right hand side incases two fine wire grid sheets with a 90% transmission.
The two grids are used to field ionize Rydberg atoms. The MCP is mounted on the left hand side of the mechanical layout.

A photo of the partially assembled MCP holder without the MCP is shown in Fig. 2.8.

A Monte Carlo simulation is provided by Dr. A.C.L. Jones which shows the values needed for the electric potential applied to focus the most positrons onto the MCP plate, this is shown in Fig. 2.9.

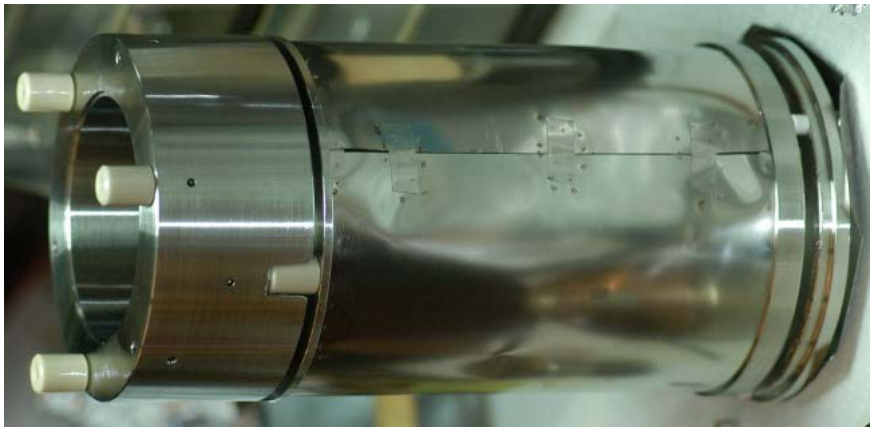

Fig. 2.8 MCP holder (without the MCP) and ionization section used in Rydberg Spectroscopy.

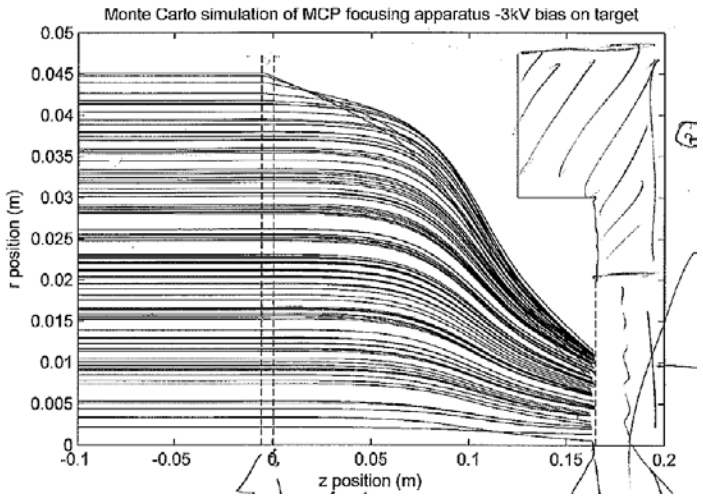

Fig. 2.9 Monte Carlo simulation of ionized positron particle trajectories using a -3.0kV potential applied at z=0.15m.

References

[35] http://www.tlabs.ac.za/public/Radioisotopes.htm

[36] Handbook of Chemistry and Physics edited by D.R. Lide et al.(CRC,2001)

[37] A.P. Mills, Jr," Frontiers in Laser Cooling, Single-Molecule Biophysics and Energy Science", Lawrence Berkeley National Laboratory, August 30, 2008 Berkeley, Ca

[38] W.H. Cherry, Ph.D. Dissertation, Princeton University, Princeton, NJ, 1958.

[39] D.E. Groce, D.G. Costello, J.W. McGowan, D.F. Herring, Bull. Am. Phys. Soc. 13, 1397(1972).

[40] K.F. Canter, P.G. Coleman, T.C. Griffith, G.R. Heyland, J. Phys. B, 5 L167 (1972)

[41]K.F. Canter, A. P. Mills, Jr. , S. Berko, " Positronium Formation by Slow Positrons Incident on Solid Targets", Phys. Rev. Lett. Vol. 33, No. 1, July 1974.

[42] A.P. Mills, Jr. and E.M. Gullikson. Appl. Phys. Lett. 49, 1121 (1986)

[43] R.G. Greaves, C.M. Surko, " Solid neon moderator for positron-trapping experiments", Can. J. Phys. 74, 445-448(1996).

[44] S.H.M. Deng, Ph.D. Dissertation, University of California, Riverside, Riverside, Ca, 2006.

[45]C.M. Surko, M. Leventhal, A. Passner, " Positron Plasma in the Laboratory". Phys. Rev. Lett. 62. No. 8, Feb 20, 1989

[46] T. Murphy , C.M. Surko. " Positron trapping in an electrostatic well by inelastic collisions with nitrogen molecules", Phys. Rev. A 46, 5696(1992)

[47]http://socrates.berkeley.edu/~fajans/Quadrupole/body.html

[48] J.P. Sullivan, J.P. Marler, S.J. Gilbert, S.J. Buckman, C.M. Surko, Phys. Rev Lett. 87, 073201 (2001)

[49] D.B. Cassidy, S.H.M. Deng, R.G. Greaves, and A.P. Mills Jr, Rev of Sci. Instr. 77, 073106 (2006)

[50] R.G. Greaves, C.M. Surko ," Inward Transport and Compression of a Positron Plasma by a Rotating Electric Field" Phys. Rev. Lett. 85. No.9, August, 2000

[51]S.E. Derenzo, W.W. Moses, Lawrence Berkeley Laboratory Report No LBL-33295, 1992.

[52]W.W. Moses, Nucl. Instr. and Meth. In Phys. Res. A 487, 123 (2002)

Chapter 3
Optical Setup

3.1 Dye Laser

The dye laser was first invented independently by P. Sorokin and F.P. Schafer in 1966[53,54]. Then the idea of using a grating as a tunable reflector was demonstrated by Soffer and McFarland in 1967 [55]. Myers[56] and Hansch[57] then incorporated beam expanders to narrow the linewidth emitted using a grating and illuminating a larger section of the grating mirror. In addition this design allowed for ease in tuning the dye laser for a large tuning range and performing high resolution spectroscopy. Dye lasers are the most widely used types of tunable lasers as all continuous wavelengths are possible between 300nm-1100nm. The pulsed dye laser in conjunction with a pulsed YAG laser work very well in the current laser experiments with Positronium atoms. For our experiment we used a single grating pulsed dye laser, PDL-1 or PDL-3 Quanta Ray laser(refurbished). The different models correspond to an internal time delay for the preamp and final amplifier stages. Both versions of the dye laser have three dye cells within the internal section of the laser.

Since the radiative decay is the primary mechanism that dexcites the Ps atom from the 2P state back to the 1S state, a 2^{nd} laser pulse, with a wavelength of 729nm-1064nm, can photoionize and detect the fast annihilation of the ionized positron upon returning to the target or annihilating against the vacuum chamber walls. The rate of

return to the 1S state is $R_k = A_k = {}_{1/\tau_k} = 1/3.2ns$=$3.1 \times 10^8/s$. The cross section for photoionization is ~$1 \times 10^{-17} cm^2$, where as for the 1S-2P transition it is $3 \times 10^{-10} cm^2$. The number of 532 photons should be roughlyn_{L2}>$10^{25}/cm^2 \cdot s$. A pulsed tunable laser source is needed as it satisfies the criterion for detection of laser excited Ps atoms, as using a CW 532 laser would not satisfy this criterion. For example a 8W 532nm laser focused to 2mm in diameter would be short of photon density by a order of magnitude of 10^5 in photon density.

The PDL-3 dye laser was used for most of the experiments. It consists of a single grating (HR) with anamorphic prism, made up of four different prisms positioned and angular aligned to collimate the light output and glued on a breadboard at the Quanta Ray factory, with a specification of 1:25. This breadboard is then locked between the grating and output coupler within the oscillator cavity. The anamorphic prism's telescope the ~1mm seed pulse emitted from the oscillator dye cell to the clear aperture of 25mm onto the grating. The output coupler is a piece of laser grade glass(since the laser needs to be tunable for ~350nm-900nm), with a wedge and AR coated on one side.

The dye cell is made of spectroscopic grade fused quartz with very precise corners. University glass shops will not have the equipment to fix or manufacturer these types of cells. The dye cell offers very low extraneous diffraction from the edges which enhance the pump efficiency and produces a slightly tall mode output with a fan of lines from the edge of the cell. The dye cell is manufactured at Hellma, and the surface

flatness is L/2 with liquid, which is polished many many times as the fused quartz is the strongest glass material[58]. The glass pieces are cut into four sections and polished and placed together to produce a flow thru dye cell. The adhesion that occurs at the corners is done thru molecular diffusion bonding process, and no special epoxies or fine glass particles are used to weld the corners together[58]. The cell uses glass that is sintered and the sintering process begins with the melted quartz material and filtered thru a glass type filter(sinter filter) to strain the large porous materials from the quartz and possibly repeated. The assembled cell is then annealed, by slowly heating and cooling the glass over a long period of time and repeated many many times[58], the annealing process will relieve any internal stress and strengthen the material of the glass.

There are three dye cells, two that are the same size, and a third cell that is ~3x times larger dimensionally. The third dye cell is larger since the beam upon exiting the preamp is saturated for the ~500um spot size and expansion of the beam is required in order to efficiently extract the most energy from the pump beam due to the dye laser's saturation fluence of mJ/cm^2. The beam is collimated with a cylindrical lense placed between the oscillator and the preamp, since the spot size of the oscilllator's gain medium will diverge vertically due to the small spot size. A internal telescope lenses are factory configured to be 4:1 and positioned between the final amplifier stage and the preamp. This allows the dye pulse to be expanded more so that the beam can be amplified more efficiently with typical gain values reaching 2-3 as oppose to 6-8 after the preamp. The PDL-1 uses a thin beam splitter for the pump beam to extract the most

energy out of the dye laser by taking roughly ~10-15% of the pump beam to be placed into the oscillator cell and the preamp cell while the remaining energy is diverted to the final amplifier cell. If greater than 15% is diverted to the oscillator cell then the user could possibly be saturating the oscillator cell, as shown in Fig. 3.1, and inefficiently pumping each of the dye cells.

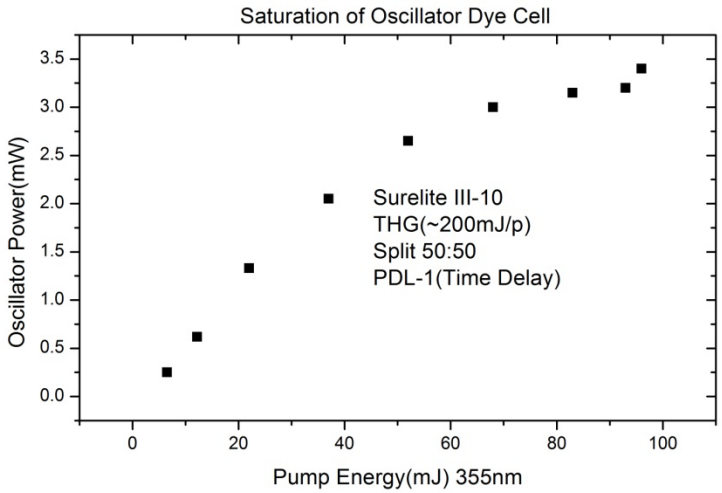

Fig. 3.1 Saturation of the Oscillator Dye cell with the available configured beamsplitter used for the PDL-3.

In most experiments the preamp, which is the same geometrically as the oscillator cell, is avoided since it will amplify the gain and energy of the slit profile and intensify the diffraction of the mode. In addition the preamp is providing another source of light that may possibly come back into the oscillator cavity and provide amplified spontaneous emission that is not coherent to original seed pulse that develop in the oscillator section, and broaden the bandwidth and could also induce a different wavelength to lase than the initial seed oscillator pulse, if a time delay is not provided for pumping the preamp. Hence in order to avoid amplified spontaneous emission the

preamp is blocked by using a card or beam dump and the final amplifier cell is pumped longitudinally. It is well known that when pumping the gain medium with a top hat profile the seed beam will replicate the same shape as the pump beam as shown in the Fig. 3.2 below.

Fig. 3.2 Single shot burn patterns measured on Zap-It burn paper at 486nm mode output from a PDL dye laser with the THG pumped longitudinal pumping. Additional Telescoping Optics were installed in the PDL to narrow the mode diameter to match the mode of the PDL mode output. The Gaussian Output coupler mirror's imprint from a Continuum Surelite, overlap onto the PDL output is observed.

But in addition to pumping longitudinally the final amplifier cell must be dilute enough to fluoresce the entire volume of the cell as there is more gain available within the bulk of the amplifier cell. If the concentration of the dye cell is to large then only the region that gets gain is the front portion of the cell, and the pump as result will not penetrate the entire region of the cell, as shown in the Fig. 3.3 below.

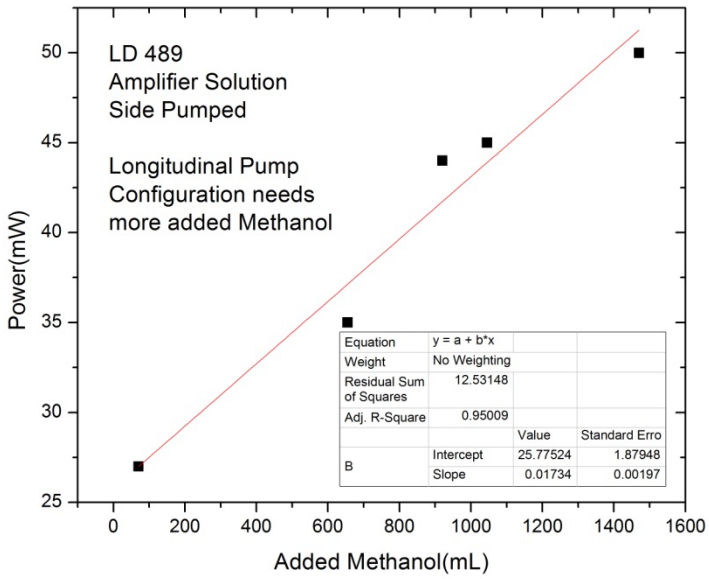

Fig. 3.3 The plot of the recommend dye concentrations is measured to be 27mW with only 50mL of methanol added. Using the same concentration of LD 489, which is needed for side pumped configuration, we add more methanol for longitudinal pumped configuration. Notice the increase in the power output that is available within the volume of the cell.

Also by energizing the entire final amplifier cell you get more gain.

To provide a near circular mode from the oscillator an iris mounted on a x-y translation stage in placed between the oscillator cell and the optical flat used to seal the grating. Or one can use a much more carefully thought out design [59] that gets the most mode and energy out from a dye laser system by using an anamorphic prism set to elongate the slit mode before pumping the final amplifier stage.

The alignment procedure we used was similar to the one provided by Quanta Ray for the PDL-1,2, and 3 manual, where in which the oscillator is first aligned then the final amplifier stage, as oppose to oscillator, preamp, and final amplifier stage.

The PDL dye laser is typically operated in between 2400 and 3000 which is read off of the dial. But it is known that using a different order can produce a bandwidth change of the dye laser. Using the diffraction equation

$$d(sin\alpha + sin\beta) = m\lambda$$

We take the derivative of diffracted angle, β, with respect to the wavelength and solve for $d\beta$ and we get

$$d\beta = \frac{md\lambda}{dcos\beta}$$

This expression in combination with the cavity design of the Quanta Ray PDL series design we can calculate the bandwidth that is restricted along the lasing axis of the dye laser given the original anamorphic prism set and distances set for the grating, anamorphic prism set, dye cell, and output coupler.

Given the bandwidth of the dye fluorescence curve, which is typically 30nm wide, the diffracted/reflected angle we assume is 1 deg at 1st order, and increasing the order used on the grating will increase the angular spread of the fixed bandwidth. The design of the four anamorphic prism dye laser will allow a certain angular spread within the dye laser to lase. Using the grating equation and knowing that amplification of the seed pulse will build for light rays that are reflected back only within the lasing axis for a flat – flat mirror configuration after many round trips, we must then infer that the incident and diffracted angles must be the same and from these two conditions the

angles for the diffracted angle for 1,2,3, and 4th order at 734nm are 12.72, 26.12, 41.35, and 61.74 deg, respectively , which is found from the expression:

$$2dsin\alpha = m\lambda$$

We measured the 1st order bandwidth to be 110Ghz on the grating spectrograph at 486nm. For every 1.05 deg spread there is 110Ghz of the total gain emission curve of 16700 Ghz that lases. This value is 1.05deg/110Ghz = 9.54e-12 deg/Hz. Using this numerical conversion constant we can get the other bandwidths for the different orders in the Table provided below.

Diffracted Angle(B)	d(mm/lines)	M (order)	Cos B	dB (deg)	Freq (BW)	dB/BW (deg/Hz)	dB*(BW/dB)
10	1.666e-6	1	0.9848	1.04			
11	1.666e-6	1	0.9816	1.05			
12	1.666e-6	1	0.9781	1.05	100Ghz	9.54e-12	100Ghz
13	1.666e-6	1	0.9744	1.05			
…	1.666e-6	…	…				
25	1.666e-6	2	0.9063	2.27			
26	1.666e-6	2	0.8988	2.29			45.7Ghz
27	1.666e-6	2	0.891	2.31			
…	1.666e-6	…	…				
41	1.666e-6	3	0.7547	4.10			25.6Ghz
..	1.666e-6	…	…				
60	1.666e-6	4	0.5000	8.25			
61	1.666e-6	4	0.4845	8.5			
62	**1.666e-6**	**4**	**0.4695**	**8.78**			**11.9Ghz**

Table 3.1 of Bandwidths for a Quanta Ray series PDL with Grating set at different orders. The "…" symbols are for angles in between the different sets. The dye that is used LDS 751 in a PDL-3 dye laser.

The PDL Quanta Ray is made up of a grating oriented at a grazing incidence angle. The grating itself made of a Fused Silica Glass substrate in which a tiny diamond tipped cutter is drawn across the grating in a scanning HeNe laser interferometer controlled xyz

stage. The grating is in a sense a mirror, and with a length of 50mm and a density of 600 lines/mm as a result has 30000 lines that are illuminated. Given the length of the cavity is 100cm the FSR of the single grating dye laser is 600Mhz, then it is estimated that the dye laser has 20 modes within a 0.005nm bandwidth. The gain medium is made up of a solvent with a laser dye circulating thru the Dye Cuvette at 1ft/sec. It is known that the refractive index of the dye exhibits fluctuations in the liquid during the flow and these fluctuations as a result perturb the frequency output of the dye laser and in addition couple the spatial transverse laser modes in the initial seed pulse. The frequency of the dye laser as a result jumps in a random fashion as shown in Fig. 3.4 for the PDL at 1st order on the grating.

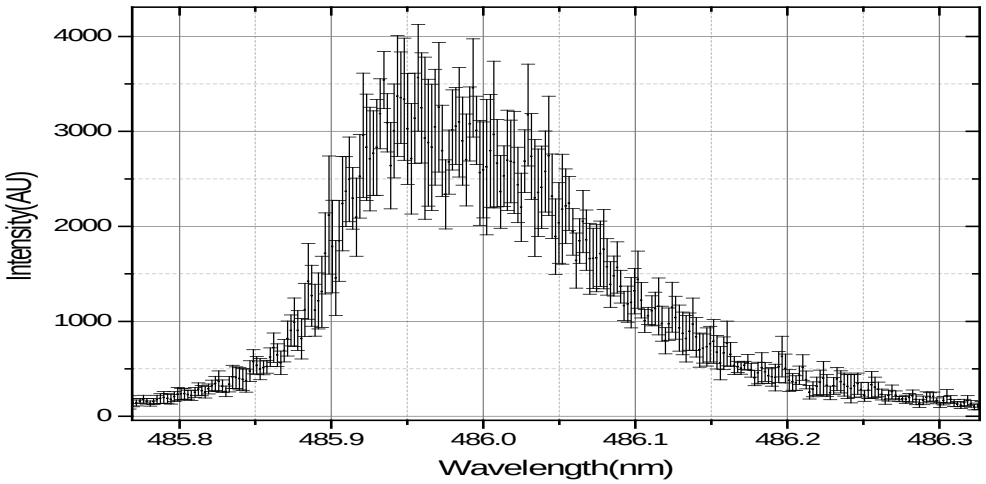

Fig. 3.4 10 single shot wavelengths averaged with SD Error bars plotted. The measurement was done on a 0.75m Cznery Turner Grating Spectrometer converted into a Spectrograph with the entrance slit set at 10um. The Grating in the spectrometer has 1200 lines/mm with a 4"x4" aperture. The Dye laser grating is set a 2nd order. Notice the larger Error bars are much larger within the middle region of the bandwidth. This demonstrates the spurious hole burning effects and random nature of the multimode output of the dye laser. The x-axis is calibrated using an Argon Ion lamp, and can also be calibrated with the 821 Burleigh/Bristol Wavemeter.

The YAG we used was a Continuum Surelite III-10 and/or Surelite I-20, as the YAG series is a capable of running 1-2 months straight 24 hours a day with virtually no adjustments needed, once the nonlinear crystals are carefully optimized and enclosure temperature stabilized to within ± 2 deg. The YAG laser was positioned as close to the dye laser as possible as the mode from the YAG is the best when closest to the dye laser and as result in longitudinally pumping the final amplifier cell will amplify the dye cell with a circular mode assuming a near circular mode from the dye laser. Each Surelite YAG came with temperature controlled KD*P SHG Type I and THG Type II nonlinear harmonic

generating crystals. With 920mJ/p of 1064nm of fundamental the amount of 532nm light converted was about 300mJ from the type I crystal. At THG there is 240mJ/p of 354nm light. With 240mJ/p of 354nm light the horizontally polarized pump beam is rotated to s-polarization, since the Hertzian oscillating dipole model the power emitted over the solid angle has a $(sin\theta)^2$ dependence. Typically we can get about 15-20mJ/p of 486nm light using the LD 489 dye. The recipe for the concentration is either on the Exciton website or is well documented in the PDL-3 manual. We used 408mg/li for the oscillator and 108mg/li for the amplifier stage. The final amplifier stage must be dilute to 30mg/li if the mode is pumped longitudinally in the final amplifier cell. The dye concentration with the most energy requires the final amplifier cell to be pumped from the side. The PDL-3 that we have includes a cylindrical reflecting 355 mirror made just for side pumping the final amplifier cell. Side pumping is needed if more energy is required for experiment as LD 489 is considered a low gain dye.

The dye lasers were purchased from Dick Anderson at Anderson Laser's/ DNA Equipment Inc. Ken James had the unique idea of purchasing the MC-1 controller with the PDL's dye laser. This allowed us to rotate the grating on the dye laser using the internal stepper motor instead of manually rotating the grating by hand. The MC-1 , when used with the Hand Control Box, allowed for quickly rotating the original stepper motor attached to the dye laser that rotated the grating inside the oscillator cavity. The MC-1 also offered a way of quickly tuning to the peak of the dye gain curve and also switching to different orders on the grating.

I attempted to first try the MC-1 controller. The MC-1 controller had two computer controlled options when originally bought in the late 1970's. The first option was the parallel line I/O interface that uses 12 parallel output lines in between the MC-I system and the computer. The MC-1 is configured to operate with the Digital Equipment Corporation, Model PDP-11, which is a16 bit minicomputer that comes with a DRV11 16 bit parallel line interface, and without modification and no special programming instructions. We did not purchase or find a refurbished Digital Equipment computer PDP-11. The opto - codes and coding language are provided with the PDP-11 microcomputer in the PDL-1 manual. The 2nd option is the IEEE-488 configuration for the MC-1 which uses the 1975 standard instructions, but we have not checked if the MC-1 control module has the IEEE-488 card installed. I concluded the MC-1 required another computer that had the 1975 IEEE-488 code. But at this point another quicker solution seemed more practical but with a bit more work in identifying the components of the MC-1 and trouble shooting the opto-codes and wiring it can be solved, but we desired the computer controlled tuning that integrated with Labview instead.

We then communicated directly with the stepper motor that was integrated into the PDL-1 laser by using TTL pulses that were turned on and off in a specific sequence for the Unipolar Two Phase Stepper Motor. The motor was tunable using four high current transistors that were gated from the LabView DAQ card using a digital output which produces TTL pulses sent to the transistor's gates. We identified the wiring

needed to communicate to each pole of the stepper motor. But we found after some time spent that each step was too large and inaccurate in repeated rotations.

We then decided to use a SLA7070 or SLA7071 IC Unipolar, 2 Phase Step motor driver chip to control the dye laser stepper motor. The chip was at a low cost, roughly $6 / chip and had the ability to convert the 8 steps into 32 steps, which converted the course sinusodial wave into a more finer sinusodial wave, but the wiring and instructions provided were less than trivial. With enough time and experience spent in troubleshooting each of the components it was possible to use this method as a working low cost solution for tuning the dye laser.

The wavelength's were measured using two instruments. The SPEX 0.75m diffraction grating spectrometer and the 821 pulsed wavemeter. The spectrometer was first used to measure the wavelength. Ken James had the idea of integrating the grating spectrometer to automatically measure the wavelength through LabView. The idea we initially used was a reference wavelength, HeNe, and the dye laser sent into the spectrometer and plotting the HeNe and Dye laser intensities vs wavelength. But due to the hysteresis of the bevel gears underneath the spectrometer and the data rate recording requirements the idea was less than desirable. Initial attempts to record the intensity vs wavelength were poor and due to the numerous times the spectrometer needed to scan both wavelengths, this increased the hysteresis since the bevel gears were slowing degrading over time. An improvement was made by switching to higher grade stainless steel bevel gears. This improved the repeatibilty of the scans. But it was

still evident that degradation of the steel bevel gears would slowly degrade over time. At this point two problems were discovered. One was the repetition rate of the experiment required the laser to fire at 1-10Hz frequency in order to plot the intensity of the measured light vs the wavelength that is scanned within the spectrometer. Second, the time required for the spectrometer to scan across a set of reference lines and the unknown wavelength of the dye laser required speeds that were not feasible within a 2 minute time period. We then decided to measure the wavelengths by hand for the first experiment.

The scanning for the spectrometer implemented a Lin Controller Stepper Motor, Silverpak 17CE. This item came with the stepper motor, Driver and a US Digital E2 wheel encoder. The 17CE was first integrated with the spectrometer by rotating the grating in the SPEX 0.75m spectrometer, and measuring the intensity vs the wavelength. But since wavelength measurements were done by hand, and we accomplished the task of training with the 17CE stepper motor we decided to transfer the stepper motor to the PDL dye lasers. A rectangular aluminum tube was used to elevate the height of the 17CE motor and clamp the motor down to the optical table. A rigid shaft rod coupler with bushing was then used to mechanically connect both the 17CE motor to the PDL's shaft. The rod/shaft of the PDL is connected to the handknob that manually tunes the dye laser. The hand knob was removed in order to attach the 17CE. The 17CE has an additional apparatus called the"optical gate" that emits a light across the photo gate. If

blocked the driver/controller of the 17CE sends a command to “home” the stepper motor and rotate until the optical gate is blocked.

In conclusion I successfully integrated the automatic tuning of the PDL-1 and SHG phase matching crystal with the 0.007Hz High density Ps pulser for most of the experiments with Labview at this point. The next possible upgraded version is incorporating the PCI-4E card which is a controller that keeps track of the rotational position and direction of the motor using the E2 encoder that is integrated with the17CE stepper motor. The following flow chart in Fig. 3.5 is used for Labview programming and was demonstrated to work with Labview. Further work is needed to integrate the Labview program with current Ps optical spectroscopy experiments.

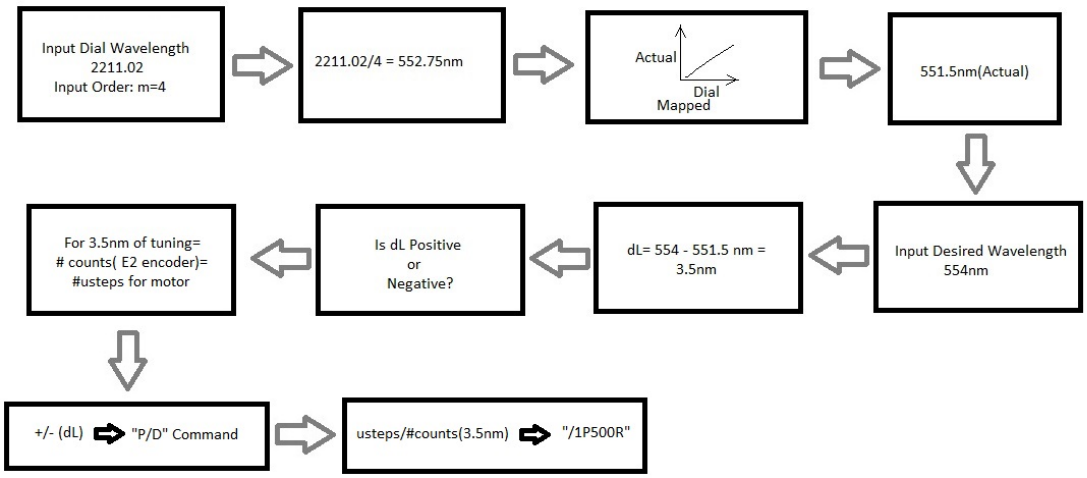

Fig. 3.5 Flowchart for auto tuning to the select wavelength.

Another parameter that we measured is the wavelength drift from shot to shot using the 821 wavemeter. In Fig. 3.6 is a sample of a 5 hour run with the dye laser operating at 4th order on the grating. The accuracy of the wavemeter is specified to be $\pm 600\ Mhz$ at 800nm. A drift of 0.0018nm was measured within the temperature controlled laser enclosure.

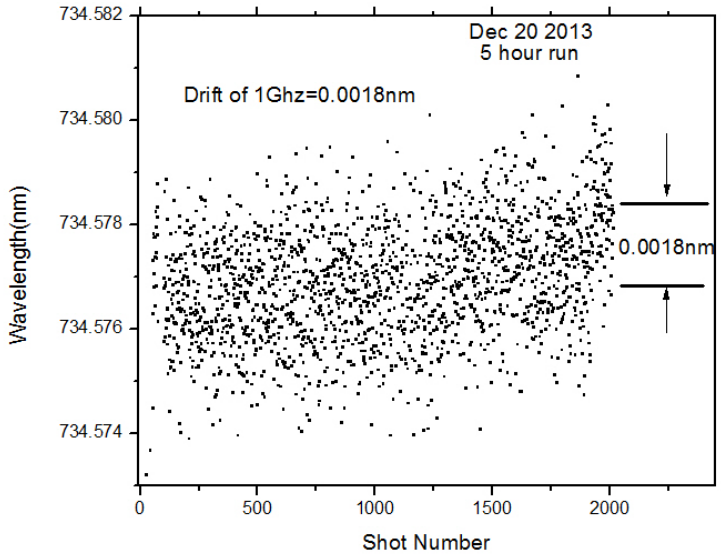

Fig. 3.6 Plot of the measured wavelengths obtained from a 821 wavemeter, with the Q-switch of the Nd:YAG firing at a rate of 1 shot every 10 seconds over a time period of 5 hours at 4th order on the dye grating.

The pulse width was measured on an EOT-2030 PIN Silicon photodiode with the light directed on to the 0.4mm diameter head with a rise and fall time of less than 0.3ns. The output was connected to an Agilent Digital Oscilloscope with a 6 Ghz bandwidth, and a sampling rate of 20Gs/s. In Fig.3.7 below shows the multi-mode output that

corresponds to the 20 different modes that have the highest gain within the 10Ghz bandwidth of the 486nm light.

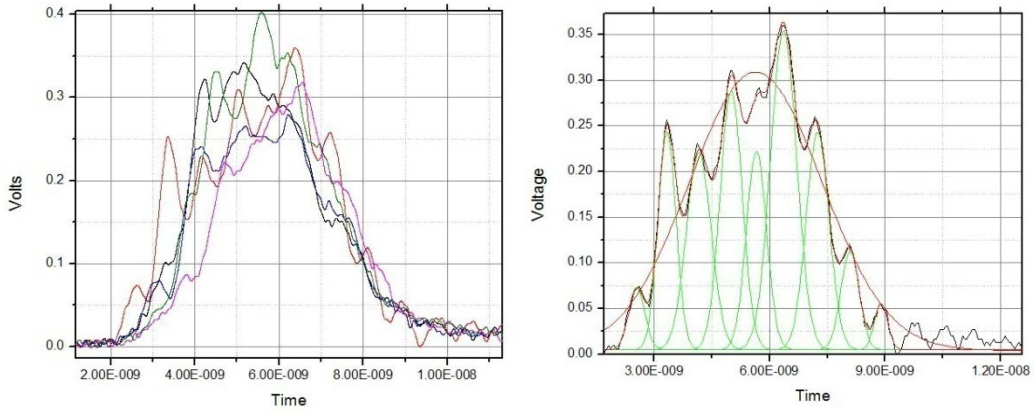

Fig. 3.7 Measured Pulse width from a PDL laser. The figure on the lefthand side is a plot of five shots. Notice the from shot to shot shows the different modes that corresponds to different wavelengths within the gain curve that are building up in the PDL oscillator are random. The figure on the right hand side is a single shot. There are about 8 modes in the time profile shown on the right, if the dye laser was seeded for single frequency output the trace would produce a single smooth Gaussian plot.

The dye laser cavity alignment can cause the seed pulse to have a lower threshold for lasing output, hence the optimum amount of energy will not be extracted from the PDL laser. When the pump beam position into all three dye cells are optimized and the front output coupler and cylindrical lenses are positioned, rotated, and aligned to each cell the best alignment of the dye oscillator is known to occur when the pump power threshold is at its lowest value, as shown in Fig. 3.8.

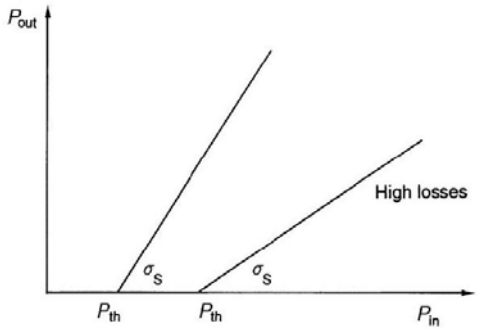

Fig. 3.8 Figure adapted from [60]. Plot of the output power vs. the input pump power. Notice the threshold for lasing is shifted to the left, which indicates lower losses compared to the trace for higher losses. A good alignment of the pump beam position and mirrors for the cavity will produce the lower lasing threshold. σ_S is the slope efficiency defined by Koechner.

When the threshold is at its lowest value, which indicates good to perfect alignment of the cavity, it is known to produce the energies that the manufacturer has specified [61].

As the Pockel cell switches open the losses are lowered beneath the gain curve, as a result the power build up or population inversion depletes in a very short time, and the Nd:YAG produces a 6-8ns long 1064nm pulse within a Continuum Surelite.In combination with the short THG pulse obtained from the YAG and the short fluorescence time of the dyes, which is typically in the ns, the dye laser time pulse width is also on the same order as the pump Nd:Yag pulse time width.

Lastly the dye medium is considered a high gain material and as a result the output coupler does not need to have a high reflective coating, usually within the 90% range, for this reason the output coupler is specified with no coating, expect the AR coating needed for the opposite side of output coupler. The time profile of the dye pulse depends essentially on the risetime of the YAG's q-switch.

3.2 Sum Frequency Generation or Second Harmonic Generation in the Lab

The dye lasers tuning range can be extended using nonlinear optical crystals by second harmonic generation of the fundamental light into the UV range. Other frequency mixing techniques such as sum frequency mixing or difference frequency mixing can be used for generating UV wavelengths if the fundamental energy used in second harmonic generation is lower than the other available mixing combinations such as 355nm and 772nm. For both Quanta Ray PDL's laser systems I had added a couple of tuning SHG module's to each dye laser system. The SHG module is a stand-alone device that rotated a nonlinear crystal that was developed independently from the tuning PDL laser system. Integrating both the nonlinear SHG crystal with the Dye laser tuning was done thru Labview and required tuning one element to the other and performing the experiment with both operating synchronously by first receiving a TTL trigger pulse from the high density Ps pulser. The same TTL trigger pulse was used to fire the Q-switch and initiate the stepper motor to tune to the next wavelength on the dye laser and rotate to the corresponding phase matching angle for the nonlinear crystal for generating 243nm light.

The BBO crystal was one selectively bought by Peng Wan, who initially used the nonlinear crystal for pulse picking. The crystal was purchased from Foctek. The dimensions of the crystal are 6x6x10mm BBO Type I nonlinear crystal. The BBO crystal is hygroscopic, so the crystal will tend to fog in the lab if humid (moisture in the air)

enough, but the front and back face's of the crystal are AR coated. The front AR coating was specified for sum frequency generation of 355+ 740-780nm light. The back face was AR coated for 230-250nm light. The damage threshold values are determined by the AR coating, which is 600MW/cm^2, the polished surface's of the front and back portion of the crystal, and the internal bulk lattice of the crystal itself. It's known that the bulk damage threshold values are larger than the surface damage threshold values[60]. But since any of these three items are in the beam's path, then the weakest damage threshold value will determine the damage threshold for the entire module itself, assuming the laser beam itself is collimated. Using 600MW/cm^2 as the damage threshold, we obtain with a 1.5mm diameter spot size and a 5ns pulse width, a maximum energy value of 50mJ/p. Assuming an additional safety factor of two, to reduce our risk for damaging the crystal, we use 25mJ/p instead of 50mJ/p.25mJ/p * 10Hz is 250mW, which is the maximum power that needs to be avoided on the power meter.

This crystal was mounted in a dust free Cell with the front window angled at Brewster's angle. The front window was a CVI Suprasil Brewster window. The back window was a UVGFS laser grade window AR coated at 248nm on both sides. The back window was mounted with a single rubber o-ring seal on both sides of the window. During the installation of the BBO crystal inside the cell, in which the crystal's front surface was aligned perpendicular to the z-axis of the cell, both the cell and the BBO crystal were purged with Helium gas/Nitrogen Gas. The BBO crystal was mounted on a

CVI grade laser window made of UV grade Fused Silica that was cut in half in the Glass shop. The idea of mounting the crystal onto a glass platform was first suggested by Xiaojing Tan, since the dye laser beam could possible clip the BBO crystal in its mount and vaporize the material that the crystal was mounted on and cloud the front and back surfaces of the crystal which would reduce energy transmitted thru the cell. In addition the thermal insulation provided by a glass platform prevents additional thermal drift which could shift the SHG phase matching angle and decrease the amount of SHG energy. Though the power delivered to the BBO crystal is less than 0.5W for a YAG fired at 10Hz , the concern for the crystal heating up was not relevant since the positronium pulse was fired at a rate of 0.007Hz, in addition the index of refraction is insensitive to small temperature changes. For example, at T=293K for generating second harmonic light at 266nm from 532nm in a Type I crystal cut at 47.3 deg has a $d\theta_{pm}/dT \ \ [deg/K]$= 0.0025 for BBO[62].For generating 243nm light the crystal is cut at 58.3 deg and has a $d\theta_{pm}/dT \ \ [deg/K]$ =0.00421[62]. We make a rough estimate at 243nm that $d\theta_{pm}/dT$ is 0.004 deg/K and within the laser enclosure there is a temperature change of roughly +-2deg. So assuming a 2 deg temperature shift the phase matching angle value will change about 0.008 deg. The smallest rotational increment for the closed loop rotational stage is 0.008 degrees. Other nonlinear crystals have much more sensitive changes to temperature in the phase matching angle, for example KDP has a value of 0.0382 deg/K. So a 2 deg temperature shift will change the phase matching by 0.080 deg[63], as a result the crystal would have to be adjusted using

a feedback control loop to compensate for the drop in the energies. Our entire SHG module itself was fabricated in 2009 and is still in use as of 2014 with the same rated conversion efficiencies.

The cell was machined in the Student Machine shop using a lathe to achieve the cylindrical shape and a milling machine with a sine bar to cut the front portion of the cell at Brewster's angle. Having a Brewster angle input allowed for near 100% transmission of light at all wavelengths, ignoring the internal bulk absorption of the Brewster window itself. The polarization of the input light into the cell needed to be p-polarized(vertically), and that is accomplished by placing a piece of paper in front of the cell and lying flat to block the light reflected off the Brewster window and rotating the polarization until the light that is scattered off of the paper has reached a minimum.

The crystal was then mounted on a New Focus 8410 closed loop motorized rotational stage. The ability to rotate within 0.010 deg accuracy is a standard feature necessary for rotating the BBO's phase matching angle. The accuracy specification indicates that the rotational mount may rotate to 367 degrees away from the initial home angle of 1.008 deg, and rotate back to the home angle within ± 0.010 deg in one move. The closed loop rotational mount was controlled through Labview.

In the lab technically it is very difficult to find the exact phase matching angle to generate Lyman Alpha photons, assuming the linewidth of the laser is very small. The dye laser produces a linewidth of roughly 10Ghz or 0.008nm at 6^{th} order on the dye grating at 486nm. The laser bandwidth that can be converted to SHG light in the

nonlinear crystal must be rotated to a specific phase matching angle to within $\pm$0.03deg. By searching for the second harmonic generation of light we would rotate the BBO crystal in its mount to roughly 60 deg or 56 deg, and then rotate the crystal slowly until we reach 58 deg. If the HeNe light reflected off the front face of the BBO crystal, is reflected normal to the surface, this indicates that the input light is going into the crystal at 58 degs, as the crystal is cut at the factory at 58 degrees.

But we must be careful to not rotate in course intervals or too quickly as one may miss the SHG light generated in the lab. If you had a 12nm wide bandwidth laser then you have roughly +-5 deg tolerance to generate the SHG light at 800 nm so the accuracy needed for a smaller bandwidth laser increases by a factor of 500. It is known that any type of nonlinear crystal is grown, cut, and polished to exact specifications desired by the customer. When one receives the SHG nonlinear crystal from the Manufacturer the company will specify the angle but it is a good rule of thumb that the cut is within ± 0.1 degree, so we did not expect the phase matching angle to be good within the state accuracy of 0.01 deg. For practical purposes and time a neat trick that was borrowed from design of the Alexandrite laser optical mounts, is placing the crystal and cell in a standard 1" or 2.0" Kinematic Mirror Mount with the Nonlinear crystal mounted. The 2.0" mirror mount has a 1.5" arm that rotates about a stationary fixed point. The threads per inch (tpi) for the two adjuster knobs on the mirror mount have 80tpi. So one revolution angularly rotates the crystal on a very fine scale, in addition to the small order translation movement, which is on the order of um. So, 1/80" over an

arm that is 1.5” long means, using $S = r\theta$, we obtain an angular rotation of 8.333mrad, which is around 0.5 deg. The Closed Loop Rotational stage,CLRS, has a resolution of 0.010deg. So the mirror mount is equivalent to a CLRS with one turn on the knob being equivalent to 50 adjustments. So this estimate is a very neat trick to enable one to obtain a very accurate and very fine CLRS using a standard 2.0” Two Adjuster Kinematic mirror mount, and it is quite possible to attach a computer controlled stepper motor, such as the Lin Motor 17CE to replace the adjustment knob, in order to rotate the crystal’s phase matching angle at a low cost with no weight restriction.

In the lab this enables one to quickly find the phase matching angle of a crystal quickly instead of using a manually adjusted standard rotational stage with a course resolution such as 0.1 degree. In addition It is a also a good rule of thumb that in quickly aligning the SHG crystal that one would aim generally in the center of the front and back window and use a lens tissue to observe the shadow of the SHG crystal on a white bond card(3”x5” index card) to align the beam close to the center of the BBO crystal at low power.

Communication between the closed loop rotational stage and the dye laser can be lost and as a result the phase match angle must be found and reset to 486.04nm. The angle can be found very quickly using a HeNe beam and two irises. Using two irises will also enable one to find the phase matching angle when a realignments performed on the dye laser transversely offsets the beam’s position and input angle onto the BBO crystal. Here are the following steps.

1) Mount a HeNe laser such that beam height is approximately level with the entire SHG module .
2) Find two irises and take one iris and align to the HeNe beam's height. Then take the same iris and check that the HeNe beam is at the same height 1m away. One can go to 2m or 4m but table space is a premium so 1m is enough.
3) If the HeNe beam is not leveled then one mirror is needed to level the height so that the height is the same for 1m separation distance.
4) Then plant two irises at the specific location that enables access to the SHG module and set the irises 1m apart.
5) Then using the HeNe beam that is going thru the two irises, place the SHG module into the path of the HeNe beam in between the two irises.
6) Once the phase matching angle for SHG is found then using the HeNe or Dye laser beam aimed at the SHG module record the reflected angle of the HeNe beam with respect to the first iris. This is will save a lot of time in resetting the closed loop rotational stage if the communication between the CLRS and computer is lost and a new IP address is needed to reset the closed loop driver.

Sum Frequency and Second Harmonic Generation and Phase matching Angles

The Beta Barium Borate (BBO) is a transparent, cut, and polished nonlinear crystal belonging to the class 3m, a class 3m crystal is discussed in the section Nonlinear

susceptibility. The nonlinear crystal enables us to generate the UV specific wavelength range at a low cost by inputting a high energy ns laser pulse and frequency converting within the crystal itself. The refracting index n of the crystal is a function of the electric field or intensity of the photon's and is expressed as:

$$n(E) = n_o + n_1 E + n_2 E^2 + \cdots$$

In nonlinear optics the dipole moment of the unit volume is defined as the dielectric polarization P. The electric field vector E is related to the polarization by:

$$P(E) = \kappa_o E + \chi^{(2)} E^2 + \chi^{(3)} E^3 + \cdots$$

κ_O is the dielectric susceptiblitly constant, $\chi^{(2)}$ and$\chi^{(3)}$ are the nonlinear susceptibility coefficients, where the cubic nonlinearity $\chi^{(3)} \ll \chi^{(2)}$. Two monochromatic waves with frequencies f_1 and f_2 in a crystal with a $\chi^{(2)}$ terms forms a new photon with combination frequencies $f_{3,4} = f_1 \pm f_2$. Each photon defines a k-vector and the wavelength range is 185-2600nm for BBO. The phase matching condition for Sum Frequency Mixing, for example 355nm + 772nm is given by the following condition:

$$\overrightarrow{k_1} + \overrightarrow{k_2} = \overrightarrow{k_3}$$

or

$$\Delta k = 0 \quad \rightarrow \quad \overrightarrow{k_1} + \overrightarrow{k_2} - \overrightarrow{k_3} = 0$$

This condition is met by rotating the nonlinear crystal until the following expression (1) is satisfied. Since $k = n(\omega) \cdot \omega / c$ then,

$$n_1\omega_1 + n_2\omega_2 = n_3\omega_3 \quad (1)$$

The BBO crystal is of Type I, meaning the polarization of the input light must be:

$$o + o = e \Rightarrow n_{1o}\omega_1 + n_{2o}\omega_2 = n_{3e}\omega_3$$

This leads to

$$\frac{n_{1o}}{\lambda_1} + \frac{n_{2o}}{\lambda_2} = \frac{n_{3e}}{\lambda_3}$$

Using the equation for the index ellipsoid

$$\frac{sin^2\theta}{n_e^2} + \frac{cos^2\theta}{n_0^2} = \frac{1}{n_e^2(\theta)}$$

we can combine the two recent equations above and restate as[62]:

$$\frac{sin^2\theta}{\frac{n_{3e}^2}{\lambda_3^2}} + \frac{cos^2\theta}{\frac{n_{3o}^2}{\lambda_3^2}} = \frac{1}{\frac{n_{1o}^2}{\lambda_1^2} + \frac{n_{2o}^2}{\lambda_2^2}}$$

The right side of the expression is for the SFM input and as result we change the angle of the crystal to find what $n_o(\omega) = n_e(2\omega)$ inside the BBO crystal, since

$$\Delta k = 0 = \frac{4\pi}{\lambda_o}\,(n_o(\omega) - n_e(2\omega))$$

Converting the equation with the $sin\theta$ and $cos\theta$ terms into only $tan\theta$ it is straight forward to work out the steps to find the expression

$$tan\theta = \frac{1 - A}{B - 1}$$

Where

$$A = \frac{\frac{n_{1o}^2}{\lambda_1^2} + \frac{n_{2o}^2}{\lambda_2^2}}{\frac{n_{3o}^2}{\lambda_3^2}} \quad , \quad B = \frac{\frac{n_{1o}^2}{\lambda_1^2} - \frac{n_{2o}^2}{\lambda_2^2}}{\frac{n_{3e}^2}{\lambda_3^2}}$$

Sellmier Equation for BBO

Using the Sellmier equation for the BBO crystal one can then plug in for the given λ_1,λ_2, and λ_3 to find the corresponding phase matching angle for the crystal to obtain 243nm using SHG or SFM for a Type I crystal. The Sellmier equations are given below[64].

$$n_o(\lambda) = \sqrt{2.7359 + \frac{0.01878}{\lambda^2 - 0.1822} - 0.01354\,\lambda^2} n_e(\lambda)$$

$$= \sqrt{2.3753 + \frac{0.01224}{\lambda^2 - 0.01667} - 0.01516\,\lambda^2}$$

3.3 Nonlinear Susceptibilty term

The power generated from 2nd harmonic generation can be found from the following expression, in the small signal limit:

$$P_2 = \frac{2\pi^2 d_{eff}^2 L^2 P_1^2}{\varepsilon_o c n_1^2 n_2 \lambda_2^2 A} sinc^2(|\Delta k|\mathrm{L}/2) \quad (1)$$

The conversion efficiency can be defined as P_2/P_1. With the condition $\Delta k = 0$, i.e. phase matching is rotated for the nonlinear crystal, the other three parameters: length, spot size , and nonlinear susceptibility term can be adjusted properly for generating the most energy. The Second Harmonic generation of light is produced in a BBO Type I(ooe) nonlinear crystal. The phase matching angle is discussed in the SFM mixing chapter. The efficiency can increased by decreasing the beam diameter to smaller values but is limited by the Peak Power which is determined by the expression: $PeakPower =$

$\frac{Energy}{Areaofbeam} * \frac{1}{time}$. Peak power is specified by the AR coating, which is $600 Mw/cm^2$. Using a 5ns pulse the value is then given as $3 J/cm^2$. We found from previous chapters that a 1.75mm diameter is the smallest diameter to produce 25mJ/p without any damage. But with a 1.75mm beam diameter the beam will walkoff inside the crystal at 243nm. The walkoff angle is given as:

$$\rho(\theta) = \pm \arctan[\left(\frac{n_o}{n_e}\right)^2 tan\theta] \mp \theta$$

which is around 4 degrees at 243nm. The other parameter is the length of the crystal. The amount of SHG energy will saturate and is limited by the input energy, so no matter the length of the crystal it's not possible to produce more than roughly 30% of the input energy at 243nm. The next term that can influence the converted efficiency for SHG is proportional to the nonlinear susceptibility term d_{eff} or χ_{eff}. Using Shen's notation the double dot product is calculated by the following steps, where $\hat{e}$ is a unit vector:

$$\chi_{eff} = \hat{e}_3 \cdot \chi^{(2)} : \hat{e}_1 \hat{e}_2$$

χ_{eff} can be expressed as:

$$\chi_{eff} = \hat{e}_{3a} \cdot \chi^{(2)}{}_{abc} : \hat{e}_{1b} \hat{e}_{2c}$$

$$\sum_{bc} \chi_{abc} \hat{e}_{1b}\, \hat{e}_{2c}$$

$$b = x, y, z c = x, y, z$$

$$\chi^{(2)} = \chi_{axx} e_{1x} e_{2x} + \chi_{axy} e_{1x} e_{2y} + \chi_{axz} e_{1x} e_{2z} +$$

$$\chi_{ayx} e_{1y} e_{2x} + \chi_{ayy} e_{1y} e_{2y} + \chi_{ayz} e_{1y} e_{2z} +$$

$$\chi_{azx} e_{1z} e_{2x} + \chi_{azy} e_{1z} e_{2y} + \chi_{azz} e_{1z} e_{2z} +$$

$\hat{e}_1 = \hat{e}_2 = (sin\phi, -cos\phi, 0)$ implies that $e_{1z} = e_{2z} = 0$, so the expression above reduces to

$$\chi^{(2)} = \chi_{axx}e_{1x}e_{2x} + \chi_{axy}e_{1x}e_{2y} + \chi_{ayx}e_{1y}e_{2x} + \chi_{ayy}e_{1y}e_{2y}$$

$$\chi_{eff} = \hat{e}_{3a} \cdot \chi^{(2)}{}_{abc} = \hat{e}_{3a} \cdot (\chi_{axx}e_{1x}e_{2x} + \chi_{axy}e_{1x}e_{2y} + \chi_{ayx}e_{1y}e_{2x} + \chi_{ayy}e_{1y}e_{2y)}$$

The "a" subscript implies a summation:

$$\chi_{eff} = \sum_a e_{3a} \cdot (\chi_{axx}e_{1x}e_{2x} + \chi_{axy}e_{1x}e_{2y} + \chi_{ayx}e_{1y}e_{2x} + \chi_{ayy}e_{1y}e_{2y)}$$

$$\chi_{eff} = e_{3x} \cdot (\chi_{xxx}e_{1x}e_{2x} + \chi_{xxy}e_{1x}e_{2y} + \chi_{xyx}e_{1y}e_{2x} + \chi_{xyy}e_{1y}e_{2y)} +$$

$$e_{3y} \cdot (\chi_{yxx}e_{1x}e_{2x} + \chi_{yxy}e_{1x}e_{2y} + \chi_{yyx}e_{1y}e_{2x} + \chi_{yyy}e_{1y}e_{2y)} +$$

$$e_{3z} \cdot (\chi_{zxx}e_{1x}e_{2x} + \chi_{zxy}e_{1x}e_{2y} + \chi_{zyx}e_{1y}e_{2x} + \chi_{zyy}e_{1y}e_{2y)}$$

BBO is a (3m) crystal and according to the crystal definition for the second number on d_{21}, which is 1, we then use the following

1=xx , 2=yy , 3=zz , 4=yz , 5= xz , 6=xy

For example $d_{21} = d_{2xx} = d_{yxx}$

BBO is a Trigonal Crystal in the crystal class: 3m. The nonvanishing tensor elements are:

$$xzx = yzy \quad xxz = yyz \quad zxx = zyy, zzz \quad yyy = -yxx = -xxy = -xyx$$

For BBO the tensor for d_{il} is:

$$d_{il} = \begin{bmatrix} 0 & 0 & 0 & 0 & d_{15} & -d_{16} \\ -d_{21} & d_{22} & 0 & d_{24} & 0 & 0 \\ d_{31} & d_{32} & d_{33} & 0 & 0 & 0 \end{bmatrix}$$

d_{il} is equivalent to χ_{eff} due to different notations.

$$\chi_{il} = \begin{bmatrix} \chi_{xxx} & \chi_{xyy} & \chi_{xzz}\chi_{xyz} & \chi_{xxz} & \chi_{xxy} \\ \chi_{yxx} & \chi_{yyy} & \chi_{yzz}\chi_{yyz} & \chi_{yxz} & \chi_{yxy} \\ \chi_{zxx} & \chi_{zyy} & \chi_{zzz}\chi_{zyz} & \chi_{zxz} & \chi_{zxy} \end{bmatrix}$$

$$= \begin{bmatrix} 0 & 0 & 0 & 0 & \chi_{xxz} & \chi_{xxy} \\ \chi_{yxx} & \chi_{yyy} & 0 & \chi_{yyz} & 0 & 0 \\ \chi_{zxx} & \chi_{zyy} & \chi_{zzz} & 0 & 0 & 0 \end{bmatrix}$$

We know can find which terms in χ_{eff} are zero.

$$\chi_{eff} = e_{3x} \cdot (\chi_{xxx}e_{1x}e_{2x} + \chi_{xxy}e_{1x}e_{2y} + \chi_{xyx}e_{1y}e_{2x} + \chi_{xyy}e_{1y}e_{2y)} +$$

$$e_{3y} \cdot (\chi_{yxx}e_{1x}e_{2x} + \chi_{yxy}e_{1x}e_{2y} + \chi_{yyx}e_{1y}e_{2x} + \chi_{yyy}e_{1y}e_{2y)} +$$

$$e_{3z} \cdot (\chi_{zxx}e_{1x}e_{2x} + \chi_{zxy}e_{1x}e_{2y} + \chi_{zyx}e_{1y}e_{2x} + \chi_{zyy}e_{1y}e_{2y)}$$

$$\chi_{eff} = e_{3x} \cdot (\quad 0 \quad + \chi_{xxy}e_{1x}e_{2y} + \chi_{xyx}e_{1y}e_{2x} + \quad 0 \quad) +$$

$$e_{3y} \cdot (\chi_{yxx}e_{1x}e_{2x} + \quad 0 \quad + \quad 0 \quad + \chi_{yyy}e_{1y}e_{2y}) +$$

$$e_{3z} \cdot (\chi_{zxx}e_{1x}e_{2x} + \quad 0 \quad + \quad 0 \quad + \chi_{zyy}e_{1y}e_{2y})$$

The zero terms have been found and χ_{eff} reduces to:

$$\chi_{eff} = e_{3x}(\chi_{xxy}e_{1x}e_{2y} + \chi_{xyx}e_{1y}e_{2x}) + e_{3y}(\chi_{yxx}e_{1x}e_{2x} + \chi_{yyy}e_{1y}e_{2y})$$

$$+e_{3z}(\chi_{zxx}e_{1x}e_{2x} + \chi_{zyy}e_{1y}e_{2y})$$

Using the unit vector definitions:

$$\hat{e}_3 = [-cos\theta cos\phi, -cos\theta sin\phi, sin\theta]$$

$$\hat{e}_1 = \hat{e}_2 = [-sin\phi, -cos\phi, 0]$$

We can now substitute the terms back into the expression and replace χ_{ijk} with d_{il}

$$\chi_{eff} = e_{3x}(\chi_{xxy}e_{1x}e_{2y} + \chi_{xyx}e_{1y}e_{2x}) +$$

$$e_{3y}(\chi_{yxx}e_{1x}e_{2x} + \chi_{yyy}e_{1y}e_{2y}) + e_{3z}(\chi_{zxx}e_{1x}e_{2x} + \chi_{zyy}e_{1y}e_{2y}$$

Upon substitution of the variables we get

$$\chi_{eff} = -cos\theta cos\phi(-d_{22}(-sin\phi)(-cos\phi) - d_{22}(-cos\phi)(-sin\phi))$$

$$+(-cos\theta sin\phi)\big((-d_{22})sin^2\phi + d_{22}cos^2\phi\big) + sin\theta(d_{31}sin^2\phi + d_{31}cos^2\phi)$$

$$\chi_{eff} = d_{22}cos\theta[sin3\phi] + d_{31}\sin\theta$$

The values are $d_{22} = 2.22\text{pm/V},\ d_{31} = 0.16\text{pm/V}$ [65,66].

You can also use the SNLO program(ver. 58) provided by Dr. Arlee V. Smith and substitute the wavelengths that you would like to SHG/SFM/THG and click on "Qmix" to find what χ_{eff} is expected for any crystal that is desired by the user.

3.4 Measurement of a Broadband width Pulsed Dye Laser

To measure the bandwidth of a light source in the Ghz range requires using a diffraction grating spectrograph for frequencies in the range of 20-1000 Ghz. For smaller bandwidth frequencies of the order of Ghz to Mhz range more dispersive optics are needed to resolve the spectral structure of the laser , for example a Fabry Perot Interferometer[67] or a Michelson interferometer. Our dye laser has a coherence length of $L_c = \frac{\lambda_c^2}{\Delta\lambda} = 29mm$ and the OPD within the middle of etalon is 3.175mm, so our ability to obtain fringes is satisfied. Our dye laser beam was not split into two beams using a beam splitter and the polarizations of both beams were the same. Lastly the spatially coherence of the beam was not enhanced using, for example, a 5X objective magnification with a 50um pinhole diameter or a 10X with a 25um pinhole, since we desire the need to look at the entire transverse profile of the original beam, as spatial

chirp may also exist in the original dye laser beam. For most of our experiments our PDL uses a single grating cavity, operated at 1st order Littrow angle specifically in the oscillator cavity. With this configuration we measured the bandwidth using a 0.75m diffraction grating spectrograph. As the experiment required finer resolution, using the dye grating at a higher order such as 4th order for the NIR light and 6th order at 486nm, the spectral characteristics were measured using a homemade fixed air space etalon with 1/8" ball bearings. The measured bandwidth of the laser was 100 Ghz wide while operation at 1st order on the grating and 12 Ghz wide when set at 6th order on the dye grating. It is known that operation of the dye laser lower than 8 Ghz can be reached with *only* the oscillator pumped just above lasing threshold. A more technical approach that enables the use of both the pre-amplifier and final amplifier dye cells involves placing a etalon that is broadband in the oscillator cavity. Using a filter or Etalon that is placed within the PDL-1 oscillator cavity and specified for 90% reflectivity, enables a 1.5Ghz bandwidth, and tuning is done by over pressurizing the oscillator chamber with 1-2 atm of Research Grade Nitrogen gas. The resolution for measuring 1.5Ghz output could be made with our homemade etalon which has approximately a 2Ghz resolution.

The dye laser's we used were PDL-1 & 2 made by Quanta Ray/Spectra Physics. Each dye laser was pumped by a Surelite III-10 or I-20 YAG, non seeded, using temperature controlled KD*P crystals that converted the fundamental 1064nm light into third harmonic or second harmonic light. The grating in the dye laser has 600 lines/mm and rotated to 1st order Littrow angle. The output of the dye laser beam is placed in a wedge

and then into a SHG BBO crystal to convert 486nm to 243nm light. The light that is split from the wedge is placed into a SPEX 0.75m spectrometer with the exit slit removed. A CCD camera is positioned near the exit slit with a xyz translational stage aligned to the center of the exit slit and focal position of the Spectrograph. The alignment procedure was as follows, but if a wavemeter is available at the time, these steps are not needed, but recommended for accuracy:

1. Two irises were set at two heights of 9.5” +-1/8” across 0.6m. A 1.5” UVGFS lens was used to focus the light into the 5um sized slit of the spectrometer. The irises were approximately set at 3mm.
2. The lens was removed so that the Hene beam could be centered on the 1.0” tall entrance slit vertically and horizontally and onto the Spherical mirror. The HeNe laser was adjusted until the beam was centered on the center of the 10cm diameter Aluminum Spherical mirror.
3. The beam diameter of the HeNe was enlarged to about 3.0” after traversing through thru the lens, slit, and across the 0.75m breadboard. A 1.5” positive lens was mounted on a xyz stage, and placed 1.5” away from the entrance slit. The lens was then adjusted vertically and horizontally until the circular 3” beam profile was centered across the 4.0” spherical mirror with the slit open all the way.
4. With the exit slit in place the grating was tuned until the Hene light was visible by eye in a semi-dark room with a paper screen. The exit slit was made to be

10um as was the entrance slit. The grating was rotated in only one direction until the HeNe was transmitted thru the exit slit.

5. The exit slit was carefully removed and the CCD camera put in place.
6. The light was attenuated until the beam profile did not saturate the camera and the focus position was adjusted until the image of the entrance slit width of the projected light reached a minimum. The adjustment was made 5 times until the smallest width was identified. The error in adjustment of the focal position is about +-200um for the 0.75m reflecting mirror.
7. The multiple spectral lines from an Argon + Mercury lamp were then identified and recorded at 5-6 different diffracted angles as mentioned in Chapter(xx). This calibration then gives for the grating set at 486nm at 2nd order or 972nm to be 0.00452nm/pixel on the CCD camera. The calibration will be discussed in a later chapter. We can also use the 821 wavemeter measurements to calibrate the spectrograph.

The diffraction grating spectrometer that was used has a grating set at the diffracted angle for 972nm, 28.97 deg. At this angle the wavelength spread over the exit slit of the CCD camera is given by the following expression

$$\frac{d\lambda}{dx} = \frac{d}{mf} cos\beta$$

We find that the spectral width on at the CCD camera is 4.52pm/pixel. A single shot of the dye laser is shown in Fig. 3.9 with background included of the leaking light in the

spectrograph. We fitted the horizontal lineout profile to be Gaussian and the FWHM was 28.4$\pm$0.4 pixels wide. Knowing that the spectral width is 4.52pm/pixel, which is discussed in the next chapter, we obtain (4.52pm/pixel)×30 pixels = 0.1356nm at 972 nm on the Spectrograph dial. The linewidth is then 0.1356/2nd order =0.067nm at 1st order. Using the expression, $df = -cd\lambda/\lambda^2$, with $d\lambda = 0.067nm$ we obtain a bandwidth of 86 Ghz at 486nm. Each pixel represents a resolution of 3 Ghz at 486nm, with the Dye laser operating at 6th order on the grating we measured a value of 17-20 Ghz as the minimum bandwidth observed on the diffraction grating, which translates to 6-8 pixels wide. Given the entrance slit is 10um wide this represents an expected width of 2-3 pixel's width measurement, which does not include the bandwidth of the laser and crosstalk of the pixels. There are a total of 1390 pixels across the CCD camera and at 972 nm translates to a maximum bandwidth measurement of 6.28nm at 972nm or 3.14nm at 486nm. This roughly translates to a bandwidth of 3-4 Thz.

The SHG bandwidth of the laser was measured by using a 2nd set of mirrors aimed thru the same two irises used to measure the bandwidth of the fundamental 486nm light. The bandwidth of the SHG covered the same portion of pixels as the fundamental, so roughly speaking, if the fundamental was 30 pixels wide the SHG was also just under 30 pixels wide. At 6th order of the PDL-1 the SHG linewidth approached 7-9 pixels width as did the fundamental reached 7-8 pixels. The bandwidth measurement was at 243nm must be divided by four instead of two since 243nm light is reflected off of the spectrograph's grating at 4th order. It is known that a thinner BBO

crystal converts more fundamental bandwidth into SHG, for example a 50-100um thick BBO crystal is used in autocorrelators for detecting the time pulse width for femtosecond lasers, which usually are 25fs to 100fs long, or 20nm to 8 nm in bandwidth. For smaller bandwidth we had to use a fixed spaced Etalon to measured the bandwidth of the laser.

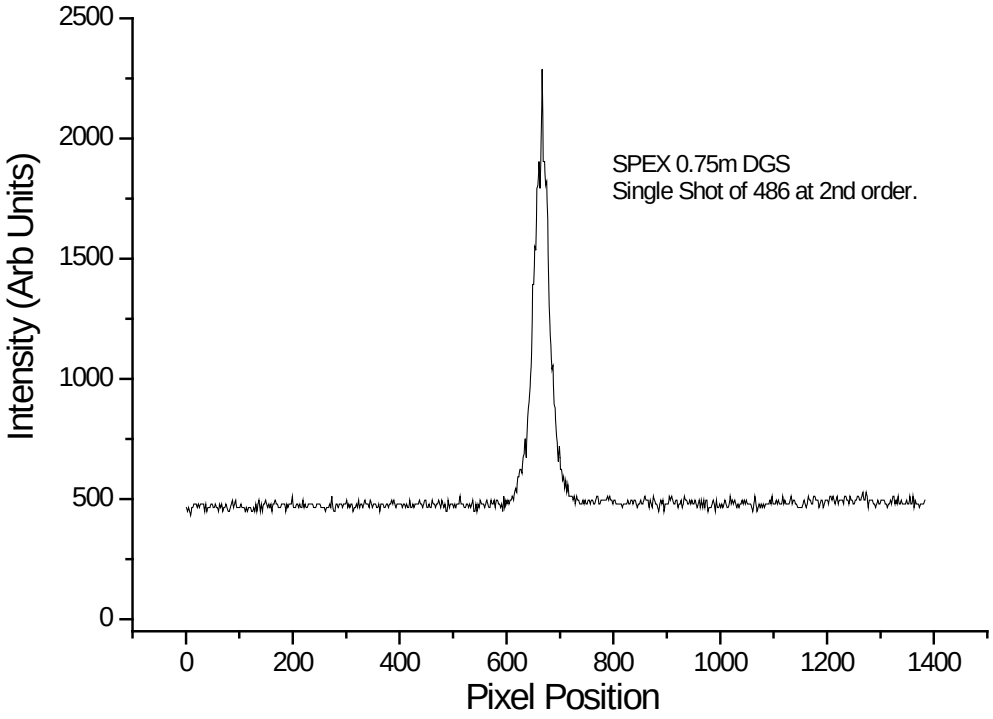

Fig. 3.9 Single shot measurement of the bandwidth of the dye laser, at 2nd order on the dye grating measured on a SPEX 0.75 diffraction grating spectometer converted into a spectrograph.

Bandwidth Measurement using a Fixed Air Space Etalon:

The etalon that we used had a surface flatness, after coating, of $\lambda/10$ at 633nm. It is known that using a higher reflectivity produces a higher resolving etalon.

We chose for our etalon a 90% reflection +- 2 percent with a wedge of 30 arcminutes. The reflectivity finesses is 28 with a surface finesse of 10 and wedge finesse of 40. This results in a total finesse of 10, which tells us that the total Finesse is determined by the factor that has the least Finesse, our surface flatness. The spacers used wereball bearings with a 0.125" spacing gives a free spectral range of 47Ghz. Without these spacers it is very difficult to produce a set of perfectly circular set of rings. The resolution is defined as FSR/Finesse which results in a 4.7Ghz resolvability. The optics chosen were two CVI PR1-488/515 – 90 –IF -1537 –C. The FSR is 47 Ghz with a typical FWHM of 8Ghz for the bandwidth of the dye laser. Given that the input beam is collimated the lens produces the same optical path length for the rays that are collectively constructing and deconstructing within the middle portion of the etalon upon each reflection and transmission. The k-vector's are the most collimated within the middle of the etalon, and using a single focusing lense the object is positioned at infinity, i.e. the middle of the etalon, and the lense projects the accumulated phases of each reflection and transmission and produces a interferometric image onto the CCD camera that is circular due to the curvature of the spherical surfaces of the lense. The expression that gives the bright fringe pattern between two surfaces with a spacing d is

$$2ndcos\theta = m\lambda$$

Using the small angle approximation, we simplfy the expression above, , using $\theta = \frac{r_m}{f}$ to give:

$$\frac{2nd}{\lambda}\left(1-\left(\frac{\theta^2}{2}\right)\right)=m$$

Substitution of the angles gives us.

$$\frac{2nd}{\lambda}\left(1-\left(\frac{r_m^2}{2f^2}\right)\right)=m$$

Solving for r_m we get

$$1-\left(\frac{\lambda m}{2nd}\right)=\frac{r_m^2}{2f^2}$$

$$r_m^2=2f^2[1-\left(\frac{\lambda m}{2nd}\right)]$$

Subtracting adjacent rings we obtain

$$r_{m+1}^2=2f^2[1-\left(\frac{\lambda(m+1)}{2nd}\right)]$$

$$r_m^2-r_{m+1}^2=2f^2\left[1-\left(\frac{\lambda m}{2nd}\right)\right]-2f^2\left[1-\left(\frac{\lambda(m+1)}{2nd}\right)\right]=\frac{\lambda f^2}{nd}\quad \text{Eq.(1)}$$

Using the same expression $r_m^2=2f^2[1-\left(\frac{\lambda m}{2nd}\right)]$ and assume $r_{m'}^2=2f^2[1-\left(\frac{(\lambda+\delta\lambda)m}{2nd}\right)]$ which assumes that if the wavelength has a bandwidth it only changes the radius on the same order m.

$$r_m^2-r_{m'}^2=2f^2\left[1-\left(\frac{\lambda m}{2nd}\right)\right]-2f^2[1-\left(\frac{(\lambda+\delta\lambda)m}{2nd}\right)]=\frac{\delta\lambda f^2 m}{nd}\quad \text{Eq.(2)}$$

Dividing equation Eq(2) by Eq(1) we get the following expression:

$$\frac{r_m^2-r_{m'}^2}{r_m^2-r_{m+1}^2}=\frac{\frac{\delta\lambda f^2 m}{nd}}{\frac{\lambda f^2}{nd}}=\frac{\delta\lambda m}{\lambda}$$

Since $2ndcos\theta = m\lambda$ and for small angles the expression becomes$2nd = m\lambda$, solving for m, $\frac{2nd}{\lambda} = m$

$$\frac{r_m^2 - r_{m'}^2}{r_m^2 - r_{m+1}^2} = \frac{\delta\lambda\ 2nd}{\lambda^2}$$

Since $df = cd\lambda/\lambda^2$ and the $FSR = \Delta f = c/2nd$ then the equation above reduces to

$$\frac{df}{c} = \frac{\Delta f}{c}\frac{r_m^2 - r_{m'}^2}{r_m^2 - r_{m+1}^2}$$

Redefining in terms of the wavenumber we get the final expression[68].

$$\delta\nu = -\frac{1}{2nd}\frac{r_m^2 - r'^2_m}{r_m^2 - r_{m+1}^2}$$

We find a bandwidth of 8Ghz where r_{m+1} is the radius of the smaller diameter fringe and $r_m, r_m^{'}$ is the FWHM of the radius of the adjacent ring. The n is the index of refraction of air and d is the length of the spacer. The dye laser was then tuned to 1st order to broaden the bandwidth of the laser. We used a 2.5:1 telescoping lense setup with a focusing lense to produce a set of parallel k-vector's in the etalon and a focusing lense to relay the image of the interferometric rings onto the CCD camera as shown in Fig. 3.10.

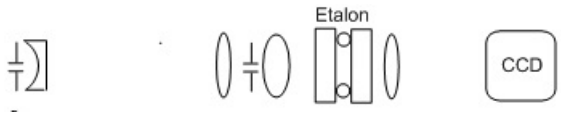

Fig. 3.10 Optical Setup for measuring the Fabry Perot Rings from a Fixed Air Spaced Etalon.

The dye output was first aligned to the CCD camera with all the optics removed. The CCD image of the beam was centered on the front of the CCD camera. Two irises were placed separated by 10”. The dye output was directed toward a telescope of 1:2.5 and then focused within the etalon. A lens with a 6.0” focal length was then directed to the CCD camera. The CCD camera was mounted on a X-Y translation stage. All four optics were centered on each piece by looking at the beam profile on the CCD camera and then adjusting the vertical and horizontal position of the lens until it was centered on the CCD camera.

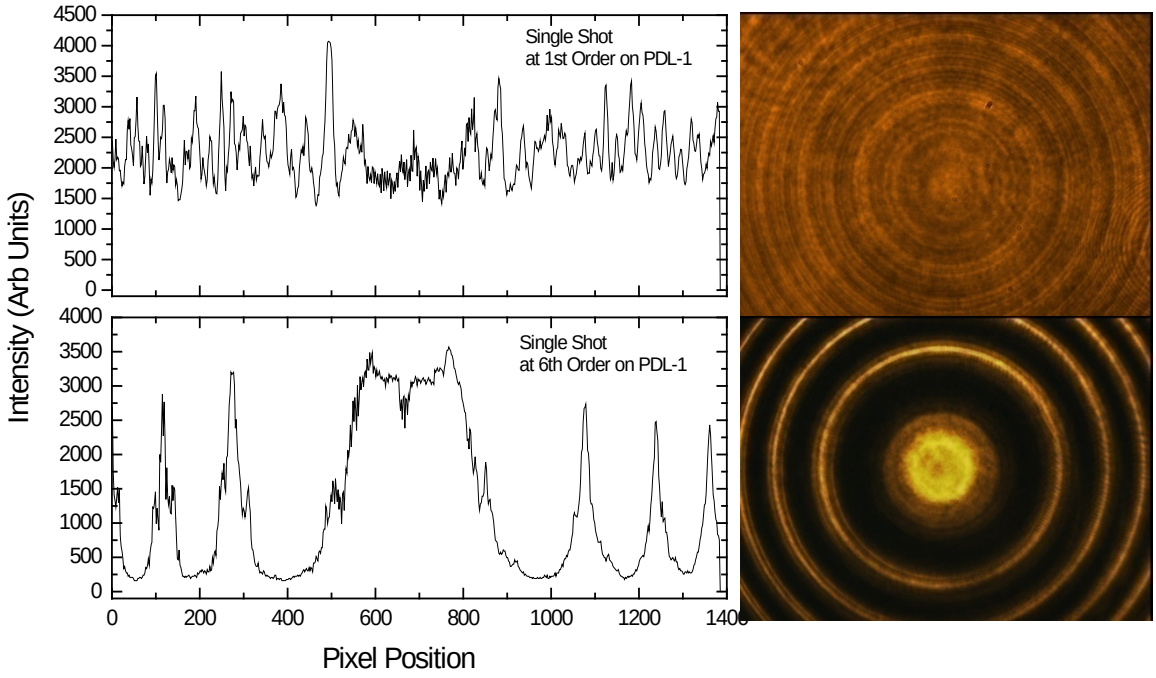

Fig. 3.11 Single shot bandwidth measurement using a Fixed Spaced Fabry Perot Etalon with a FSR of 47Ghz with dye laser having ~100Ghz (top set) and ~10Ghz(bottom set). The figure on the left shows the lineout taken center of the fringe pattern and the right a single shot capture of a single pulse.

From the Fig. 3.11 above we have used 1/8” ball bearings to fix the spacing between the two optics at a value of 3.175mm, which corresponds to an FSR of 47 Ghz. The Dye laser was then tuned to 1st order on the grating. The bandwidth has exceeded the FSR and as a result we are not able to define the bandwidth of the dye laser.

We then purchased 1mm ball bearings and had the initial problem of picking a material to hold all three ball bearings within the etalon. Instead of using a double sheeted corrugated paper to hold the 3.175mm ball bearings within a triangular formation, we used a 3”x5” card with three small holes punched at three equidistant angles. The 1mm ball bearings were placed by hand into the circular aperture within each of the three punched holes. The paper aperture with the ball bearings were then placed on a wire tripod configured with three arms. This tripod is needed tolower the ball bearings and the paper aperture onto the optic.

A single shot bandwidth measurement using the 150Ghz fabry perot is show below inFig. 3.12.

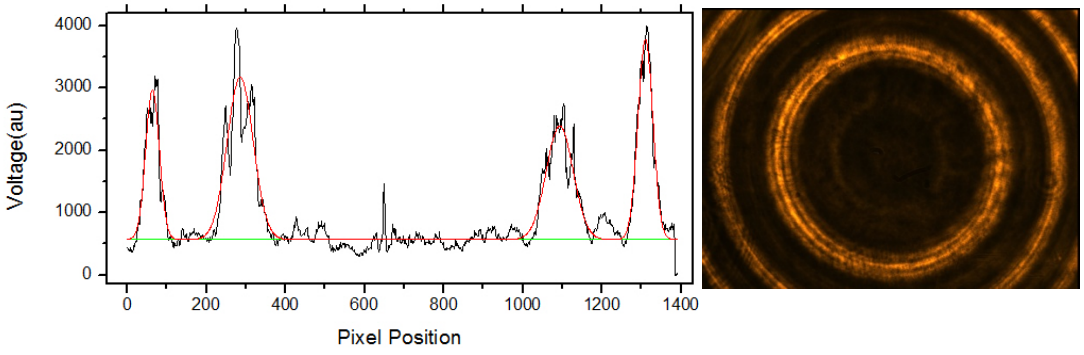

Fig. 3.12 Single shot measurement of the PDL at 2nd order on the dye grating, using a 150Ghz fixed spaced etalon.

In conjunction with this measurement the bandwidth was also measured on the 0.75m spectrometer. The plot in Fig. 3.13 on the left shows a 10 shot averaged measurement of the 100Ghz wide laser. The averaged spectral profile is fitted using two Gaussian plots. A second fit shows evidence of a stronger bandwidth lasing within the broader bandwidth of the entire dye laser spectrum. The measured value of the inner bandwidth is approximately 36Ghz. This agrees with the measured bandwidth using the 150Ghz wide etalon which was roughly ~30 Ghz. Since the spectrometer shows evidence that the bandwidth is quite large, ~ 190Ghz, we expected the entire CCD camera to be filled with many rings. This large bandwidth is evident in the background of the single shot ring profile as the baseline is non-zero and also observed in real time from shot to shot. Another important point is since the spacing between rings must correspond to 45Ghz, one can get a rough estimate of the linewidth by scaling the width of the ring to the spacing between adjacent rings to measure the linewidth without the formula.

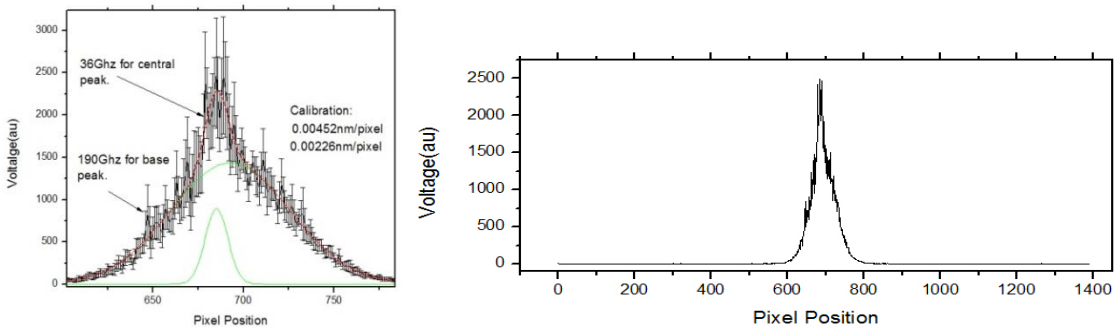

Fig. 3.13Ten single shot measurements of the PDL configured for 2nd order on the grating for lasing. The figure on the left is a plot of the average taken over 10 shots. The figure on the right shows the entire lineout of the spectral profile.

In conclusion we were able to measure the bandwidth of the PDL-1 dye laser when operating the dye laser at 1st to 6th order littrow on the grating. This demonstrates

the possibility of expanding the bandwidth of the laser by operating at a different order on the grating. No extra alignment of the laser cavity was needed when switching between different orders on the grating and we did not need to add additional optics such as a prism to expand the bandwidth of the dye laser. The ability to expand the spectral bandwidth involved only the rotation of the grating to different orders m. In addition one can also illuminate a lower number of lines within the grating by introducing a square aperture to block the number of illuminated lines on the grating. But the bandwidth suffers from sporadic gain narrowing within the 300Ghz bandwidth from shot to shot when reducing the number of lines illuminated on the grating. The "fingers" of high gain across the bandwidth are uneven, which results in longer data measurements to decrease the random error observed for Ps excitation with 300Ghz broadband laser.

Small Angle Approximation for Cos pheta

In the small angle approximation we used in the expression $2ndcos\theta = m\lambda$ we arrived at the following expression

$$\frac{2nd}{\lambda}\left(1-\left(\frac{\theta^2}{2}\right)\right) = m$$

Solving for the angle we get:

$$\left(1-\left(\frac{\theta^2}{2}\right)\right) = \frac{m\lambda}{2nd}$$

$$\left(1-\left(\frac{m\lambda}{2nd}\right)\right)=\frac{\theta^2}{2}$$

$$\theta=\sqrt{2-\left(\frac{m\lambda}{nd}\right)}$$

We compare to the true formula

$$\theta=\cos^{-1}\left(\frac{m\lambda}{2nd}\right) \quad (1)$$

In these two expression for θ, we see that in order for the angles to be small the order,m , needs to be near 13000 with an upper limit of 13069 and anything larger would have no solution, assuming that d=3.175mm, $\lambda = 486nm$, and n=1.00027. We conclude that θ is a very accurate expression if using eq(1) to map the position of the mth order straight fringe pattern that is imaged from the fixed spaced etalon. Another important aspect to observe is why the center of the ring pattern has a central maximum spot. This spot can be explained by the following reason. The pattern that is observed is similar to a circular diffraction pattern in which the phases of the wavelengths constructively interfere at near zero deg incidence. By tuning the wavelength the bright spot is converted into a dark spot in the middle of the fringe pattern because of destructive interference that exists between adjacent maximum orders. In deriving the expression$\delta\nu = -\frac{1}{2nd}\frac{r_m^2-r'^2_m}{r_m^2-r_{m+1}^2}$ we notice that there is no angular dependence of the radius's of the ring's which is false. In the table (xx), we calculate the radius of each order using the expression, $=\frac{r_m}{f}$, from eq(xx) in the etalon image given

the focal length of the lense, 58.5cm. Notice in the 5th column the numerical values of the spacing between adjacent radius's is not linear. Hence, for an accurate measurement of the bandwidth one would then need to analytically compensate the nonlinear behavior at near zero degrees, as bandwidth measurements we observed were showing a 15% difference in the measured bandwidth when analyzing between different pairs of imaged rings. Upon further exploration we find that it is constant by looking at inverse of the squared difference's between adjacent rings, the expression shows there is no angular dependence. More study is needed to establish the sublte errors in measuring the bandwidth of a broadband laser using a fixed spaced etalon.

Order	Radians	Focal Length(m)	Radius(mm)	$r_{m+1} - r_m$	$\frac{1}{r_{m+1}^2 - r_m^2}$
13069	0.00753892	0.0585	0.441027	NA	NA
13068	0.01448683	0.0585	0.84748	0.406453	1.909428
13067	0.01905007	0.0585	1.114429	0.266949	1.909379
13066	0.02271444	0.0585	1.328795	0.214366	1.909331
13065	0.02586485	0.0585	1.513094	0.184299	1.909282
13064	0.02867122	0.0585	1.677267	0.164173	1.909233
13063	0.03122646	0.0585	1.826748	0.149481	1.909185

Table 3.2 Radius's of each order of the etalon ring used in the etalon. The 4th column is the difference of the radius's between adjacent orders. The 5th column is the inverse of the differences of the radius's squared.

The resulting nonlinear behavior cannot be applied in our bandwidth analysis due to the non- one to one correspondence between eq(1) and eq(xx) when calculated the order and the radius. The radius values do match with the measured values using eq(1). But this analysis has helped explained the large circular maximum that appears in the center

of the pattern, and in addition has explained why the bandwidth that we do calculate is not the same for different sets of rings. But there is an advantage to using$\delta\nu = -\frac{1}{2nd}\frac{r_m^2 - r'^2_m}{r_m^2 - r_{m+1}^2}$, since the angle and order is not needed in the calculation. Another aspect of the analysis we must look at is the error involved in the small angle approximation. Specifically what is considered to be a "small" angle is the next question we would like to answer.

We calculate the approximation to see what limit works and from the Fig. 3.14 below we plot the relative error between $Cos\theta$ and $1 - \theta^2/2$. We set the limit for relative error to be <0.1%, as shown in Fig. (xx), for measuring the bandwidth, accurately. This implies the angles must be less than 22.5deg or 0.39 radians. Given a 6" lense or 0.15m focal length lense the largest r_m is 58.5mm, or 5.85cm. Using an input angle of 22.5 deg is beyond the dimension of our UNIQ camera , which has 6.5mm x 4.9mm CCD area.

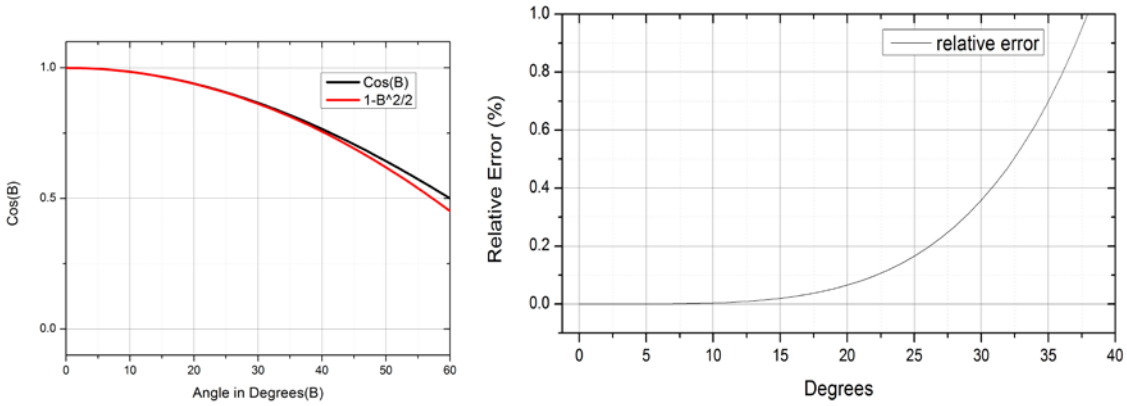

Fig. 3.14 Plot of the $Cos\theta$ and $1 - \theta^2/2$ versus the incidence angle. Note the two different functions are very similar for angles less than ~30deg. The plot on the right hand side is the relative error of the small angle approximation versus the angles used.

We generate a table of values to observe the relative error in using the small angle approximation, a shown in Table 3.3.

Angle (degrees's)	Angle(radians)	$Cos\theta$	$1-(\theta^2/2)$	Relative Error(%)
0	0	1	1	0
1	0.017453	0.999848	0.999848	3.86687E-07
2	0.034907	0.999391	0.999391	6.18964E-06
3	0.05236	0.998630	0.998629	3.13573E-05
4	0.069813	0.997564	0.997563	9.92035E-05
5	0.087266	0.996195	0.996192	0.000242507
6	0.10472	0.994522	0.994517	0.000503651

Table 3.3 Tabulated comparison of errorsusing the small angle approximation for angles less than 6 degrees.

Based upon measurements we made earlier of our 8Ghz bandwidth laser we see that the largest radius measured is 3.3mm. Using $x = fd\theta$, then our largest angle would be ~3.25 deg=0.056 radians. We have an estimate of the error produced from using the large angle approximation for our setup and the value is 0.000031 %. Hence our uncertainty is 0.000001 or 1 part per million. This establishes the large angle error is small in applying the relationship of$\delta\nu = -\frac{1}{2nd}\frac{r_m^2 - r'^2_m}{r_m^2 - r_{m+1}^2}$.

For r_{m+1} order corresponds to smaller radiuses, we find that if we take the measured difference of adjacent radius components the nonlinear behavior of the radiuses mentioned in Table (3.2) is nearly one to one for all orders. The uncertainty though is 1 part in 10^5 in combination with the uncertainty of the radius measurement which is $\pm$2 pixels with another $\pm$1 pixel off center position of the circular fringe which gives a total uncertainty of $\pm$3 pixels. For the numerator we have an uncertainty of

difference and the power's which is $4 \times (\pm 3 pixels) \times 4.65um$=0.00006m. The denominator has the same value of uncertainty be we must add the aforementioned 1 part in 10^5 resulting from the table(3.2). The last two components are the indices of refraction and the spacing of the ball bearings. We have an uncertainty of 2 parts 10^3 for the diameter of the ball bearings and 4 parts in 10^6, which occurs since the index of refraction for air may change with temperature. Going back to the equations 1 and 2 we have the defined wavelength, distance separation, and the index of refraction. The uncertainty for the products and quotients is given as

$$\frac{\delta q}{|q|} \approx \sqrt{\left(\frac{\delta w}{|w|}\right)^2 + \left(\frac{\delta x}{|x|}\right)^2 + \left(\frac{\delta y}{|y|}\right)^2 + \left(\frac{\delta z}{|z|}\right)^2}$$

$$\frac{\delta q}{|q|} \approx \sqrt{(0.00006)^2 + (0.00007)^2 + (0.002)^2 + (0.000004)^2}$$

The δq= 0.1Ghz , or 100Mhz in our bandwidth measurement. Please note that we still measured a different bandwidth of 9.5Ghz using a set of rings further away from the center as opposed to 8Ghz where we a set of rings closer to the center, and we do not know where the error is coming from. More than likely if an order greater than the 5th order ring away from center of the etalon fringe pattern is used, than a closer accurate measurement of the bandwidth can be reached. We verified the FSR of the etalon using the 821 wavemeter by is tuning 45 Ghz at 486nm. We measured a value of 45 ± 3 Ghz using a 821 wavemeter. Taking the ratio's of the spatial spread of the width of a single ring and the difference in radius's of adjacent rings we can the bandwidth of the dye laser.

It is also known that the laser linewidth can be measured using a Fizeau wavemeter[69] by looking at the contrast of the sinusoidal fringe pattern. But this may require a large number of optics including a air wedged gap a off axis paraboloid mirror, microscope objective with spatial filter, a compensating plate, and cylindrical lense with a CCD camera, and a knowledge of a proper alignment to achieve a zero shear position at the location of the CCD camera. This solution may work but it is also possible just to observe the reflection from 5min arc wedge at 45 degrees imaged onto a CCD camera.

Calibration of the 0.75m Grating Spectrometer in Czerny Turner Geometry

The SPEX 0.75m grating spectrometer was converted into a Spectrograph, by removal of the exit slit, and calibrated with a Mercury Argon Spectral lamp. Calibrating the Spectrograph allowed us to measure the spread of frequencies emitted from the dye laser, as alternatively rotating manually the mechanical knob that rotates the diffraction grating and transmits the unknown input light thru the exit slit, and recording the intensity vs the dial number. The dial number is calibrated with two reference line's with the knob slowly rotated with two hands along one direction, multiple times, to avoid hysteresis. But recording the intensity and measuring the triangular intensity profile, with the diffraction limited aperture of the grating combined with the diffraction limited size of the entrance slit, vs the dial number can also be used as a comparison with the measurements made with the spectrograph. It was found that pairs of lines can

be imaged onto the CCD camera with a 6.5-6.3mm width across the CCD camera width in a 750mm focal length spectrometer. By using a known spectral reference line from a high voltage discharge lamp, it is possible to record wavelengths quickly. Also using a CCD camera allowed single shot measurements of the bandwidth across the spatial profile of the dye laser beam. The ability to measure the bandwidth in real time enables quick adjustments with a large bandwidth laser. In the later sections I will mention the calibration lines used for the SPEX spectrograph.

The first set of wavelength measurements were done with the spectrometer and rotating the dial by hand with both hands and using a EOT-2030 Pin Photodiode(PD) placed at the exit slit and measuring the transmitted intensity at the exit slit. The two optical beams were collinearly aligned to one another over a distance of 0.75m with two irises. The HeNe laser beam, which is the known wavelength, was sent along with a portion of the unknown wavelength of the dye laser input . The EOT PD detector responds to a CW photon source that is on order of uW, produces a voltage output that was observed on the digital oscilloscope. The slope of the dial number was measured using the 3rd harmonic of 354nm light or 1064.1nm with the Nitrogen laser that emitted 337.1nm. The wavelengths correspond to 1064.1nm and 1011.3nm. These two wavelengths were chosen since they were well known and in close vicinity to one another. The closeness of the two reference lines reduces the systematic error that creeps up due to gear slippage if long rotations of the dial are involved to reach the two reference lines. Also the ability to measure accurately more than once is reduced in time

so multiple measurements can be made. The wavelength difference is $52.80 \pm 0.07nm$ with a dial number difference of 104.955 ± 0.345 with a dial resolution of 0.005 measured 21 times. The standard error is 104.955 ± 0.075. The slope is defined as nm/dial number, which is 0.503nm/dial number with a standard deviation of 0.001nm/dial number. For the first stage wavelength measurements we used the 0.503nm/dial number slope with the He-Ne 632.816nm line or 1265.632nm in air. The next set of measurements involved the Spectral Lamp and calibration of the wavelength across the CCD camera since the gear slippage was occurring more frequently. This required a measurement of the spectral width across the CCD camera.

The SPEX 0.75m Grating spectrometer consisted of a plane reflecting grating with a blaze angle of 36.5 Deg, dimensions of 108mm x 108mm x 16mm with no wavelength specification, which is assumed to be broadband. The grating is similar to the model 53-*-530R at Richardson Gratings. The spectrometer is mounted on a breadboard with two 10cm Aluminum Spherical mirrors and two mechanical slits with the grating arranged in a Czerny Turner geometry. The CCD camera used was a UNIQ 12bit 4.65um size pixel camera with an EPIX framegrabber board mounted on Aluminum Machined Square block with 1.0" xyz Translation stage. The reference lamp used was a HG-1 Mercury & Argon pencil lamp from Ocean Optics. The lamp output was transferred thru a 600um solarized fiber that was one foot long. The 600um size fiber was used to couple the most light out from the 100uW lamp, and we used a UV collimating lense to transfer the light output and still enable good alignment overlap of

the Mercury & Argon lamp with the dye laser across the two irises separated 0.6m apart. All sources entered the input of the spectrograph using a 4.0cm positive lense, which was mounted on a xyz stage, with the entrance slit set at 10um.

Using the Spectral reference lines and strength of emission lines quoted in the publications I measured the spectral spread of the grating spectrometer using 6 reference points. Six points were used as six references were found at the time to consist of more than two reference lines simultaneously across the 6.3mm CCD camera over the 750mm focal length of the spectrometer. The spectral spread vs the diffraction angle of the spectrometer will be mentioned later in this chapter.

We next used a High Voltage Discharge Spectral lamp with Hydrogen. The Hydrogen line that we used is the 486.133nm H-beta line in air overlapped with the dye laser input. The H-beta line is well known but the wavelength per pixel across the CCD surface is not known. I optimized the position of the CCD camera that was mounted on a xyz stage with 1.5Ghz wide HeNe laser source to position the camera at the focus of the 2^{nd} spherical mirror of the spectrometer. This can be positioned by looking at the slit image of the He-Ne laser and varying the z-position until the slit was straight vertically and sharp in feature, which can be determined by looking at the “horizontal lineout “ using the EPIX software and minimizing the spatial width of the imaged entrance slit. We used a HG-1 Ocean Optics Argon & Mercury pencil lamp. In Fig. 3.15 shows the lines that we used to calibrate the nm/Pixel over the 500-1200nm range of the spectrograph.

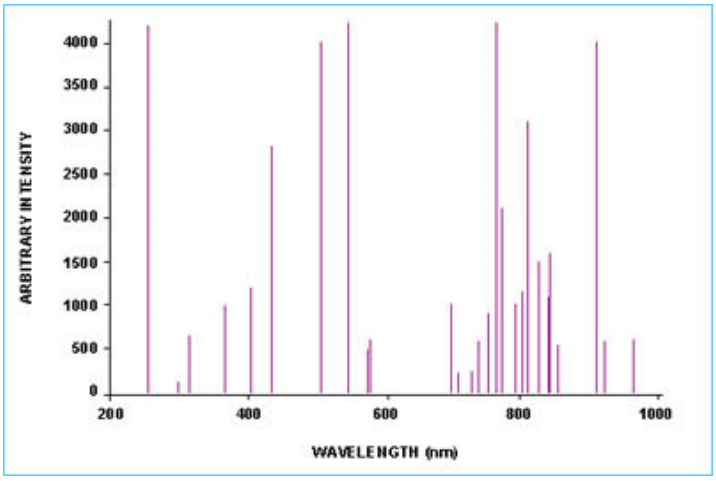

Fig. 3.15 HG-1 Mercury Argon Calibration Source from Ocean Optics. Emission Spectrum from Mercury emission lines are <600 nm. Argon emission lines are >600 nm.

We measured a total of six sets of lines that were found by rotating the dial of the spectrometer at various wavelengths and rotating the grating to the lines that provided the largest intensity. To compensate for the amount of power emitted from a Pencil lamp powered by a 9V battery, we had to turn off the room lights, look for any light leaking into the spectrometer, and used a long electronic shutter time for the CCD camera. For our first set of spectral lines we measured were 365.0158nm, 365.4842nm, and the 546.0750nm lines[70,71,72] with the grating in the spectrometer set for ~1095nm, as shown in the Table below.

Wavelength(nm)(Air)	**365.0158**	**365.4842**	**546.0750**
Order	3	3	2
Wavelength in 1st order	1095.0474	1096.4526	1092.1500

Table 3.4 1st set of Mercury Reference Lines

$$\lambda_{air} = \lambda_{vac}/n$$

Since the temperature around the time of calibration was roughly 80 deg +-2 deg we must convert the wavelengths to the proper values since the reference air wavelengths were done at standard laboratory settings of roughly 73+-2 deg. Using the expression$\lambda_{air} = \lambda_{vac}/n$, we take the wavelengths from the reference multiply by the index of refraction at 73 deg F and then divide by the index at 80 deg F to get the proper wavelength for our measurements, which are shown in the table below:

Wavelength(nm)	**365.4842**	**365.0158**	**546.0750**
Order	3	3	2
Wavelength in 1st order	1096.4526	1095.0474	1092.1500
Index at 80 deg	1.000273114	1.000273141 at 80	1.000266356
Index at 73 deg	1.000276837	1.000276864 at 73	1.000269996
Wavelength(nm) @ 80d	365.485549	365.0171585	546.076998
Wavelength in 1st order	1096.4566	1095.0515	1092.1540

Table 3.5 1stset of Mercury Reference lines with the indices of refraction of air compensated for the larger temperature change.

An image of all three reference lines taken is shown in Fig. 3.16.

Fig. 3.16 Spectral Reference lines imaged using a CCD camera for the 1st set.

The spacing between the two outer reference lines, 1096.4566nm and 1092.1540nm, is 1010.67 pixels. The spectral spacing is 4.257 pm/pixel. A second set of lines are the Argon lines 840.8210nm and 842.4648nm[73], which are listed in Table 3.6 with the adjusted indices of refraction.

Wavelength(nm)	**840.8210nm**	**842.4648nm**
Order	1	1
Wavelength in 1st order	840.8210nm	842.4648nm
Index at 73 deg	1.00026707	1.00026706
Index at 80 deg	1.00026346	1.00026345
Wavelength(nm) @ 80d	840.8240	842.4678
Wavelength in 1st order	840.8240	842.4678

Table 3.6 2nd set of Mercury & Argon reference lines with the indices of refraction of air compensated for the larger temperature change.

From the 2nd Table the spacing was 346.70 pixels. The wavelength spread across the CCD camera is 4.741 pm/pixel for wavelengths around 841nm sent to the spectrometer. A image of all two reference lines taken is shown in Fig. 3.17 for the 2nd set of lines.

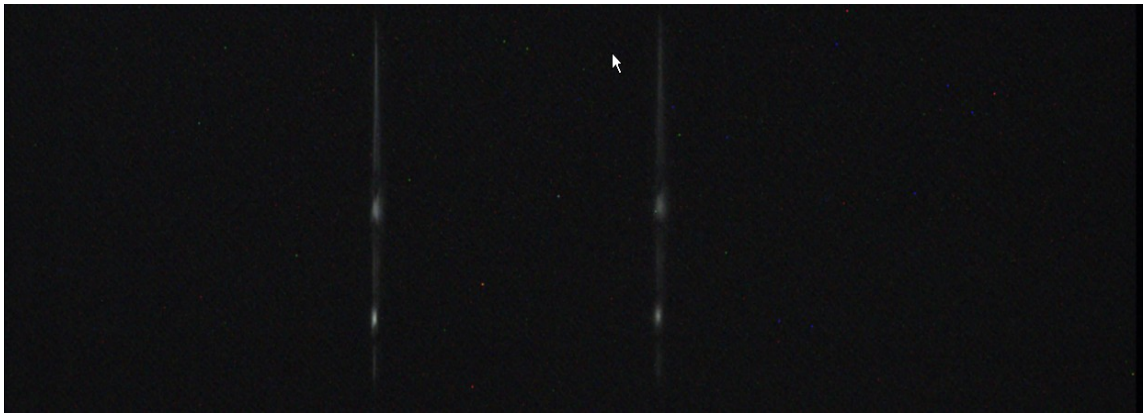

Fig. 3.17 Spectral Reference lines imaged using a CCD camera for the 2nd set.

We next look at the 3rd set of lines which are shown in Table 3.7[73].

Wavelength(nm)	750.3869nm	751.4652nm
Order	1	1
Wavelength in 1st order	750.3869nm	751.4652nm
Index at 73 deg	1.00026762	1.00026761
Index at 80 deg	1.00026401	1.00026400
Wavelength(nm) @ 80d	750.3896	751.4679
Wavelength in 1st order	750.3896	751.4679

Table 3.7 3rd set of Mercury & Argon reference lines with the indices of refraction of air compensated for the larger temperature change.

From this table the difference of 1.0783nm is spread across 222.0 pixels which gives 4.857 pm /pix for the 751nm setting. The total wavelength's difference uncertainty is 0.001nm. The uncertainty of the pixel spacing between adjacent lines is 0.1um. Since $q = x/u$, where x=1.0783nm and u=222 pixels × 4.65um we can find the uncertainty of the nm/ pixel spacing from the following expression:

$$\delta q = q\sqrt{\left(\frac{\delta x}{x}\right)^2 + \left(\frac{\delta u}{u}\right)^2}$$

Our uncertainty in x is 0.001nm and uncertainty in u is 0.1um. With q=1.04456e-6 nm/m then δq =0.00103. Or $q = 1.044 \pm 0.001 \times 10^{-6}$ nm/m. A image of the 3rd reference lines is shown in Fig. 3.18.

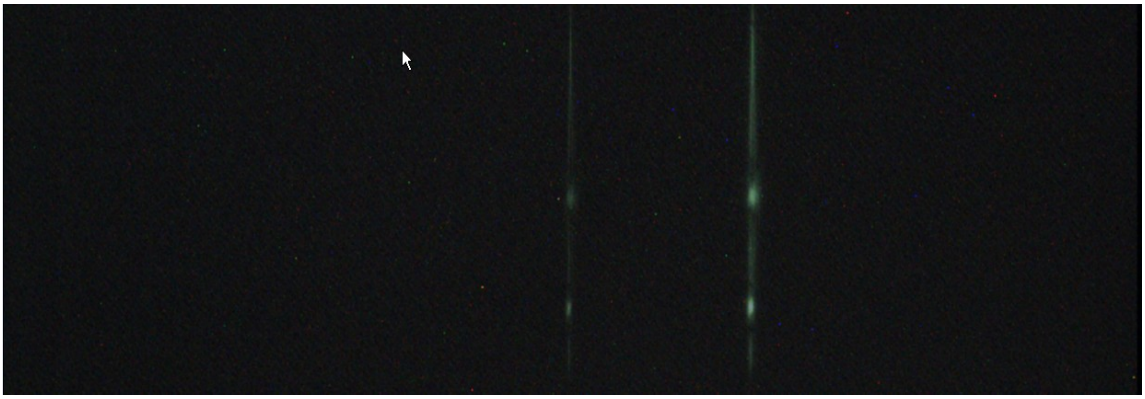

Fig. 3.18 Image of 3rd set of spectral reference lines.

Our 4th set of lines are shown in the Table 3.8[70,71,72,73] with the indices of refraction adjusted to the proper temperature.

Wavelength(nm)	**811.5311nm**	**810.3693nm**	**404.6565nm**
Order	1	1	2
Wavelength in 1st order	811.5311	810.3693	809.3130
Index at 73 deg	1.00026723	1.00026723	1.00027458
Index at 80 deg	1.00026362	1.00026363	1.00027089
Wavelength(nm) @ 80d	811.5340	810.3722	404.6580
Wavelength in 1st order	811.5340	810.3722	809.3160

Table 3.8 4th set of Mercury & Argon reference lines with the indices of refraction of air compensated for the larger temperature change.

From the 4th Table the spacing was 464.00 pixels. The wavelength spread across the CCD camera is 4.780 pm/pixel for wavelengths around 810nm sent to the spectrometer.

A image of all three reference lines taken is shown in Fig. 3.19 for the 4th set of lines.

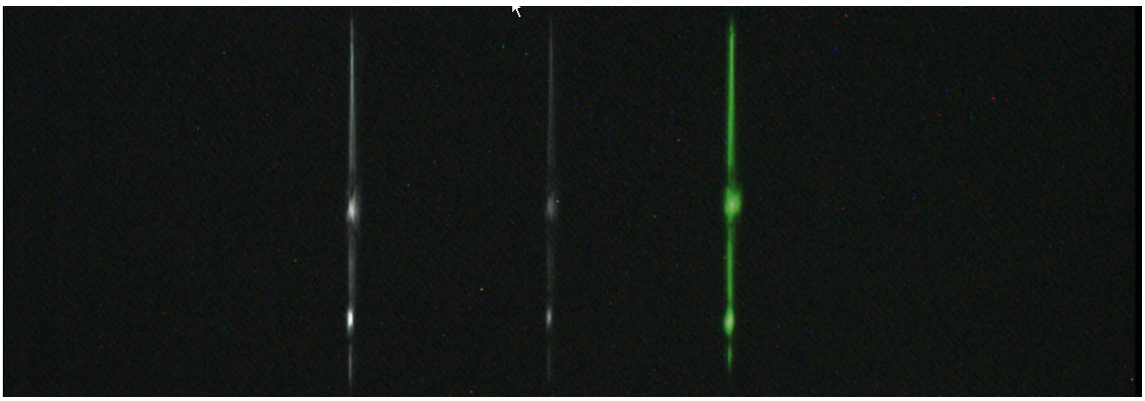

Fig. 3.19 Image of 4th set of spectral reference lines.

The table of the 5th set of compensated temperature reference lines are shown in Table 3.9[70,71,72].

Wavelength(nm)	576.9610nm	579.0670nm
Order	2	2
Wavelength in 1st order	1153.9220	1158.1340
Index at 73 deg	1.00026954	1.00026950
Index at 80 deg	1.00026590	1.00026587
Wavelength(nm) @ 80d	576.9631	579.0691
Wavelength in 1st order	1153.9262	1158.1382

Table 3.9 5th set of Mercury & Argon reference lines with the indices of refraction of air compensated for the larger temperature change.

From the 5th Table the spacing was 1025.17 pixels. The wavelength spread across the CCD camera is 4.1086 pm/pixel for wavelengths around 1156nm sent to the spectrometer. A image of all two reference lines taken is shown in Fig. 3.20 for the 5th set of lines.

Fig. 3.20 Image of 5th set of spectral reference lines.

Our final set of lines are the 576.9610nm and 579.0670nm again, but set at the 1st order on the diffraction grating spectrograph. The table of adjusted values is shown below.

Wavelength(nm)	576.9610nm	579.0670nm
Order	1	1
Wavelength in 1st order	576.9610	579.0670
Index at 73 deg	1.00026954	1.00026950
Index at 80 deg	1.00026590	1.00026587
Wavelength(nm) @ 80d	576.9631	579.0691
Wavelength in 1st order	576.9631	579.0691

Table 3.10 6th set of Mercury & Argon reference lines with the indices of refraction of air compensated for the larger temperature change.

From the 6th Table the spacing was 418.00 pixels. The wavelength spread across the CCD camera is 5.038 pm/pixel for wavelengths around 577nm sent to the spectrometer. A image of all two reference lines taken is shown in Fig. 3.21 for the 6th set of lines. Notice the spacing is not exactly ½ of the previous set of lines, 5th table. This indicates a Cosine diffracted angle dependence of the wavelength spacing which we will derive next. A image of all two reference lines taken is shown in Fig. 3.21 for the 6th set of lines.

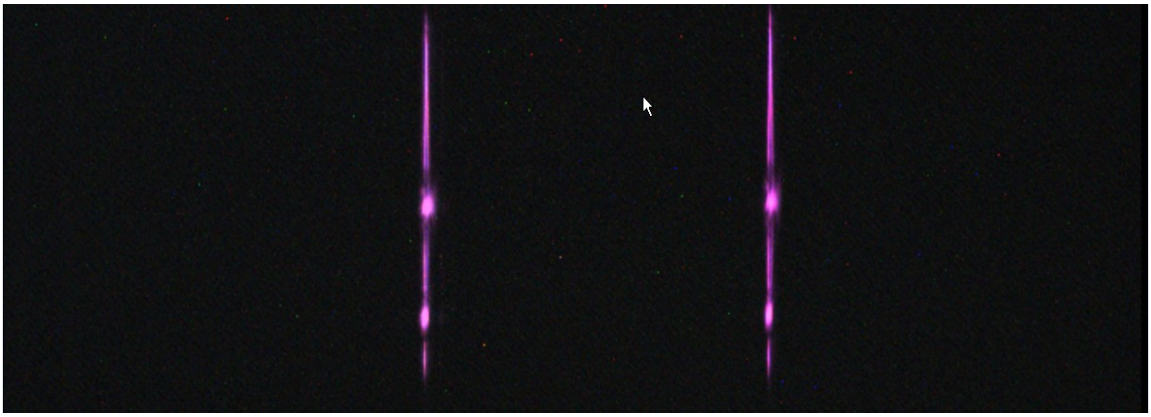

Fig. 3.21 Image of 6th set of spectral reference lines.

The diffraction equation is:

$$d(sin\alpha \pm sin\beta) = m\lambda$$

The incident angle, α, is considered a constant since all wavelengths incident onto the grating are the same and solving for the diffracted angle β, we find changes with wavelength dependence of the diffracted angle. Taking the derivative of both sides of the diffraction equation with respect to the diffracted angle and wavelength we get the following expression. Notice the spread of the diffracted wavelength has a Cosine dependence.

$$\frac{d\beta}{d\lambda} = \frac{m}{dcos\beta}$$

Using the two following equations, where the first expression is the same as before, the second equation is the spread of the arc length given the width of the angle over the focal length of the spectrograph, we have:

$$dcos\beta d\beta = md\lambda$$

$$dx = fd\beta$$

where dx is the spatial spread at the exit slit, f is the focal length of the spectrometer, and d is the groove spacing of the grating, we divide both of them and get

$$\frac{d\lambda}{dx} = \frac{d}{mf} cos\beta$$

The calibration of the wavelength difference over the spatial spread at the exit slit is dependent on the diffraction angle used in the SPEX 0.75m spectrometer, and the focal length of the spectrometer. The grating spacing is 1200 lines/mm and the order is one with a focal length of presumably 0.75m we get a slope value of 1.111×10^{-6}. The last

unknown parameter is the diffracted angle with initial offset angle which we find next. Another possible unknown value is also the focal length of the spectrometer.

The photo below in Fig. 3.22 will show us how the diffracted grating angle was obtained. In the Fig. 3.22 we see how the sine bar drive operates for the SPEX 0.75 grating spectrometer. The important portion is the isosceles shaped triangle that is shown in the lower left hand portion of Fig. 3.22. The triangle has a base which is a 50tpi screw that helps rotate the grating. When the grating is rotated to emit a wavelength that corresponds to zero nm, the triangle looks like a "T" with the brass block positioned towards the upper limit end of the 50tpi screw, the upper limit end of the screw would be located on the left handside of Fig. 3.22 positioned vertically in the middle.

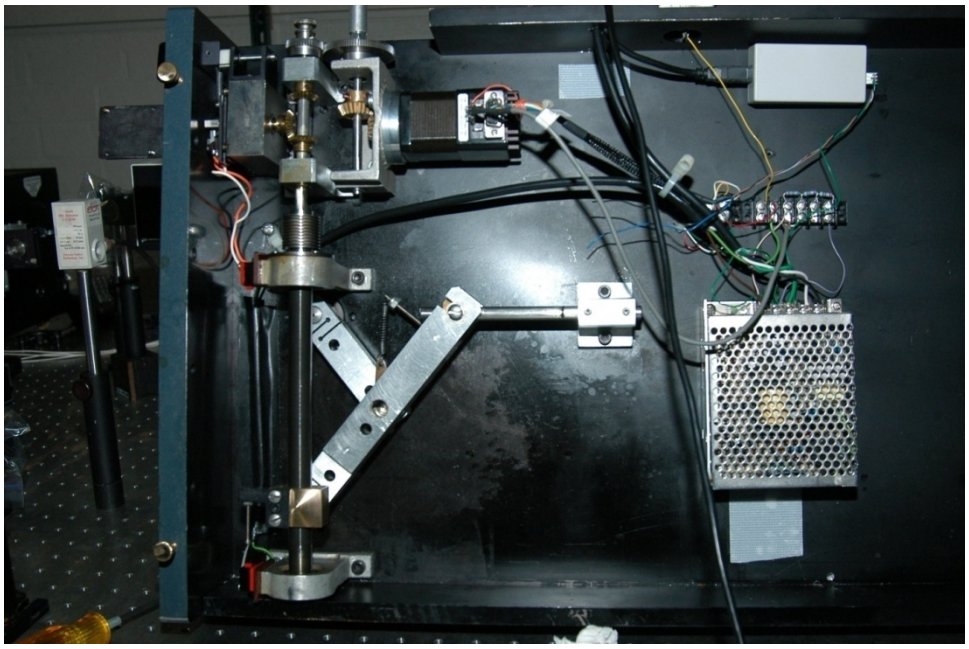

Fig. 3.22 A photo is taken of the SPEX 0.75m grating spectrometer, underneath the breadboard.

With a vernier dial caliper with a resolution of 0.001” on the dial we measured the arm to be 3.267 ± 0.003" in length measured from the center of the brass block(located on the lower left of the photo) and the pivot point of the isosceles triangle, which is the vertex of the triangle. One revolution on the crank, rotates the 50tpi screw one revolution if the gears are one to one, produced a 0.02” translation across the threaded screw. The rotated angle of the grating can be found by taking half of 0.02” and dividing by the length of the arm, and finding the inverse sine. The grating spectrometer is arranged in a Czerny Turner geometery so when the grating is set for zero nm, i.e. the grating face is parallel to the left wall of the spectrometer, this will angularly set the grating for zeroth order reflection for the diffracted angle. As a result, all wavelengths will exit the spectrometer and the incident angle corresponds to an initial offset angle. I measured the initial offset angle to be -6.72 degrees. The diffracted angle value can be found using the diffraction equation since the rotated angle is related to the wavelength, and the initial offset angle must be added to all diffracted angles as the grating is rotated. With a good understanding of the relationship between the rotated angle, diffracted angle, and incident angle in a Czerny Turner Geometry we will next produce a table to get an expression for the diffracted angle vs the wavelength. We use for our slope 0.503nm/dial number. A table of the values of all parameters is in Table 3.11.

Turns on Large Crank	X(inch)	Arm Length (inch)	Rotated Angle	Initial Angle	nm	Diffract Angle	Diffract Angle + Offset	Cos(Diffract Angle + Offset)
0	0	3.267	0.000	6.719	0.000	-0.117	-6.719	
0.5	0.01	3.267	0.175	6.895	5.031	-0.114	-6.546	
1	0.02	3.267	0.351	7.070	10.062	-0.111	-6.373	
1.5	0.03	3.267	0.526	7.245	15.092	-0.108	-6.200	
2	0.04	3.267	0.702	7.421	20.123	-0.105	-6.028	
2.5	0.05	3.267	0.877	7.596	25.154	-0.102	-5.855	
3	0.06	3.267	1.052	7.771	30.185	-0.099	-5.682	
3.5	0.07	3.267	1.228	7.947	35.216	-0.096	-5.509	
4	0.08	3.267	1.403	8.122	40.247	-0.093	-5.336	
4.5	0.09	3.267	1.579	8.298	45.277	-0.090	-5.163	
5	0.1	3.267	1.754	8.473	50.308	-0.087	-4.990	
5.5	0.11	3.267	1.930	8.649	55.339	-0.084	-4.817	
6	0.12	3.267	2.105	8.824	60.370	-0.081	-4.644	
6.5	0.13	3.267	2.281	9.000	65.401	-0.078	-4.471	
..	..	..	..	..	..	..	..	..
87.5	1.75	3.267	32.389	39.108	880.393	0.426	25.194	0.9049
88	1.76	3.267	32.597	39.316	885.424	0.429	25.399	0.9033
88.5	1.77	3.267	32.805	39.524	890.455	0.432	25.604	0.9018
89	1.78	3.267	33.014	39.733	895.486	0.435	25.809	0.9003
89.5	1.79	3.267	33.223	39.942	900.517	0.439	26.015	0.8987
90	1.8	3.267	33.433	40.152	905.547	0.442	26.221	0.8971
90.5	1.81	3.267	33.644	40.363	910.578	0.445	26.428	0.8955
91	1.82	3.267	33.855	40.574	915.609	0.448	26.635	0.8939
91.5	1.83	3.267	34.066	40.785	920.640	0.452	26.843	0.8922
92	1.84	3.267	34.278	40.997	925.671	0.455	27.051	0.8906
92.5	1.85	3.267	34.490	41.210	930.701	0.458	27.260	0.8889
93	1.86	3.267	34.703	41.423	935.732	0.461	27.469	0.8873
93.5	1.87	3.267	34.917	41.636	940.763	0.465	27.679	0.8856
94	1.88	3.267	35.131	41.850	945.794	0.468	27.889	0.8839
94.5	1.89	3.267	35.346	42.065	950.825	0.471	28.100	0.8821
95	1.9	3.267	35.561	42.280	955.856	0.474	28.312	0.8804
95.5	1.91	3.267	35.777	42.496	960.886	0.478	28.524	0.8786
96	1.92	3.267	35.994	42.713	965.917	0.481	28.736	0.8768
96.5	1.93	3.267	36.211	42.930	970.948	0.484	28.949	0.8750
97	1.94	3.267	36.428	43.148	975.979	0.487	29.163	0.8732
97.5	1.95	3.267	36.647	43.366	981.010	0.491	29.377	0.8714
98	1.96	3.267	36.866	43.585	986.040	0.494	29.592	0.8696
98.5	1.97	3.267	37.085	43.804	991.071	0.497	29.808	0.8677
99	1.98	3.267	37.305	44.024	996.102	0.500	30.024	0.8658
99.5	1.99	3.267	37.526	44.245	1001.133	0.504	30.240	0.8639

Table 3.11 Tabulated values of the Diffracted Angle values and corresponding wavelengths for the SPEX 0.75 Diffraction Grating Spectrometer.

I used a 6th order polynomial fit to find the relationship of the input angle to the diffracted angle, this is plotted in the Fig. 3.23 below.

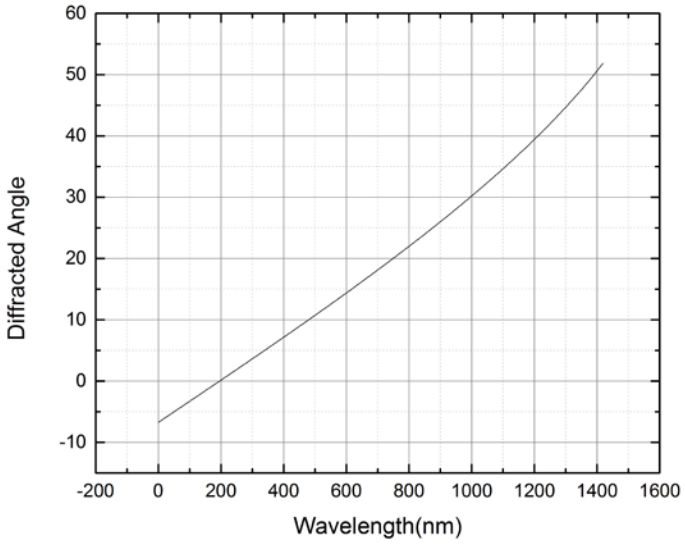

Fig. 3.23 Plot of the Diffracted Angle vs. Wavelength for the SPEX 0.75m

Using a 6th order polynomial fit, $y = y_o + B_1x + B_2x^2 + B_3x^3 + B_4x^4 + B_5x^5 + B_6x^6$, the values are $y_o = -6.7100$, $B_1 = 0.0340$,$B_2 = 3.1005 \times 10^{-6}$, $B_3 = -8.5380 \times 10^{-9}$, $B_4 = 1.7207 \times 10^{-11}$, $B_5 = -1.2936 \times 10^{-14}$, and $B_6 = 4.0510 \times 10^{-18}$. A high order was chose to get closer to the extrapolated diffracted angle to within 0.01 deg.

After measurement of the reference lines I next found the pixel corresponding to the exit slit using a He-Ne laser and the same two input irises. A right angle L shaped base mount was placed and clamped next to the base of the xyz stage for the CCD camera. This was needed to help aid in placing the CCD camera back into its original position when the exit slit was removed and reinstalled. The pixel position

corresponding to the exit slit is pixel 641. Then using the recorded images of the Mercury and Argon lines for the six measurements we can extrapolate the wavelength value for the pixel position 641 and work backwards to get the diffracted angle for each correspond wavelength, which shown in the Table 3.12 below.

Wavelength	**dλ/dx**	**dλ/dx (pm/pixel)**	**Wavelength(at exit slit)**	**Diffracted Angle**
577nm	1.083e-6	5.038	578.4271	13.60
751nm	1.045e-6	4.857	751.7032	20.11
810nm	1.028e-6	4.780	810.5031	22.40
841nm	1.020e-6	4.741	841.5701	23.62
1094nm	0.916e-6	4.257	1095.1346	34.40
1156nm	0.884e-6	4.109	1156.7000	37.33

Table 3.12 Accumulated reference wavelength values from Table's 3.5-3.10 with the corresponding diffracted angle at the exit slit.

With the diffracted angles well known, using the 6th order polynomial fit, we plot the $d\lambda/dx$ vs the $Cos\beta$ of the diffracted angle, as shown in Fig. 3.24, and find a slope value of 1.12667×10^{-6} with a 1.4% error with respect to the predicted value. The adjusted Reduced Chi square value is 0.99988 which indicates a good fit. We measured the focal length of the Spherical mirror and found it was 74.4cm with a resolution of 0.1cm(~1/32"). In calculating the error again with respect to the new predicted value we now had an 0.6% error.

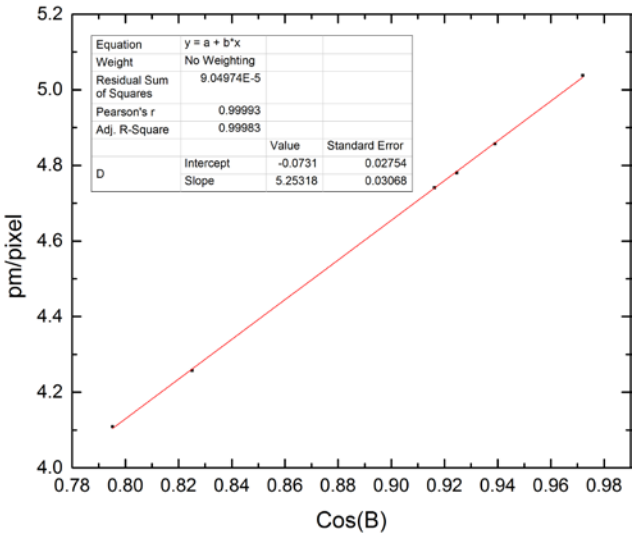

Fig. 3.24 Plot of the measured wavelength spatial spread versus the cosine of the diffracted angle.

To avoid an extra set of calculations Figure 3.25 shows the mapping of the wavelength input with the diffracted angle and the resulting wavelength spatial values without the Cosine dependence.

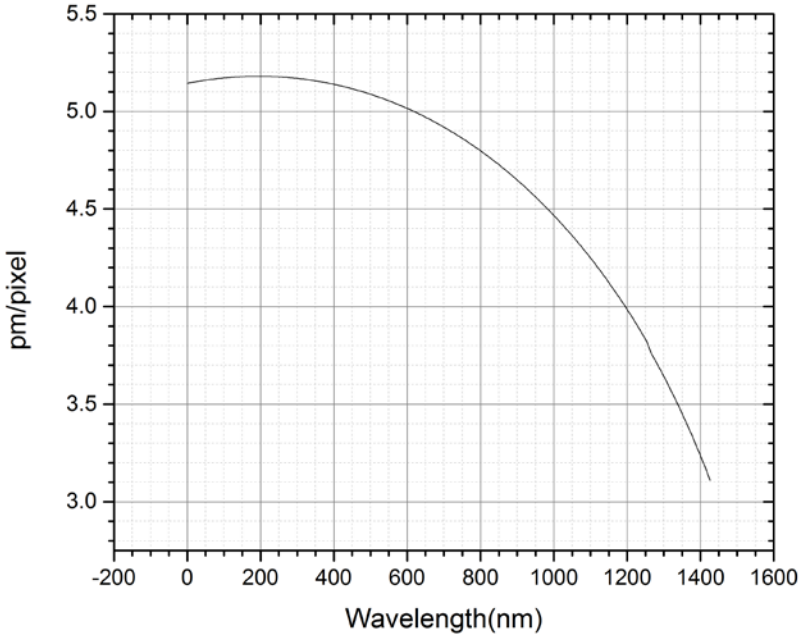

Fig. 3.25 Final result of pm/pixel vs wavelength input in spectrograph.

The Balmer H-Beta line is at 486.133nm in air and at second order in the spectrograph is also existing as a 972.266 nm source. Using the 6th order polynomial and combination with the fitted straight line of the spectral wavelength spread or quickly using the graph in Fig. (xx) we get a value of 4.52pm/pixel. We next would like to look at possible systematic error's in our measurements.

If the angle is incorrect which is possible if the grating mount and the rotational latching mount crept over time, that will produce a systematic offset of $\pm 1\ deg$. This would result in a spacing of 4.47 pm/pixel or 4.57 pm/pixel as oppose to the 4.52pm/pix. The difference of 0.05pm/pixel would correspond to 63Mhz/pix. The total width across the CCD camera is 1391 pixels. If the reference spectral lamp is centered than the largest spacing would be typically 600 pixels. Each pixel would have an error of 63Mhz/pixel and with a 600 pixel spacing result in a 38 Ghz error offset for wavelengths furthest from the reference. We use the conversion, 12.7 Ghz =0.01nm at 486nm. But with the grating operating at 2nd order the wavelength's error reduces by ½ which results in a possible error of $\pm 0.015nm$, and by chosing the reference line to be close to the tuning range on the order of +-100 pixels reduces the error to $\pm 0.003nm$.

We tested the calibration's drift, by looking at the spacing between the 365.4842 and 365.0158nm lines measured in Table (xx) which are the 1st set of reference lines. We tested by checking the spacing in January of 2010, which corresponded to 330 pixels apart. One month later in February we measured 330 pixels. A 7th set of reference lines were found much later, as shown in Fig. 3.26 These sets of lines correspond to 2 x

365.0158nm and the 727.2936nm line[70,71,72,73].

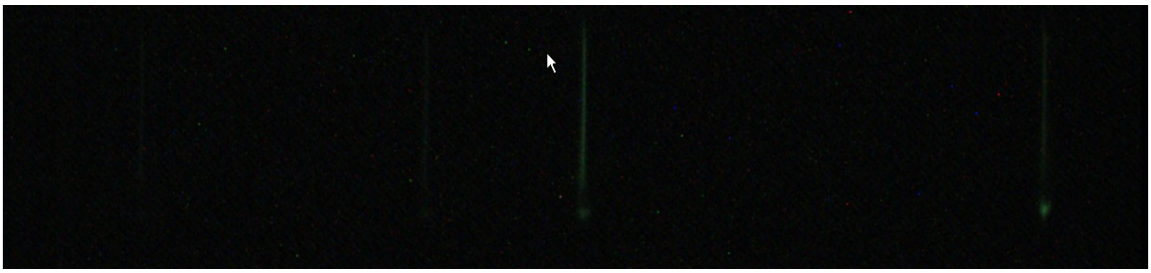

Fig. 3.26 7th set of spectral lines imaged from a Mercury & Argon pencil lamp.

The spacing between the lines was 560 pixels, this corresponds to 4.889 pm/pixel. The wavelength at this setting is 730.0316nm at the exit slit which corresponds to 19.28 deg for the diffracted angle and that gives a calibration of 4.886 pm/pix. The error between the two is 0.06% in which 4.889 pm/pixel is assumed to be the expected value. The measurement at 730nm is a good test of the calibration since it does not involve the previous six sets of reference lines used for the calibration.

We also observed the spacing when another heat source was turned on within the laser enclosure. The alexandrite laser, which represents a significant heat load, was turned on for more than 30 minutes. The reference lines that correspond to the 7th set of reference lines drifted 5-6 pixels to the left of the CCD camera. But the spacing of the two lines did not change which indicates the preservation of the wavelength spread over the horizontal width of the camera. One last check was observed with a 821 wavemeter four years later. The dye laser was tuned in between 731.802nm and 731.716nm with a spacing of 18 pixels. This would give a value of 4.778 pm/pixel. Using the previous lookup table I get a value of 4.883pm/ pixel. A large error of 2.2% was

found and we believe this would indicate an error in the offset angle of the grating spectrometer, since the same two irises used before in the previous calibration were no longer installed, and also the procedure for carefully positioning the CCD camera at the exit slit which should correspond to the He-Ne laser inputted thru the same two irises, was not done, so the accuracy of the diffracted angle could be offset. Also the measurement should have been done with a larger spread in between the two tuning points used in the measurement with the 821 wavemeter.

A quick solution to finding the calibrated wavelength spread on the CCD camera installed on the Spectrograph is to use the PDL-1 dial at 6^{th} or 5^{th} order. Using the dial number and tuning the laser across the CCD camera that is mounted onto the Spectrograph will enable one to obtain the wavelength spatial calibration much more quickly, as the accuracy is not important, whereas the linear dial number on the PDL-1 tuning wavelength is probably very accurate. For example if tuned to the first point, 2900 corresponds to 483.333 nm and tuning across to the 2^{nd} point, 2930 corresponds to 488.333nm, a wavelength difference of 5.000nm, with the measured pixel spacing will give the experimenter a good calibration value, along with a required reference input. The resolution is 0.01 on the PDL-1 Dial. This corresponds to a tuning step of 0.002nm at 6^{th} order on the PDL tuning grating.

In the later times in 2010 I also mounted the spectral Hydrogen or Helium lamp on a micro translational stage as the peak intensity was offset from the alignment with respect to the two irises and the entrance slit set a <10um. The wavelength is

determined by the following expression, using the Hydrogen Balmer Beta Line in air[74]:

$$\lambda_{dye} = \left[2 \times 486.133nm(air) \pm \left(\frac{4.52pm}{pixel}\right)(\, spacing(\, 486.133\, line - DyeLaser))\right]/2$$

This will provide approximately a 0.01 nm accuracy value at a rate of 7mHz or faster.

As the data rate increased we reverted to using the 821 Bristol wavemeter as it was unpractical to measure the wavelengths at a slow rate. Our conclusion is that using these methods offers the experimenter to quickly tune the wavelength without an expensive wavemeter and also observe wide bandwidth outputs in the Ghz range, with the resolution of 17Ghz, with single shot capabilities.

3.6 Quadrant Photodetector

Integration of pulsed laser beam positioning with commercial motorized mirror mounts requires interfacing with the Labview software with quadetectors tailored for short ns pulse detection. The sampling rate for the PCI-6024 data acquisition board is 250kS/s. This enables the data acquisition to resolve us events, but as a result of small time resolution a ns laser pulse is undetectable. With the DAQ board one would need to modify the quad detectors in order sample and hold the existing voltage for the DAQ board to measured.

We can find the current flow of the quad photodetector by treating the PD as a single Norton equivalent circuit junction produced by a p-n junction. The simplified version of the PD is a Norton current source in parallel with a capacitor and a resistor. The current will split in two at the RC junction, one current flowing thru the capacitor(I_C) and the other flowing thru the resistor (I_R). The total current is thus

$$I = I_C + I_R$$

Since the voltage is the same across each component we get

$$I_R R = I_C Z_C \quad \text{and} \quad Z_C = \frac{1}{j\omega C}$$

We now solve for I and we get

$$I = I_R + I_R R/Z_C$$

The voltage output will then be

$$V = IR = (I_R + I_R \frac{R}{Z_C})R_L$$

In terms of the complex impedance we get the voltage output to be

$$V = \frac{IR}{\sqrt{1 + \omega^2 C^2 R^2}}$$

Notice that the voltage output from the Quad PD will drop to $1/\sqrt{2}$ of its intitial value. This occurs when $\omega = 1/RC$, this represents the frequency response of the Quad PD. Having a larger capacitance reduces the frequency response of the PD. As a result the time constant is extended, which makes a ns pulse event last longer than its true pulse duration. But in the case for beam positioning we need the event to last longer than ns.

There was no commercial system that was available to my knowledge for 243nm nanosecond laser 10Hz or 1Hz pulse detection and for NIR light. The following stretching or sample and hold circuit component, in Fig. 3.27 was used which allows the user to stretch the measured pulsed voltage on a DAQ connected to a computer[75].

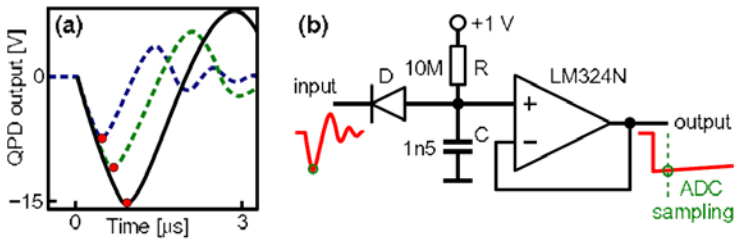

Fig. 3.27 Figure adapted from [75]. This is a sample and hold circuit design used for pulsed laser events.

The following circuit was fabricated so as the typical 5ns pulse width could be stretched to register a voltage amplitude on the computer using the DAC as a voltage measurement. A quad detector and wired the internal components to take the photocurrent and stretch the pulse and in addition add and subtract [76] with a given gain of 1000 for both UV 243nm light and visible-IR light. The resistors that are used 1% tolerance 1kohm resistor's. A quad detector uses summation of the two upper quadrants and takes the difference of upper and lower sections combined. The uncertainty is defined as the upper=dx1+dx2 minus the lower =dx3+dx4,etc. Since the provisional uncertainty is a summation of all uncertainties using a 1% tolerance resistor reduces the uncertainty of the beam's position by a factor of 10 compared to a tolerance of 10% and this is helpful for approaching the near center of the quadrant

region as voltage differences start to approach the under tolerance values. Using a 30AWG wire(0.010” diameter) and the wire warp tool allowed the fabrication of the pulse stretched quad detector to be on a very small scale, and contained within one electrical box. The laser pulse signal was fed in the connector block and the connector block is connected to the PCI-6024. The common PCI-6000 series has many useful features such as 16 channel analog voltage measurements and two TTL digital output clocks , 2-3 external triggering channels, which can enable a computer to become a digital oscilloscope. The Surelite TTL Snych output pulse triggered the PCI -6024.
One could also purchase from Pacific Silicon Sensor Incoprorated the entire quadetector which includes a Quad Sum and Difference Amplifier, for ~$400-500. This specific quad detector cannot be modified for pulse detection and may not have the pulse width to be detectable on a 1us resolution DAC board. The window from Pacific Silicon Sensor Incorporated can be replaced with a UV Grade Fused Silica window from CVI by placing the quad detector in between the vice and slight cracking the original window on the head. But the leads that are attached to the Quad Si wafer are very fragile and can be broken off if no window is in place. This enabled the computer to measure single shot locations of the laser pulse that is tracked into the 821 wavemeter or allow a +-1mm location of the beam onto the target chamber with respect to the +-500um Positron beam size on to the target. But using the floor as the non moving component there is the slight possibility of moved for each platform, assuming the optical table is non floating, for the beam to move. The addition of punched 3x5 cards that are attached to

the back and front ends of the viewport, with quad detectors allowed for a general tracking of the laser beam position with respect to the target in the UHV chamber.

References

[53] P.P. Sorokin, J.R. Lankard," Stimilated Emission Observed from an Organic Dye Chloro-aluminium Phtalocyanine", IBM J. Res. Dev. 10,162 (1966)

[54] F.P. Shafer et.al. " Organic Dye Solution Laser", Applied Physics Letters, 9(8), 206(1966)

[55] B.H. Soffer , B.B. McFarland, "Continuously Tunable, Narrow-Band Organic Dye Lasers", Applied Physics Letters, Vol 10.,No 10, May 15 1967

[56] S.A. Meyers, " An Improved Line Narrowing Technique for a Dye Laser Excited by a Nitrogen Laser," Opt. Comm. 4, 187 (1971).

[57] T.W. Hansch "Repetitively Pulsed Tunable Dye Laser for High Resolution Spectroscopy", Applied Optics, Vol 11 No. 4, April 1972

[58] Hellma USA, SPIE San Diego Optics & Photonics Show August 2014, Personal Communication.

[59]P. Drell, S. Chu," A Megawatt Dye Laser Oscillator-Amplifier System for High Resolution Spectroscopy", Optics Communications Vol 28, No 3 March 1979, pg 343-348

[60] W. Koechner, Solid State Laser Engineering, 6th Rev, Springer c2006, pg 120.

[61] Quanta Ray / Spectra Physics, PDL-1,2,3 Manual.

[62] Handbook of Nonlinear Optical Crystals 3rd Edi. V.G. Dmitriev, G.G. Gurzadyan, D.N. Nikogosyan

[63]D. Eimerl, L. Davis, S. Velsko, E.K. Graham, A. Zalkin, J. Appl. Phys, 62, 1968-1983(1987)

[64]K. Kato: IEEE J. QE QE-22, pg1013-1014 (1986)

[65]Eckardt, R.C. et al. IEEE Journal of Quantum Electronics 26,p. 922 (1990)

[66]Weber, M.J., Handbook of Optical Materials, CRC, Boca Raton, Pg. 148. (2003)

[67]PAR MM. CH. FABRY ET A. PEROT,"Theorie ET Applications D'UNE NOUVELLE METHODE DE SPECTROSCOPIE INTERFERENTIELLE" ANNALES DE CHIMIE ET DE PHYSIQUE 16,115 (1899)

[68] Extended JHS “Fabry Perot Etalon, a guide to its use on the Optics course” Extended JHS Jan 1996, Dept. of Physics, Univeristy of Oxford.

[69] “ Laser-linewidth measurement with a Fizeau wavemeter” Christoper Reiser, Peter Esherick, Robertt B Lopert, Optics Letters, Nov 1988, Vol 13 No11 981-983.

[70] Joseph Reader, Craig Sansonetti, J. Mervin Bridges “ Irrradiances of Spectral Lines in Mercury Pencil Lamps”. Applied Optics Vol 35. No 1. , Jan 1, 1996.

[71] Craig J. Sansonetti, Marc. L. Salit, Joseph Reader. “ Wavelengths of Spectral Lines in Mercury Pencil Lamps”. , Applied Optics, Vol 35. No.1, Jan 1 1996.

[72] E.B. Saloman, “Wavelengths, Energy Level Classifications, and Energy Levels for the Spectrum of Neutral Mercury”, Journal Physical Chemistry, Ref. Data. Vol. 35, No 4, 2006.

[73] G. Norlen, Phys. Scr. 8, 249 (1973).

[74]Ralchenko,Yu, Kramida, A.E. Reader, J. and NIST ASD Team (2008), NIST Atomic Spectra Database (Ver. 3.1.4). http://physics.nist.gov/asd3[2008, March 26], National Institute of Standards and Technology, Gaithersburg, MD.

[75] Kral. L.” Automatic Beam Alignment system for a pulse infrared laser” Rev. Sci. Instru. 80, 013102 (2009)

[76]Anderson. M., Ward, C “ All-Reflective Automated Beam Alignment Device for Ultrafast Lasers” American Journal of Physics, 72(10) Oct. 2004, pg 1347-1350

Chapter 4
Experiments

SSPALS laser induced signal

The positron pulse implanted onto the target surface generates a significant amount of vacuum Ps atoms. The conversion efficiency of o-Ps atoms formation is ~35-40% for the porous silica target. These o-Ps atoms annihilate into a burst of gamma rays which are observed using single-shot positron annihilation lifetime spectroscopy(SSPALS) [77]. The lead tungstate scinntillator used is 50mm in diameter and 40mm in length. The scinntillator was combined with a Hamamatsu R2083 PMT where the center of the scinntillator was about 75mm away from the target. The annihilation signal was sent to a 6 Ghz bandwidth digital oscilloscope set to a sampling rate of 20Ghz. The signal or voltage pulse is proportional to dN/dt or the number of annihilation gamma rays detected within the decaying gamma ray burst. Shown in Fig. 4.1 is the optical setup just outside of the viewport which shows the mirror's, irises, and other optics needed to direct and maintain overlap of the 243nm UV beam and the Residual 532nm beam with respect to the porous silica target used during the experiments.

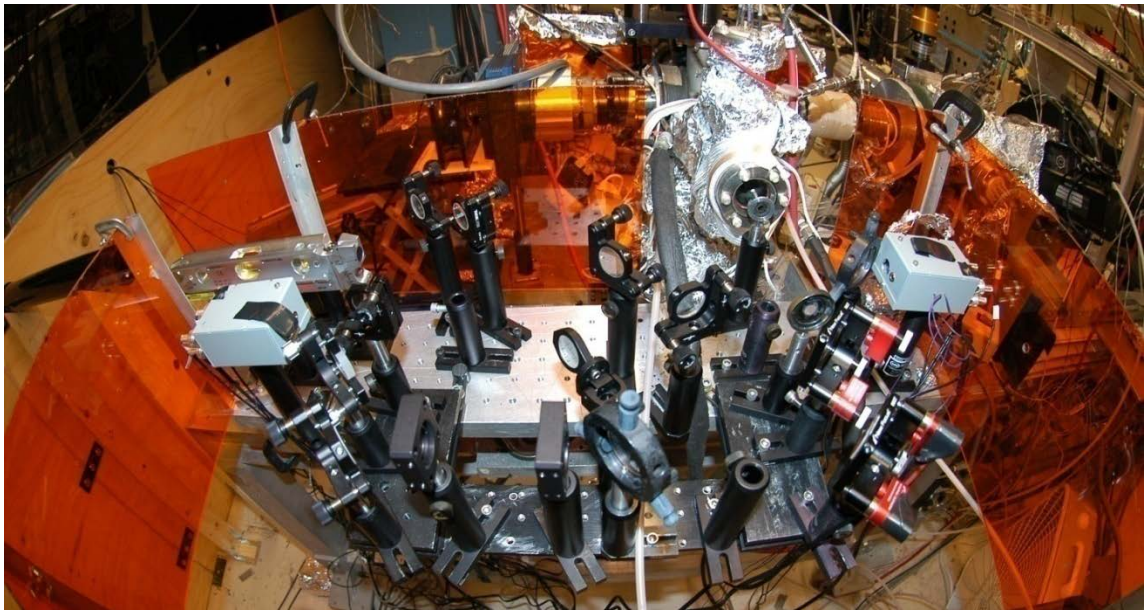

Fig. 4.1 Optical Setup just outside of the Viewport.

A photo of the porous material target is shown in Fig. 4.2 on the left side, which was removed after the experiment. In same Fig. 4.2 the photo on the right is showing the target holder and the target chamber just outside of the viewport .

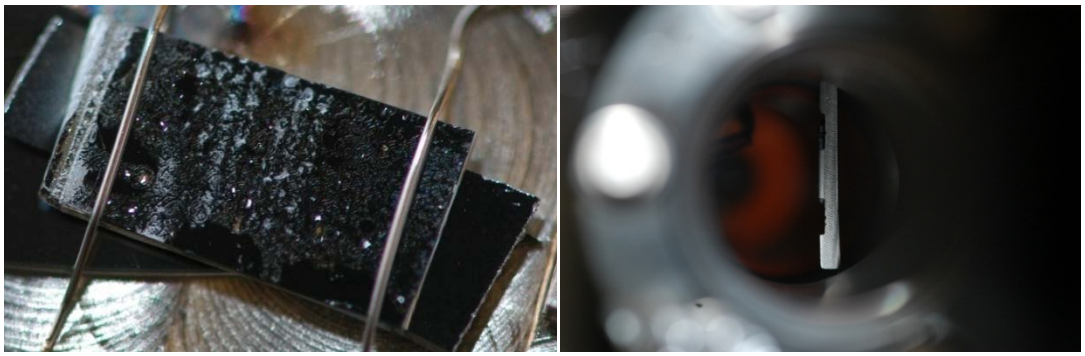

Fig. 4.2 The porous silica target after an experiment is shown in the photo on the left. A photo of the target just outside of the viewport.

The SSPALS voltage signal is composed of two different integrated voltage's coming from one single shot of gamma rays. The two voltage's obtained from the detector have different time limits used for integration. The prompt peak, which is the time the

integrated signal spans from -50ns to 300ns, is used to estimate the total Ps formation detected from the target. The delayed fraction, which spans from 50-300ns, is a measurement of the remaining long lived triplet state Ps atoms. Both components are shown in the SSPALS measurement using the accumulator with no laser, as shown in Fig. 4.3.

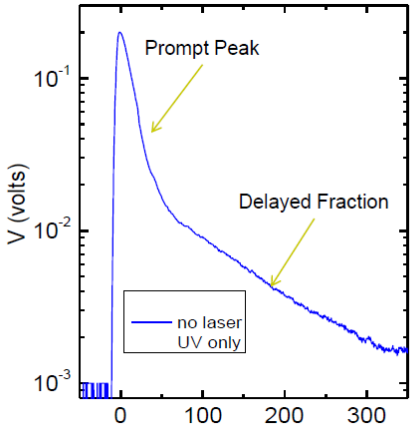

Fig. 4.3 SSPALS of slow Ps atoms emitted from the target. The prompt peak is the between the time spans of -50ns to 50ns. The Delayed peak is plotted from 50ns to 300ns.

The delayed fraction is defined as:

$$f_d = \int_{50}^{300} V(t)dt \Big/ \int_{-50}^{300} V(t)dt$$

V(t) is the detector voltage output, and the denominator is very similar to the numerator but it includes the time of the prompt peak, -50ns to 300ns. The prompt peak is measurement of the fast decaying Ps atoms and the remaining triplet state Ps atoms. The average overall delayed decay for the triplet Ps atoms is given as:

$$f_3 \cong f_d e^{t/\tau}$$

where τ is the mean lifetime of delayed Ps annhiliation and t=50ns. A 10% beamsplitter was used to reflect 532nm light into the same scintillator and PMT used to detect the Positronium annihilation gamma rays. A cartoon is shown in Fig. 4.4 which shows the UV light and Ps interaction region

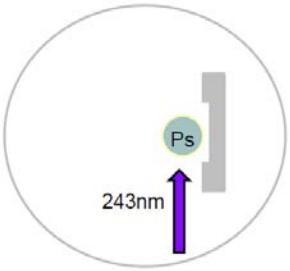

Fig. 4.4 Ps and Laser interaction region.

Within the interaction region the UV laser beam was aligned to avoid hitting the target directly as this light could create short and long lived paramagnetic centers which could effect the formation of Ps atoms[78].

Our signal occurs by the following sequence of events. The Ps within a magnetic field absorbs a photon from the ground state 1^3S_1 to the $2^3P_j(j = 0,1,2)$ state. Upon excitation to the 2p states the magnetic field mixing occurs in which some of the 2^3P states mixes with the 2^1P states. The estimated mixing value is about 10% within a 700 Gauss field. The excited 2p atoms then decay back down to the 1^3S_1 and 1^1S_0, whereupon in the 1^1S_0 state the atoms quickly decay into two gamma rays. In Fig. 4.5 we show the sequence of events.

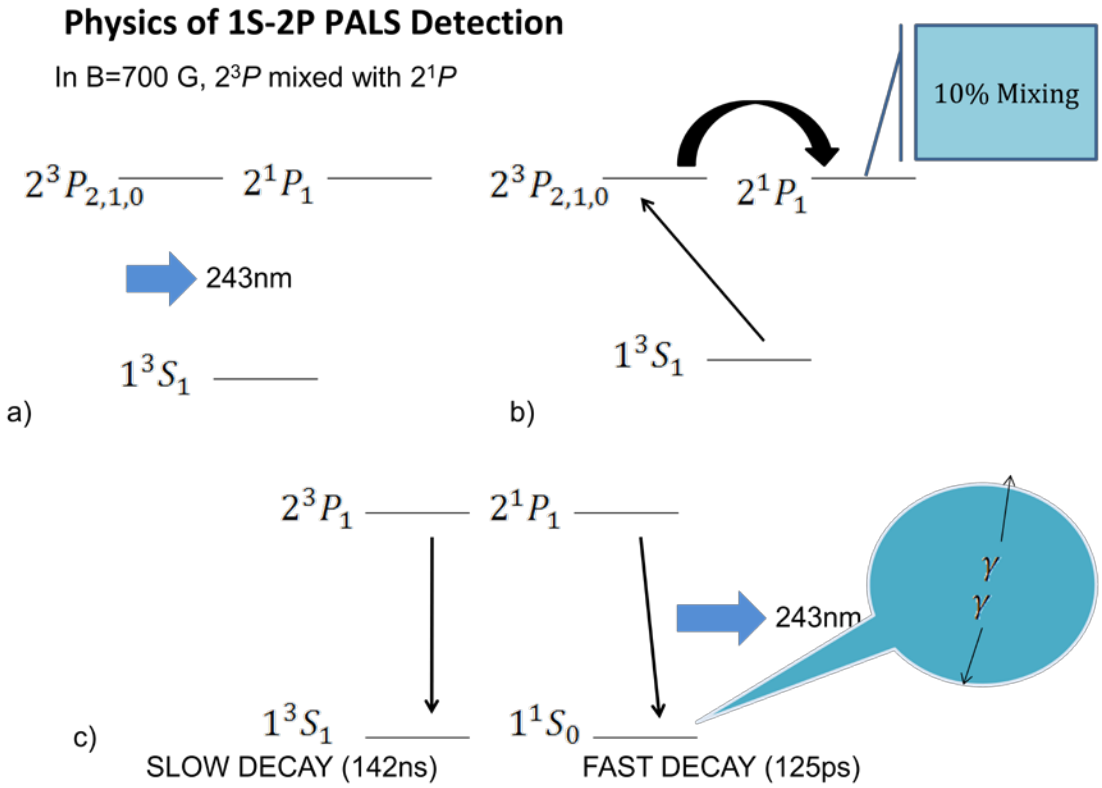

Fig. 4.5 The sequence of events that occur for laser excited SSPALS with a Alpha Lyman photon within a 700 Gauss field along the Ps beam axis. The sequence of events begins with a) a incident 243nm photon and a ground Ps atoms. b) Photon absorption occurs to excite the Ps atom from the ground state triplet level to the excited 2p triplet and 2p singlet state. The 2p singlet state excitation occurs thru mixing/quenching effect. c) After absorption the spontaneous emission occurs with the increased amount of gamma rays to detected to show that a laser induced effect occurred within the laser + Ps overlap region.

The events are also shown in the sequence given below:

$$1^3S_1[142ns] + h\nu \rightarrow 2^3P_j + 2^1P_0$$
$$2^1P_0 \rightarrow 1^1S_o[125ps] + h\nu \rightarrow 2\gamma$$

A figure of the measurement of both the gamma rays and laser induced signal is shown

in Fig. 4.6.

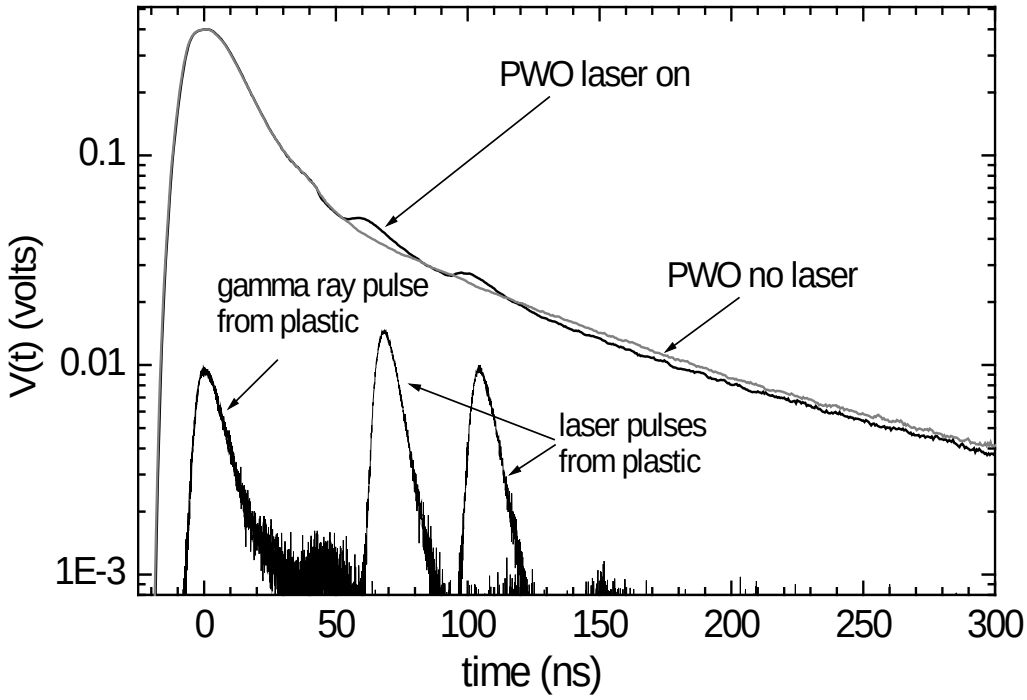

Fig. 4.6 The figure is taken from [16]. The single-shot annihilation lifetime spectra is obtained from the high density Ps accumulator. Note the laser pulse events were detected with the annihilation event at 70ns and a 2nd event at 110ns. Notice the decreased amount of long lived o-Ps atoms after the 2nd laser pulse , shown in the "PWO laser on" trace. This is reflected in the physics of the 1S-2P mixing with a 0.16T magnetic field mentioned in which the 2^3P states mixes with the 2^1P states and radiatively decay back down into the 1^1S_0 state. In the 1^1S_0 the p-Ps atoms decay quickly into two gamma rays. The measured signal was an average of 10 individual shots.

In Fig. 4.6 we also demonstrated that two laser pulse events could occur within the same single shot annihilation spectra. The reflected UV pulse diameter was approximately three times greater than the input pulse. With such a long delay of ~40ns for the 2nd UV pulse the area of the Ps cloud would become larger and an increase in the overlap would produce a constant integrated voltage signal that is similar to the 1st Ps + Laser event, even though a decrease in the energy reflected back would lower the voltage amplitude of the integrated signal.

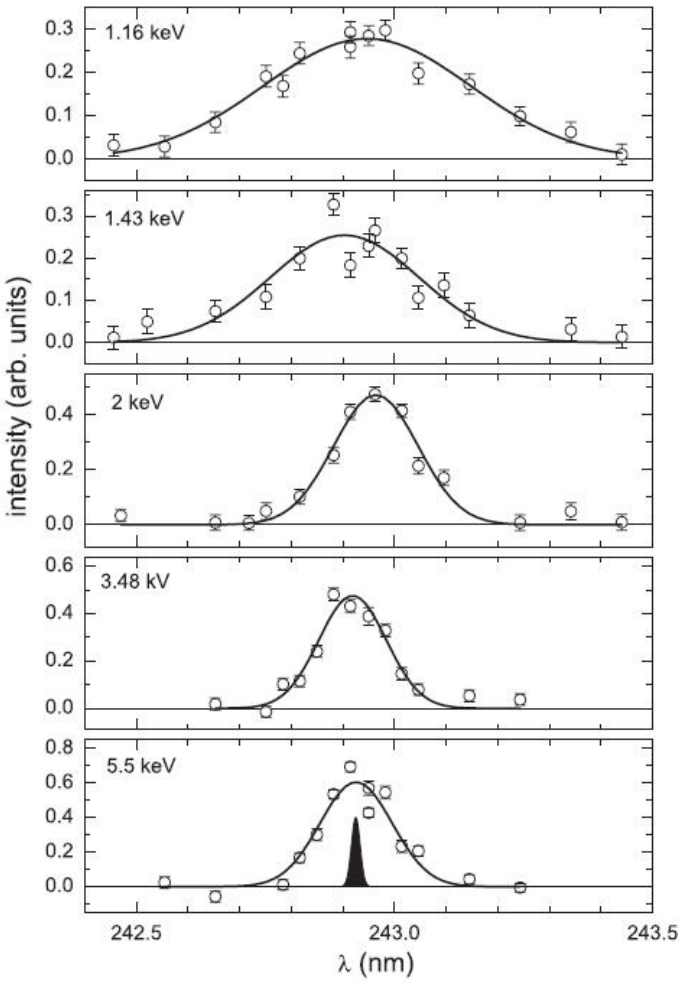

Fig. 4.7 Figure adapted from [16]. Doppler Profile of the $1^3S - 2^3P$ excitation of Ps emitted perpendicular from the Porous Silica target. The laser is directed parallel to the surface of the target. Variation of the peak wavelength is offset due to the laser calibration.

The laser induced signal of the $1^3S - 2^3P$ transition is measured with the wavelength tuned across the resonance. The scan is shown in Fig. 4.7 by plotting the difference of the “laser on” and ”no laser” trace as a function of the wavelength. Each point along the

trace is an average of ten shots with the standard deviation of the ten shots. The trace is fitted to a Gaussian distribution according to the expression:

$$P(\lambda) \propto \exp[-\frac{(\lambda-\lambda_o)^2 c^2}{2\lambda_o^2 c^2 \langle v_x^2 \rangle}]$$

where λ_o=243nm is the line resonance of the Alpha Lyman transition. The Doppler width FWHM, $\Delta\lambda$, is

$$\frac{\Delta\lambda}{\lambda_o} \approx 2\sqrt{2\ln 2}\sqrt{\langle v_x^2 \rangle / c^2}$$

From the fit at different implantation energies the motion parallel to the surface or kinetic energy can be measured. We plot E_x as a function of the positron implantation energy as shown in Fig. 4.8. As the implantation energy increased further past 3 keV, the kinetic energy of the Ps atom reached a lower limit of 42meV.

The Ps energy loss mechanism due to collisions with atoms of other gases and grains, when assuming a classical model, has been successful in describing the cooling rates of Ps in materials with mean free paths of 5 -70nm[79]. The Ps atoms are assumed to be in the ground state and constantly lose energy after each collision with a heavier particle. But the Ps de Broglie wavelength is given by the expression:

$$\lambda_{Ps} = \frac{h}{\sqrt{2m_{Ps}E_{Ps}}} \sim 0.9nm\sqrt{1eV/E_{Ps}}$$

Where the kinetic energy is E_{Ps}. Using this expression we can conclude the de Broglie wavelength approaches the size of the pores 4.4nm for a 42meV Ps atom. For a 400meV Ps atom the de Broglie wavelength reaches 1.4nm.

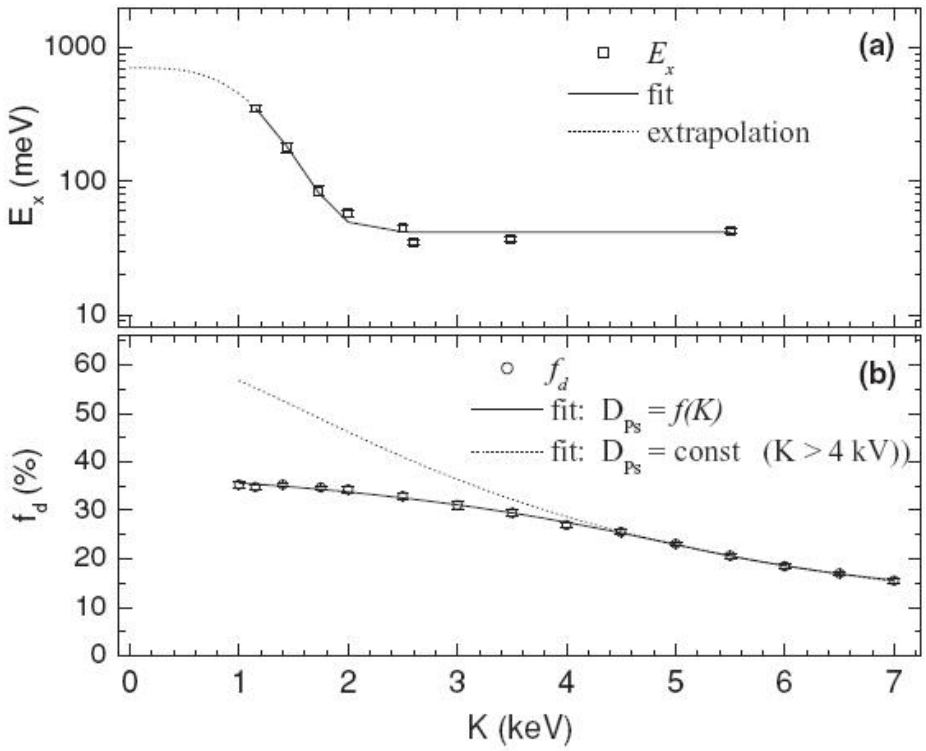

Fig. 4.8 Figure adapted from [16]. Plot of the kinetic energy parallel to the target surface vs the positron pulse implantation energy.

We measured the temperature of the emitted Ps along the x-axis near the surface of the porous silica. The expected outcome of having a deeper implantation depth would produce slower Ps atoms due to the increased interaction with the walls and the number of collisions that would occur within and in between the target pores. But the energy measured reached a limiting value of $41.7 \pm 2.7\ meV$.

This energy is corresponds to the lowest state energy of Ps confined in a infinite well, or an idealized spherical pore of radius a and diameter d=2a given the expression

$$E_o = \frac{\pi^2 \hbar^2}{2 m_{Ps} a^2} = 753 meV \left(\frac{1nm}{d}\right)^2$$

With a pore size of 2.4nm, we obtain $E_o = 131meV$. To compare the confinement energy to the measured value we need a factor η that is related to the angular distribution of emission. We assume the angular distribution is proportional to $cos\theta$, where the angle θ is between the angle of emission and the normal angle of the surface. We assume a constant distribution along the azimuthal direction, and projection of the angle is $\sqrt{v_o^2 - v_x^2}$, where $v_x^2 < v_o^2$. The kinetic energy along the x –direction is then

$$\langle v_x^2 \rangle = \frac{\int_0^{v_o} v_x^2 \sqrt{v_o^2 - v_x^2} dv_x}{\int_0^{v_o} \sqrt{v_o^2 - v_x^2} dv_x} = \frac{1}{4} v_o^2$$

This implies that $\eta = 4$.

Positronium Speed Distribution Normal to Surface

The positronium triplet state velocity distribution was measured along the laser's axis using the Alpha Lyman transition [16] parallel to the porous silica's surface. But the angular dependency of the velocity distribution was not resolved given the small separation distance(~3") between the front of the detector and interaction region. The detection apparatus uses a photomultiplier tube combined with a scintilllator to detect the annihilation of Ps gamma rays near the surface of the target.

We've assumed a $cos\theta$ angular emission dependence, where θ is angle of emission with respect to the normal direction from the surface. It was shown that a

factor $\eta = 4$ was needed to compensate the difference in the confinement energy of 131meV and the measured 42meV obtained from our data.

But recent measurements have shown a higher resolved velocity distribution by measuring the Rydberg transitions using a time of flight tube which is extended from 100mm to a 1700mm. The experiments were done with two photon excitation using n=20 and n=30, chosen for its long radiative lifetime, large ionization threshold's, and large efficiency of excitation for a three level system [80].

Positrons were injected into the surface of the copper target using the source and trap with a transfer coil but with no accumulator. The e+ will lose energy and thermalize and diffuse to the surface to be reemitted as a Ps or Ps*. In our experimental setup the Ps atoms emitted were perpendicular to the surface. At the end of the flight tube, which is 1.7m away from the target, the multi channel plate's diameter is 50.8mm. This produced a field of view of 2 deg that the detection system would selectively measure from the surface, as oppose to the collection of gamma rays detected within <100 mm away. In our detection of Rydberg Ps atoms using a MCP we assume a low count rate for Compton rescattering of Ps annhiliation along the flight tube. With the two dye laser's pumped by a single Nd: YAG laser, the optical time delay was adjusted between the UV and NIR to <0.5ns, then adjusting the time delay between the arrival time of the positronium pulse and the laser pulse, the number of detected counts were maximized . In a single run, 5000 shots were measured over a time span of 24 hours,

with both the NIR laser tuned to the n=30 transition and the UV laser tuned to the peak position of Alpha Lymen transition.

In Fig. 4.9 is a plot of our data. The probability distribution function is given by the following expression.

$$P(v) = 4\pi(\frac{\beta m}{2\pi})^{3/2} e^{-\beta m v^2/2} v^2 \quad \text{Eq(1)}$$

The physical interpretation of the quantity $P(v)dv$ represents the fraction of atoms whose speeds lie in the range of v to v+dv. But the data corresponds to the probability of counts for the Rydberg Ps atom for a particular speed v. We must then multiply the probability distribution function by the speed,v , to relate the physical quantity of what was measured in the lab. We then take eq(1) and multiply by v.

$$P(v) \cdot v = 4\pi(\frac{\beta m}{2\pi})^{3/2} e^{-\beta m v^2/2} v^3 \qquad \text{Eq(2)}$$

By using expression (2), which is now probability speed distribution we fitted the data.

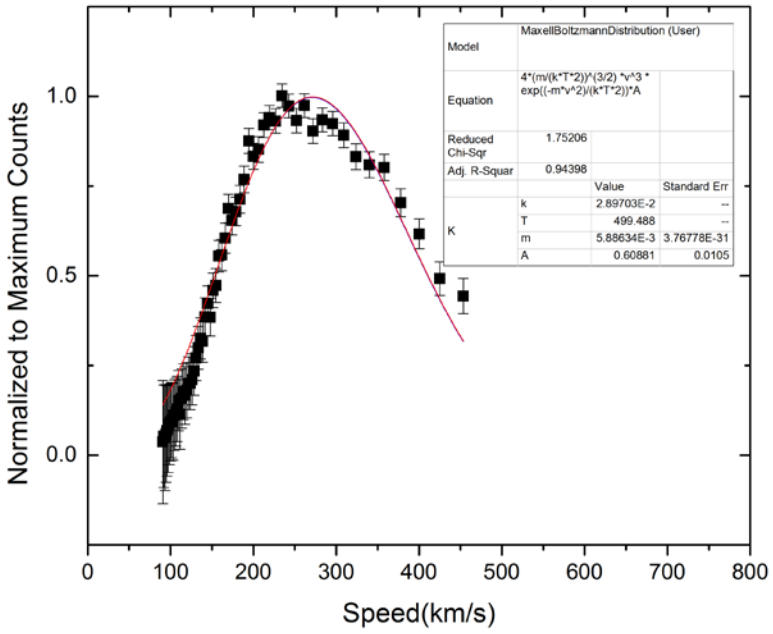

Fig. 4.9 Counts of Si p-type vs speed. Data of ion/accidental counts has not been included for speeds greater than 500km/s as the data are 5 SD away from the expected data. Data has been normalized to maximum number of counts.

The fit has a chi squared value of 1.75 which indicates a good fit to the expression. This seems to indication our observed Rydberg velocity distribution is consistent with the expected theoretical distribution. We can also look at the energy distribution of Ps atoms detected normal to the surface. We multiply the physical quantity kinetic energy, essentially v^2, to the probability distribution.

$$P(v) \cdot \frac{1}{2}mv^2 = 4\pi(\frac{\beta m}{2\pi})^{3/2}e^{-\beta m v^2/2}v^4 \quad \text{Eq(3)}$$

We make a transformation in terms of energy using $v = \sqrt{2E/m}$ and $dv = dE/\sqrt{2Em}$ and obtain our final expression:

$$P(E) \cdot E = 4\pi(\frac{\beta m}{2\pi})^{3/2}E^{3/2}e^{-\beta E}dE \quad \text{Eq(4)}$$

Using the expression we fitted to the data as shown in figure

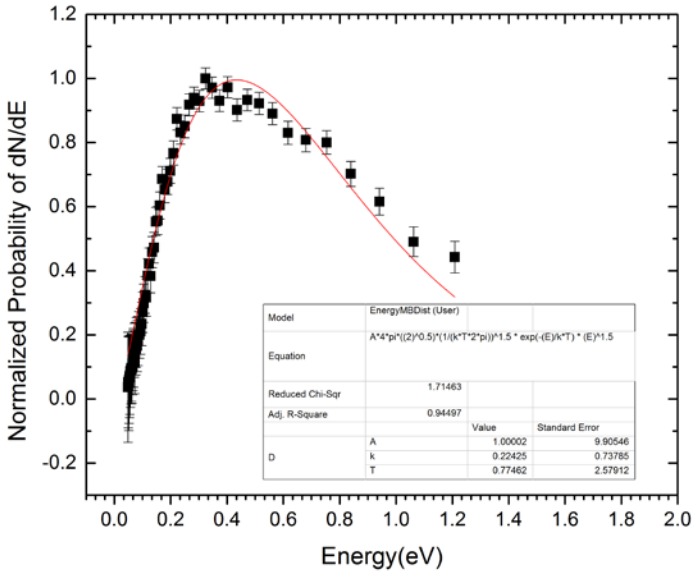

Fig. 4.10 Counts of Si p-type vs energy.

The chi squared value we obtain from Fig. 4.10 is 1.71, which indicates a good fit in our transformation of the speed distribution to an energy distribution. In retrospect we could of originally taken Eq.(1) and translate to an energy distribution by a change of variables but our expression would have a factor of $E^{1/2}$ instead of the $E^{3/2}$, as in Eq(4). Assuming that $E^{1/2}$ is correct the chi squared fit for $E^{1/2}$ is 12.17 which is indicates a disagreement. In performing a change of variables on Eq(2) we obtain a reduced chi square value of 3.99, which is also in disagreement of the theoretical fit. We conclude that we have established the first unambiguous measurement of the thermal distribution of Ps atoms for solid surfaces using Rydberg excitation. We also are able to obtain an energy distribution from a change of variables.

Laser Cooling

Laser cooling of neutral atoms is a very unique experimental method which can slow neutral atoms down in a vacuum to temperatures reaching the microkelvin range using photon exchange with the atom. Due to the overall charge of a neutral atom using a constant electric or magnetic field on an atom has no effect on its motion. To understand how photon exchange works we start with a stationary ground state atom and the incident photon tuned to the resonance of the quantum level's of the atom. The photon is propagating in the z-direction and carries a momentum of $p = h/\lambda$. The atom's initial momentum is zero. The photon is absorbed by the atom whereupon the electron is excited to a higher quantum level state and afterwards spontaneously emits the photon in an isotropic and random direction, also the orbital electron returns to its ground state level. Due to the random nature of the k-vectors of spontaneous emission, in a field free environment, this results in a zero final momentum exchange for the photon. Using the conservation of momentum, after N absorptions and spontaneous emissions, each photon passes on its momentum change, $p_f - p_i$, to the atom, and this results in a spontaneous force exerted on the atom in the direction of the laser. To get an experimental grasp of the numerical values we first look at the sodium atom, which is also the first atom of many atoms used in the demonstration of optical cooling.

The sodium atom has a mass of 23 A.M.U. and absorbs at around 620nm for the $3^2S_{1/2} \rightarrow 3^2P_{3/2}$ transition. Each photon exchange gives $\Delta v = 3cm/s$. A Na atomic

beam would roughly have a thermal velocity of 600m/s, so the number of photon exchanges that would slow the atoms down into the single digit speeds is roughly 20,000 exchanges. In 1975 $Hänsch$ and Schalow [81], conceived the idea of using a laser to capture and decelerate thermal atoms by tuning the laser below the atom's resonance. By detuning the laser off resonance the laser would be set to capture atoms that are opposing the direction of the laser as that is when absorption would occur due to the Doppler shift. The Doppler shifted frequency changes since each photon exchange of the many thousands that occur, produces an atom with a decreasing and changing thermal velocity and as result is no longer in tune with the laser's frequency. During the deceleration phase the absorption frequency is shifted for the atom after each exchange which is given by the following expression, $\omega(t) = \omega_o + k \cdot v(t)$. It was later discovered that two solutions were possible to overcome the ever changing Doppler absorption frequency in 1985.

In 1980 the first laser cooling experiment was demonstrated with Na atoms using a single counter propagating laser beam[82]. The atom's initial temperature of 600K was cooled to a temperature of 73K. In 1985 two groups demonstrated different techniques to overcome the changing doppler shifted absorption frequency, but both groups demonstrated the stopping of sodium atoms using a single counter propagating resonant laser beam. The first group led by Prodan and associates[83] used a spatially varying magnetic field to tune the slowing atom's resonance levels along the path of the beam thru Zeeman level's shifting, since the resonance of the atom's is shifted by the

expression $U_B = m_l \left(\frac{e\hbar}{2m_e}\right) B$, where $\left(\frac{e\hbar}{2m_e}\right) = 9.27 \times 10^{-24} J/T$ is the Bohr Magneton, for example for the $1s \rightarrow 2p$, the values would be shifted $f = f_o + \frac{eB}{4\pi m_e}$ for the $\Delta m_l = +1$. By slowing adjusting the magnetic field varied the shifted absorption frequency along the flight path of the atomic beam. This method produced a cloud of atoms with a temperature of 100K. The second group, Ertmer and colleagues[84] used a single counter propagating beam, but was frequency chirped the laser in time using an electro optics modulator, in order to keep the laser's frequency in resonance with the decelerating atom. This technique demonstrated a temperature value of 50mK.

In 1985 a two dimensional laser cooling scheme was used and demonstrated a temperature cooling of 3.5mK[85]. Within the same year Chu and colleagues at Bell Labs demonstrated confinement of atoms within three dimensions using the intersection of six laser beams within a vacuum for a period of 0.1 seconds[86]. Furthermore Chu showed that it was possible to cool at the quantum limit, of 240uK, which he won the Nobel Prize in Physics in 1996. In 1988 at NIST-Gaithersburg Lett. and his team cooled sodium atoms down to a temperature of 43 ± 20 uK which was below the Doppler limit [87]. A temperature of 0.6K corresponds to a thermal speed of 20m/s and at the uK range the atoms are near stationary, and it has been demonstrated that temperatures reaching the nano-Kelvin range are possible[88]. One of the many important applications of laser cooling is in the optical frequency standard, since the near zero

speed of the atom translates to a reduced Doppler effect and in addition increases the interaction time of the laser with the atom, i.e. reduction of transit time broadening[89].

Of the many atoms [90] that are possible to cool, one of the difficult challenges for experimentalists is the idea of cooling thermal Positronium atoms. The idea was promulgated by Liang and Dermer[91], and the authors both point out that cooling Positronium atoms "bottlenecked" by the Ps annihilation decay time associated with the ground state configuration in vacuum. The Ps atoms upon emission from solid surfaces convert into ground singlet and triplet state Ps atoms. Singlet atoms decay on the order of 0.125ns, would not be possible to laser cool these type of atoms since it is difficult to detect consecutive fast subnanosecond events in SSPALS within the prompt peak, which is less than 50ns. Also the idea of obtaining multiple laser pulses less than a time window of 50ns is only possible with deterministic Adiabatic Fast Passage with Red and Blue pulse laser cooling, which can be done on o-Ps states. The triplet ortho-Ps atoms, having a lifetime of 142ns, live long enough to have 30-50 photon exchanges is possible since the radiative lifetime of the 2P state is 3.2ns. The positronium atom has a mass of two electrons and absorbs at 243nm for the $1S_3 \rightarrow 2P_{2,1,0}$ transition. Ps is very light and with each photon exchange gives $\Delta v = 160{,}000 cm/s$, compared to sodium with $\Delta v = 3 cm/s$.

In the Fig. 4.6 we showed two laser pulse events within the same single shot annihilation lifetime spectra. The 2nd shot was obtained by positioning a 0 deg UV KRF

mirror 40 feet away. In Fig. 4.6 we demonstrate that it is possible to do multiple laser pulse events within the 50-300ns time window. We have planned in the future to produce a single generated laser pulse tuned to the red side of the Ps Doppler spectrum. This single high energy UV laser pulse tuned to the Red-side of the Doppler spectrum would be split into 4 beams using beamsplitters and sent thru a multipass optical setup at the target chamber with a 3-6ns delay for each pass. This would produce 16 pulses interacting with a single burst of Ps atoms emitted in front of the target. Each optical event with the Ps atom may possibly produce a 6Ghz shift, but using a spontaneous radiative cooling would reduce each optical event by roughly a factor of 2. A possible measurement of the Doppler spectrum would then demonstrate a Doppler spectrum with 50Ghz shift which would be approximately 0.01nm at 243nm. This can be a first demonstration of 1-dimensional laser cooling for multiple pulsed events with Ps atoms and with success provide a motivation for creating greater than 16 events with controlled Adiabatic Fast Passage. Another limiting factor in the development of laser of Ps atoms is the generation of multiple pulses. As of current date of 2014 there is no publication of laser technology that can generate more than 50 laser pulsed events within a 200ns time frame.

A problem still remains in producing 16 optical pulsed events, as the Zeeman mixing in the beginning of Chapter 4 shows an ever decreasing population of remaining triplet state Ps atoms upon each 1S-2P transition. This would result in an unobservable

laser cooling signal as after the 16th laser pulse there maybe no remaining triplet Ps atoms left for photoionization.

The Alpha Lyman transition is one that is chosen specifically for the Ps atom since the photon at this frequency produces the largest momentum exchange, of the many possible transitions that could be used which are listed by Liang and Dermer[91]. Note, Liang Dermer have calculated out the cool rate and Einstein Coefficents for numerous optical transitions including the two photon long lived Rydberg states and other helpful parameters such as. The cooling rate at saturation is given as[91]:

$$\frac{dv}{dt} = \frac{-Ahv}{mc}$$

Where the A is the Enstein Coefficient which is the radiative decay time of the Alpha Lyman Transition, h is the Planck's Constant, $m = 1.8 \times 10^{-27} kg$ is the mass of Ps, v is the frequency of the light. It is possible to do a two photon exchange to a Rydberg transition for laser cooling, and the possibility of the other photon sequences are derived in a table by Liang and Dermer[91]. The reason for doing a two photon exchanges is a promising path since the lifetime of the Ps atoms is extended due to the long radiative lifetimes. We will show from the data in the Rydberg spectroscopy section that Ps atoms show the Maxwell-Boltzman thermal speed distribution is around 250,000m/s. A flight path of 1.7m containing both 243nm and 730-750nm light between the MCP detection plate and target surface is possible, but the need for a cavity 1.7m long containing broad bandwidth 243nm light with 600Ghz wide profile is feasible with

the appropriate mirrors and aperture contained in the flight path. The flight tube with a 1.7m length is 5.5ft which necessitates the use of a laser pulse that is 5.5ns long. But since the overlap of the UV beam and NIR beam need to overlap the , but the experimental demonstration would need to be first done using 243nm light as it is lower in cost, using only one laser, and simpler to perform at the target surface. Since multiple pulses are needed for a single counterpropagating laser beam with the Ps cloud we would like to next mention the effect of "leakage" which reduces the overall cooling force exerted on the atom.

The chapter explains how leakage reduce's the effect of laser cooling which occurs when pumping the electron from a lower level state to higher level state, and each time the electron dexcites to a separate lower level . The Alpha Lyman transition is not a perfectly closed two level system. To describe a similar effect we look at the level diagram for Na, specifically the $3^2S_{1/2} \rightarrow 3^2P_{3/2}$, and in the next sub-chapter we will show the circumstances needed to obtain a near closed two level system in Ps. To elucidate further the idea of leakage, Phillips [92] describes this mechanism/observation of pumping a non ideal two level Na system with a dye laser. Any student would guess that if the atoms had a perfect two level excitation scheme that along the flight path with both the laser and atomic beam overlapping one another in opposite or counterpropagating direction, one could observe the flourecence by eye. The transition we speak of is pumping from the lower level $3^2S_{1/2}$ (F"=2) state to the higher level $3^2P_{3/2}$(F'=3) state. By eye the radiative decay or flouresence that occurs is visible along

the entire flight path of the chamber since the electron dipole excitation event's are infinite. But Phillips observed a peculiar event, the fluorescence light intensity was decaying further down the flight tube the atoms traveled. Phillips explains this phenonmenon paraphrasing that after excitation the flurosecence or dexcitation that occurs falls into the lower vibrational – rotational levels that are in the ground state that only a small fraction of the electrons return to the original $3^2S_{1/2}$ (F"=2) ground state and instead decay to the adjacent $3^2S_{1/2}$ (F"=1) hyperfine state[92]. This implied that Na atoms themselves did not have a constant source of ground state electrons to produce a photon exchange and as result reduced the laser cooling effect if not prevented the slowing of the atoms. But a solution was found by using a second pump laser tuned to compensate for the hyperfine interval in the ground state which repumped the leaking $3^2S_{1/2}$ (F"=2) to the $3^2P_{3/2}$(F'=3) state. An additional modulated frequency was superimposed on the primary optical frequency to "repump" the 2nd ground level, $3^2S_{1/2}$ (F"=1) state.

The idea of optical leaking was also observed in positronium and is discussed in Chapter 4 thru the idea of magnetic quenching/mixing in the 2P state. To recap this effect the electron in the Ps atoms is pumped from the $1S_3 \rightarrow 2P_{2,1,0}$ state. As result of the magnetic quenching that occurs, the 2P triplets are converted to 2^1P states, and upon decaying, traces back to the 1^1S_0 state where upon in the singlet state decays quickly within 0.125ns. To prevent such a leakage a magnetic field must be applied in order to suppress the quenching that occurs in the 2P state. In the next chapter we will

discuss the calculation of the predicted values for quenching that occurs and show that the suppression occurs for magnetic fields greater than 2T.

Laser Excitation in Paschen Bach Regime

Another experiment involved the excitation of the vacuum ground state Ps atoms using the 1S-2P transition in a 2.0T magnetic field. In the previous chapter we mentioned that the "leakage", which in actuality describes the conversion of long lived triplet state Ps atoms into short lived singlet state Ps atoms, depletes the initial population of ground state triplet atoms upon each laser pulsed event. This conversion is evident in Fig. 4.6 and in Cassidy's experiment [16] which demonstrates the depleted triplet population after the second UV laser pulse. The cause of the mixing occurs due to the externally applied magnetic fields that the Ps atom is in when excited in the 2p state.

It is known that the Hamiltonian in the 2P state, with no perturbation, has eigenvalues that represent the energy levels that make up the n=2 state. With no field applied the energy levels will stay in the same relative position's with respect to one another.

But, with a perturbation added we know that quantum mechanically the levels will shift relative to one another. It is not enough to use the fundamental expression

$U_B = m_l \left(\frac{e\hbar}{2m_e}\right) B$, for the $1s \rightarrow 2p$ transition, for which the corresponding eigenstate, $\Delta m_l = +1$, would produce a frequency shift of$f = f_o + \frac{eB}{4\pi m_e}$. We must start with the perturbed Hamiltonian, which for the Ps n=2 state is a 16 x 16 matrix. The recipe for finding the energy shifts is: 1) Find the eigenvalues of the perturbed matrix. 2) Find the eigenvectors from the eigenvalues of the matrix. The eigenvectors themselves are important as the coefficients in front of each basis represent the makeup or total superposition of states that exist for each eigenvector that is found for each corresponding eigenvalue. The basis physical represent the states at zero electric and magnetic fields. Once the eigenvectors are found one can then diagonalize the matrix. And after diagonalizing the perturbed Hamiltonian with the newly found eigenvectors, the new shifted energy values of all 16 levels can be found from the diagonal elements for a specific numerical magnetic field. To observe how the levels change and shift with respect to one another for a different magnetic field, one can diagnolize the 16x16 Hamiltonian again for 8-10 different magnetic field values[93].

It is also known that the magnetic field produces crossings in the 2p state as the magnetic field changes. As a result even a small electric field can mix the $^3S_1(m_j = \pm 1)$ with the $^3P_2(m_j = 0)$ in the neighborhood of the crossing[93].

The experiment involved the use of the accumulator producing 2×10^7 positrons, with p-doped Silicon target. The time width of the positron pulse is 1ns. The magnetic field is applied perpendicular to the sample and varied in magnitude from 0.1T

to 2.0T. The laser consists of a Q-switched Nd: YAG laser which pumps a dye laser at 486nm. The 486 light is doubled inside a nonlinear BBO crystal as described in earlier chapters. The maximum amount of UV energy is 1mJ/p. We then tuned the wavelength to the 1S-2P transition at the vacuum wavelength of 243.02nm.

Results

We found two very important effects occurring from 0.1 T and at magnetic fields greater than 2T. We can see this in Fig. 4.11, for the first effect, as we are measuring the delayed fraction or the long lived ground state triplet Ps atoms being produced from the accumulator, defined within the 50-300ns time window. Now, the quenching or mixing of the ground state Ps atoms occurs with an increasing magnetic field as shown in Fig. 4.11a, the circle designated trace, i.e. “no laser”, and we observed the quenching effect on the ground state Ps atoms, which is converting the long lived Ps atoms into short lived Ps atoms, with no laser. Now we next observe the 2^{nd} and most important effect, we introduce the UV laser at low UV energies and measure the delayed fraction for various magnetic fields. This trace with the UV laser on at 100uJ/p is shown in the trace with the upright triangles in Fig.4.11a. Notice that signal, S(%), shown in Fig. 4.11b. represents the mixing or quenching that occurs in the 2P state at around 0.16T. The S% value is large due to the large mixing effect occurring at low magnetic fields at UV energies a factor of roughly two below the saturation limit, meaning that the energy is below the ionization limit but optical excitation of the Ps atoms occurs so that enough

triplet ground state Ps are driven into the 2P state. If the energies are larger than 100uJ than saturation will occur which has a near equal amount of electron's driven down due to Rabi oscillations, and electron's driven up due to absorption.

The mixing of the 2P is well known [32,94] and is due to the magnetic field which produces Zeeman mixing of the 2P excited state. The most interesting result is that the mixing in the 2P state at 100uJ is reduced as we increase the magnetic field, as shown in Fig. 4.11a, i.e. upright triangles. The mixing reaches zero as we approach magnetic fields larger than 2.0T. An important question arises. Is there no longer atoms in the excited 2P state? Or is there no longer any ground state triplet atoms to be excited since all of triplet ground state atoms have converted to singlet state atoms. The answer to the question is that in experiment we are exciting triplet state Ps atoms at magnetic fields greater than 2T to the 2P state. The delayed is defined as the amount of triplet state Ps atoms remaining within the 50-300ns time window. If there were none, then $f_D$would be reduced to zero, which indicates a process occurring within the optical excitation process.

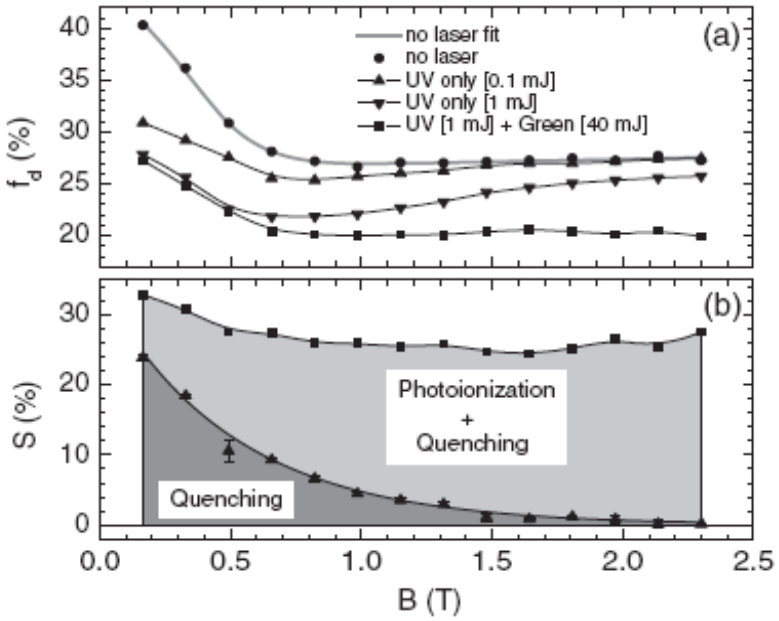

Fig. 4.11 Figure taken from [18]. The delayed fraction, f_D, and the laser induced excitation, S%, plotted as a function of the magnetic field B. The S% is the difference between laser on and no laser for UV only at 0.1mJ, UV only at 1mJ, and UV at 1mJ + Green at 40mJ/p. Notice the S(%) is constant at around 25% for the scenario of UV + Green and at the largest quenching value of only UV at 0.1mJ is 24%. This implies that quenching is suppressed in the optically excited 2P triplet state as the magnetic field is increase beyond 2T.

The signal, S%, which represents laser excited mixing of the 2p state is roughly about 25% at maximum, which occurs at 0.16T, with only 100uJ. Now increasing the energy of the UV pulse to 1mJ, which is roughly a factor of 2-3 over the saturation limit insures that all the ground state Ps atoms are excited to the 2P, and insures that the mixing in the 2P state will be observed. The signal, S%, as result decreases from 31% to 27.5%, which indicates more mixing occurring in the 2P state at the low field's, 0.16T. With evidence of more mixing at 1mJ/p at low magnetic fields the field is again slowly increased to 2T. At around 2.3T the S% laser induced signal is no longer zero. This means

that the mixing maybe occurring in the 2p state at high magnetic fields, but the quenching effect is reduced with some ionization occurring with two UV photoionization. Now, to test whether quenching is occurring, the 532 photoionizing pulse is introduced. The 532 energy, which requires around 40mJ/p to have the correct photon density to photoionize excited state 2p atoms is shown in Fig. 4.11a, i.e. “square” trace. Notice the S% is 28% with 1mJ of UV plus the 532nm laser pulse! With 100uJ of UV with no green laser, the S% was 24%, which is below the saturation. This very important effect means one thing, for the 1mJ UV plus 40mJ of green light, that quenching of “only” optically excited 2p state is reduced at large magnetic fields greater than 2T! This is also more evidence as the trace of 1mJ of UV plus 532nm light at low magnetic fields is reduced and the S% is also reduced. The S% is constant at a value of 26% from 0.16 – 2.3T. A

The important result is that in Fig. 4.11b shows that quenching is suppressed at large magnetic fields for optically excited 2p state atoms, and a diagram is shown in Fig. 4.12 to illustrate the suppressed quenching effect.

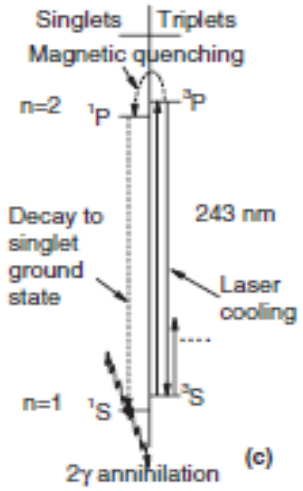

Fig. 4.12 Figure taken from [17]. Mechanism of quenching of optically 2P triplet state atoms is suppressed. At larger magnetic fields the Ps atom no longer decays to the singlet ground state level. Instead a closed 2P transition occurs at large magnetic fields.

Discussion

Since the 2P quenching is suppressed at large magnetic fields the mixing is reduced. The large impact that follows is that multiple laser pulsed events are possible, i.e. laser cooling. Now we discuss the mechanism of the suppressed quenching effect at larger in the high field limit. The Paschen Back regime produces eigenvectors divided into two classes. 1) Eight eigenstates with $m_s = \pm 1$, and these states have no singlet component, as the quantum state m_s represents currents produced by the positron and electron cancel the total magnetic moment of the Ps atom. Since the magnetic moments cancel each other out, Zeeman perturbed energy shifts do not occur, as a result the energy levels are constant with an increasing magnetic field. 2) The 2nd class of atoms are the $m_s = 0$ eigenstates. These states have a corresponding energy shift of

$\pm 2\mu_B B$, which is made of singlet components. Because of the magnetic quenching that occurs for the ground state Ps atoms in high fields, the measured delayed fraction must only occur with the eight eigenstates with $m_s = \pm 1$, and excitations from the $m_s = 0$ triplet ground state are ignored, as the energy levels shift.

Light traveling across the sample has an electric field polarized in the z direction, and this polarization has a matrix that couples to the $m_l = 0$, and only to this state, in the 2P excited state. Starting from the triplet $m_s = 1\ state\ or\ |1^3S_1\rangle$ light couples only to the state $\sqrt{1/2}[|2^3P_2(+1)\rangle + |2^3P_1(+1)\rangle]$. This is an eigenstate in the high field limit. This state is uncoupled from the singlet 2P state, which results in no quenching. Additional details with the theoretical calculation and analysis is supplemented by Professor A.P. Mills Jr. as is the flow and direction of the details of the physics. The calculation is a supplement to explain the suppression of the field mixing that occurs in low and high magnetic fields in the Ps 2P state and as result demonstrates the conditions needed for producing a optically excited closed two level system needed for laser cooling.

Analysis of Excitation(by: A.P. Mills Jr.)

The Ps n=2 states are denoted $n^{2S+1}L_J(M_J)$.The highest angular momentum *P* state is the outer product $\left|2\,^3P_2(2)\right\rangle = \left|1,1\right\rangle_L \left|1,1\right\rangle_S$. Successive applications of the lowering operator [95] with the requirements of orthogonality [96] then gives us the complete set of sixteen *n*=2 states:

$$\left|2\,^3P_2(\pm 2)\right\rangle = \left|1,\pm 1\right\rangle_L \left|1,\pm 1\right\rangle_S$$

$$\left|2\,^3P_2(\pm 1)\right\rangle = \sqrt{\tfrac{1}{2}}\left[\left|1,0\right\rangle_L \left|1,\pm 1\right\rangle_S + \left|1,\pm 1\right\rangle_L \left|1,0\right\rangle_S\right]$$

$$\left|2\,^3P_2(0)\right\rangle = \sqrt{\tfrac{1}{6}}\left[\left|1,-1\right\rangle_L \left|1,1\right\rangle_S + 2\left|1,0\right\rangle_L \left|1,0\right\rangle_S + \left|1,1\right\rangle_L \left|1,-1\right\rangle_S\right]$$

$$\left|2\,^3P_1(\pm 1)\right\rangle = \sqrt{\tfrac{1}{2}}\left[\left|1,0\right\rangle_L \left|1,\pm 1\right\rangle_S - \left|1,\pm 1\right\rangle_L \left|1,0\right\rangle_S\right]$$

$$\left|2\,^3P_1(0)\right\rangle = \sqrt{\tfrac{1}{2}}\left[\left|1,-1\right\rangle_L \left|1,1\right\rangle_S - \left|1,1\right\rangle_L \left|1,-1\right\rangle_S\right]$$

$$\left|2\,^3P_0(0)\right\rangle = \sqrt{\tfrac{1}{3}}\left[\left|1,-1\right\rangle_L \left|1,1\right\rangle_S - \left|1,0\right\rangle_L \left|1,0\right\rangle_S + \left|1,1\right\rangle_L \left|1,-1\right\rangle_S\right]$$

$$\left|2\,^1P_1(\pm 1)\right\rangle = \left|1,\pm 1\right\rangle_L \left|0,0\right\rangle_S$$

$$\left|2\,^1P_1(0)\right\rangle = \left|1,0\right\rangle_L \left|0,0\right\rangle_S$$

$$\left|2\,^1S_0(0)\right\rangle = \left|0,0\right\rangle_L \left|0,0\right\rangle_S$$

$$\left|2\,^3S_1(\pm 1)\right\rangle = \left|0,0\right\rangle_L \left|1,\pm 1\right\rangle_S$$

$$\left|2\,^3S_1(0)\right\rangle = \left|0,0\right\rangle_L \left|1,0\right\rangle_S$$

A magnetic field along the *z*-axis only couples triplets and singlets having the same orbital quantum numbers. The Zeeman matrix elements are $\tfrac{1}{2} g\mu_B B_z = B_z \times [28.028\ \text{GHz/T}]$ times ${}_S\left\langle 0,0\right|(\sigma_{1z} - \sigma_{2z})\left|1,0\right\rangle_S = 2$. The non-zero matrix elements are

$$\left\langle 2^3S_1(0)\right|(\sigma_{1z} - \sigma_{2z})\left|2^1S_0(0)\right\rangle = 2$$

$$\left\langle 2^3P_2(1)\right|(\sigma_{1z} - \sigma_{2z})\left|2^1P_1(1)\right\rangle = \sqrt{\tfrac{1}{2}},\ \left\langle 2^3P_1(1)\right|(\sigma_{1z} - \sigma_{2z})\left|2^1P_1(1)\right\rangle = -\sqrt{\tfrac{1}{2}}$$

$$\left\langle 2^3P_2(0)\right|(\sigma_{1z} - \sigma_{2z})\left|2^1P_1(0)\right\rangle = \sqrt{\tfrac{8}{3}},\ \left\langle 2^3P_0(0)\right|(\sigma_{1z} - \sigma_{2z})\left|2^1P_1(0)\right\rangle = -\sqrt{\tfrac{4}{3}}$$

In the Paschen-Back[97] (high magnetic field) limit there are eight eigen states with field independent eigen energies:

$$\left|2\,^3P_2(+2)\right\rangle = \left|1,+1\right\rangle_L \left|\uparrow\uparrow\right\rangle$$

$$\sqrt{\tfrac{1}{2}}\left[\left|2\,^3P_2(+1)\right\rangle+\left|2\,^3P_1(+1)\right\rangle\right]=\left|1,0\right\rangle_L\left|\uparrow\uparrow\right\rangle$$

$$\sqrt{\tfrac{1}{6}}\left|2\,^3P_2(0)\right\rangle+\sqrt{\tfrac{1}{2}}\left|2\,^3P_1(0)\right\rangle+\sqrt{\tfrac{1}{3}}\left|2\,^3P_0(0)\right\rangle=\left|1,-1\right\rangle_L\left|\uparrow\uparrow\right\rangle$$

$$\left|2\,^3S_1(+1)\right\rangle=\left|0,0\right\rangle_L\left|\uparrow\uparrow\right\rangle$$

$$\left|2\,^3P_2(-2)\right\rangle=\left|1,-1\right\rangle_L\left|\downarrow\downarrow\right\rangle$$

$$\sqrt{\tfrac{1}{2}}\left[\left|2\,^3P_2(-1)\right\rangle+\left|2\,^3P_1(-1)\right\rangle\right]=\left|1,0\right\rangle_L\left|\downarrow\downarrow\right\rangle$$

$$\sqrt{\tfrac{1}{6}}\left|2\,^3P_2(0)\right\rangle-\sqrt{\tfrac{1}{2}}\left|2\,^3P_1(0)\right\rangle+\sqrt{\tfrac{1}{3}}\left|2\,^3P_0(0)\right\rangle=\left|1,+1\right\rangle_L\left|\downarrow\downarrow\right\rangle$$

$$\left|2\,^3S_1(-1)\right\rangle=\left|0,0\right\rangle_L\left|\downarrow\downarrow\right\rangle$$

and eight with energies proportional to *B*:

$$\tfrac{1}{2}\left[\left|2\,^3P_2(\pm1)\right\rangle-\left|2\,^3P_1(\pm1)\right\rangle\right]+\sqrt{\tfrac{1}{2}}\left|2\,^1P_1(\pm1)\right\rangle=\left|1,\pm1\right\rangle_L\left|\uparrow\downarrow\right\rangle$$

$$\tfrac{1}{2}\left[\left|2\,^3P_2(\pm1)\right\rangle-\left|2\,^3P_1(\pm1)\right\rangle\right]-\sqrt{\tfrac{1}{2}}\left|2\,^1P_1(\pm1)\right\rangle=\left|1,\pm1\right\rangle_L\left|\downarrow\uparrow\right\rangle$$

$$\sqrt{\tfrac{1}{3}}\left|2\,^3P_2(0)\right\rangle-\sqrt{\tfrac{1}{6}}\left|2\,^3P_0(0)\right\rangle+\sqrt{\tfrac{1}{2}}\left|2\,^1P_1(0)\right\rangle=\left|1,0\right\rangle_L\left|\uparrow\downarrow\right\rangle$$

$$\sqrt{\tfrac{1}{3}}\left|2\,^3P_2(0)\right\rangle-\sqrt{\tfrac{1}{6}}\left|2\,^3P_0(0)\right\rangle-\sqrt{\tfrac{1}{2}}\left|2\,^1P_1(0)\right\rangle=\left|1,0\right\rangle_L\left|\downarrow\uparrow\right\rangle$$

$$\sqrt{\tfrac{1}{2}}\left[\left|2\,^3S_1(0)\right\rangle+\left|2\,^1S_0(0)\right\rangle\right]=\left|0,0\right\rangle_L\left|\uparrow\downarrow\right\rangle$$

$$\sqrt{\tfrac{1}{2}}\left[\left|2\,^3S_1(0)\right\rangle-\left|2\,^1S_0(0)\right\rangle\right]=\left|0,0\right\rangle_L\left|\downarrow\uparrow\right\rangle$$

The triplet m=0 decay rate in a magnetic field *B* is[98]

$\Lambda'_{1,0}=(1+y^2)^{-1}(\Lambda_{1,0}+y^2\Lambda_{0,0})$,

where x = 0.2756×(B/1 T) and $y=x/[1+\sqrt{1+x^2}]$. Since our Ps detection interval extends from 50 ns to 300 ns, the m=0 contribution will be diminished to less than 1/e in fields greater than 0.3 T.

Our problem of laser excitation of Ps from the n=1 state is thus very simple because only the state $\left|1\,^3S_1(+1)\right\rangle = \left|0,0\right\rangle_L \left|\uparrow\uparrow\right\rangle$ will be present initially in high magnetic fields. Both optical and Stark electric fields only mix this state with P-states having the same spin quantum numbers. Since the four $\left|\uparrow\uparrow\right\rangle$ states are only mixed amongst themselves, the effect will be confined to shifts in the triplet levels. There will be strictly no Stark effect spin triplet-singlet quenching in the Paschen-Back limit.

The state reached via light rh circularly polarized (+ħ angular momentum relative to the z-direction) on $\left|1\,^3S_1(+1)\right\rangle$ is always the pure state $\left|2\,^3P_2(+2)\right\rangle = \left|1,+1\right\rangle_L \left|\uparrow\uparrow\right\rangle$ for which there is no singlet-triplet mixing[94]. On the contrary, lh circularly polarized light on $\left|1\,^3S_1(+1)\right\rangle$ gives a state $\left|1,-1\right\rangle_L \left|\uparrow\uparrow\right\rangle$ that begins as a mixture of the three unperturbed triplet P states with m_J=0:

$$\left|\psi(0)\right\rangle = \left|1,-1\right\rangle_L \left|\uparrow\uparrow\right\rangle = \sqrt{\tfrac{1}{6}}\left|2\,^3P_2(0)\right\rangle + \sqrt{\tfrac{1}{2}}\left|2\,^3P_1(0)\right\rangle + \sqrt{\tfrac{1}{3}}\left|2\,^3P_0(0)\right\rangle \ .$$

At intermediate magnetic fields, the triplet m=0 components of the states with J=0 and J=2 will mix with the singlet m_J=0 P states leading to quenching. Near the 1.65 kG level crossing of the two m_J=0 J=1 P states the state will oscillate between single and triplet (at ~10 MHz 6 G away from exact crossing which one could observe with our 15 ns time resolution). Even so, the fact that there is some singlet P present in the optically excited state means that the 1S-2P transition will be detected by the resulting quenching that should be present near the crossing, in contradistinction to the zero quenching one will

have for rh circularly polarized light. We are thus able to measure the polarization of the positrons $p=[S(lh)-S(rh)]/[S(lh)+S(rh)]$ directly and independent of calibrations because of the zero quenching effect for rh light. Beware, however, that at high laser intensities there will be photoionization when using rh light that will give pseudo quenching unless extrapolated to zero intensity.

The relevant Ps wave spatial functions are

$$\psi_{n=1,L=0,M_L=0}(\vec{r})=\left(\frac{1}{a_0}\right)^{3/2}\frac{2}{\sqrt{4\pi}}\exp\{-r/a_0\}$$

$$\psi_{n=2,L=1,M_L=0}(\vec{r})=\left(\frac{1}{2a_0}\right)^{3/2}\frac{z}{a_0\sqrt{4\pi}}\exp\{-r/2a_0\}$$

$$\psi_{n=2,L=1,M_L=\pm1}(\vec{r})=\left(\frac{1}{2a_0}\right)^{3/2}\frac{2^{-1/2}(x\pm iy)}{a_0\sqrt{4\pi}}\exp\{-r/2a_0\}$$

The non-zero matrix element with the Hamiltonian for the interaction with light $H_{\rm int}=e\vec{E}\cdot\vec{r}$ is, for $\vec{E}\cdot\vec{r}=Ez$,

$$M_{n=1\to n=2,L=1,M_L=0}=\int\left(\frac{1}{a_0}\right)^{3/2}\frac{2}{\sqrt{4\pi}}\exp\{-r/a_0\}\left(\frac{1}{2a_0}\right)^{3/2}\frac{eEr^2}{a_0\sqrt{4\pi}}\exp\{-r/2a_0\}\cos^2\theta 2\pi r^2 dr d\cos\theta=$$

$$\int_0^\infty 2^{-3/2}a_0^{-4}eE\exp\{-3r/2a_0\}r^4dr\int_{-1}^{1}\cos^2\theta d\cos\theta=2^{-3/2}a_0^{-4}eE4!\{2a_0/3\}^5\frac{2}{3}=\sqrt{2}2^7 3^{-5}eEa_0=\sqrt{2}M_0$$

For $\vec{E}\cdot\vec{r}=Ex$, we have

$$M_{n=1\to n=2,L=1,M_L=\pm1}(\vec{r})=\int eEx\left(\frac{1}{a_0}\right)^{3/2}\frac{2}{\sqrt{4\pi}}\exp\{-r/a_0\}\left(\frac{1}{2a_0}\right)^{3/2}\frac{2^{-1/2}(x\pm iy)}{a_0\sqrt{4\pi}}\exp\{-r/2a_0\}r^2 dr d\cos\theta d\phi=$$

$$\int eE\frac{1}{\pi}\frac{2^{-3}}{a_0{}^4}\exp\{-3r/2a_0\}r^4dr\int_{-1}^{1}(1-\cos^2\theta)d\cos\theta\int_0^{2\pi}\cos^2\phi d\phi=eE\frac{2^{-3}}{a_0{}^4}\frac{4}{3}4!(2a_0/3)^5=2^7 3^{-5}eEa_0=M_0$$

Linearly polarized light with the electric field in the *z*-direction has a transition matrix element that couples only to m_L=0 P states, so starting from the state

$\left|1\,^3S_1(+1)\right\rangle = \left|0,0\right\rangle_L \left|\uparrow\uparrow\right\rangle$ the light only couples to the vector $\sqrt{\frac{1}{2}}\left[\left|2\,^3P_2(+1)\right\rangle + \left|2\,^3P_1(+1)\right\rangle\right] = \left|1,0\right\rangle_L \left|\uparrow\uparrow\right\rangle$, which is an eigen vector in the high field limit and experiences no quenching. If we are not in the high field limit we must decompose this vector into its eigen vector components which then develop in time independently of each other. We find the $^1P_1$ amplitude of each of the three eigen vector components and sum the three squares to find the probability of radiative (or stimulated, if the laser bandwidth is broad enough to reach ~203 GHz down to the singlet ground state) decay to the singlet ground state.

Denote the zero field m=1 eigen vectors as $\hat{e}_1 = \left|2\,^3P_2(+1)\right\rangle$, $\hat{e}_2 = \left|2\,^1P_1(+1)\right\rangle$, and $\hat{e}_3 = \left|2\,^3P_1(+1)\right\rangle$. The eigen vectors in the presence of a magnetic field are

$\hat{\eta}_i = \sum_{j=1}^{3} M_{ij}\hat{e}_j$.

The light couples to the i-th field eigen vector with amplitude $S_i = \sqrt{\frac{1}{2}}(\hat{e}_1 + \hat{e}_3)\cdot\hat{\eta}_i = \sqrt{\frac{1}{2}}(M_{i1} + M_{i3})$. The amplitude for the i-th field eigen vector being in the singlet P state is M_{i2} so the probability of quenching to the singlet ground state given that there has been an excitation to the 2P states will be proportional to $\left|S_i M_{i2}\right|^2 = \frac{1}{2}\left|(M_{i1} + M_{i3})M_{i2}\right|^2$.

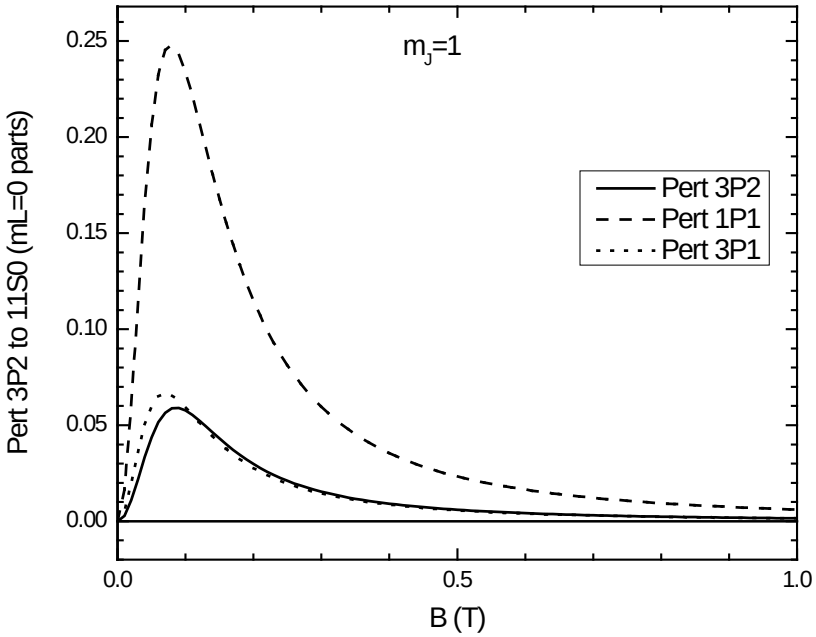

At 0.16 T the square of the amplitude for $\left|1\,^3S_1(+1)\right\rangle \rightarrow \left|1\,^1S_0(0)\right\rangle$ via the perturbed $\left|2\,^3P_2(+1)\right\rangle$ state at +1.676 GHz is 0.040

via the perturbed $\left|2\,^1P_1(+1)\right\rangle$ state at -3.243 GHz is 0.155

via the perturbed $\left|2\,^3P_1(+1)\right\rangle$ state at -8.316 GHz is 0.038

The mean energy is -3.23 GHz compared to the unperturbed n=2 triplet state at +7.645 GHz.

Linearly polarized light with the electric field in the *z*-direction has a transition matrix element that couples only to m_L=0 P states, so starting from the state $\left|1\,^3S_1(0)\right\rangle = \left|0,0\right\rangle_L \left|1,0\right\rangle_S$ the light only couples to the vector $\sqrt{\frac{2}{3}}\left|2\,^3P_2(0)\right\rangle + \sqrt{\frac{1}{3}}\left|2\,^3P_1(0)\right\rangle = \left|1,0\right\rangle_L \left|1,0\right\rangle_S$, which is not an eigen vector in the high field limit and does experience quenching. We decompose this vector into its eigen vector components which then develop in time independently of each other. We find the $^1P_1$ amplitude of each of the three eigen vector components and sum the three squares to find the probability of radiative (or stimulated, if the laser bandwidth is broad enough to reach ~203 GHz down to the singlet ground state) decay to the singlet ground state.

Denote the zero field m_J=0 eigen vectors as $\hat{e}_1 = \left|2\,^3P_2(0)\right\rangle$, $\hat{e}_2 = \left|2\,^1P_1(0)\right\rangle$, and $\hat{e}_3 = \left|2\,^3P_0(0)\right\rangle$. The eigen vectors in the presence of a magnetic field are

$\hat{\eta}_i = \sum_{j=1}^{3} M_{ij}\hat{e}_j$.

The light couples to the i-th field eigen vector with amplitude $S_i = \sqrt{\frac{1}{2}}(\hat{e}_1 + \hat{e}_3)\cdot\hat{\eta}_i = \sqrt{\frac{1}{2}}(M_{i1} + M_{i3})$. The amplitude for the i-th field eigen vector being in the singlet P state is M_{i2} so the probability of quenching (or stimulated emission by light of the same character as the exciting light) to the singlet ground state given that there has been an excitation to the 2P states will be proportional to $\left|S_i M_{i2}\right|^2 = \frac{1}{2}\left|(M_{i1} + M_{i3})M_{i2}\right|^2$.

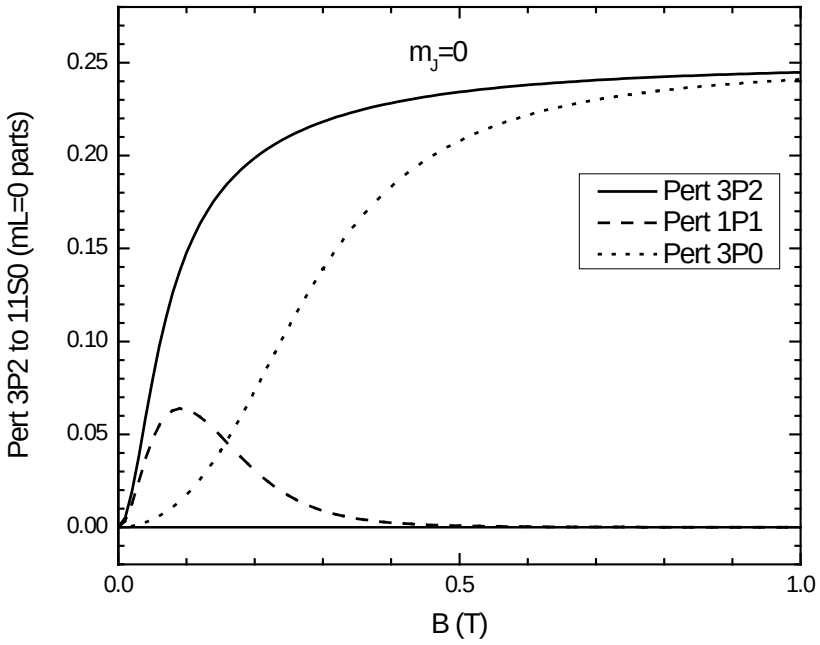

At 0.16 T the square of the amplitude for $\left|1^3S_1(0)\right\rangle \rightarrow \left|1^1S_0(0)\right\rangle$ via the perturbed $\left|2^3P_2(0)\right\rangle$ state at +1.805 GHz is 0.185, via the perturbed $\left|2^1P_1(0)\right\rangle$ state at -5.370 GHz is 0.045 , via the perturbed $\left|2^3P_1(0)\right\rangle$ state at -11.805 GHz is 0.047. The mean energy is -1.67 GHz compared to the unperturbed n=2 triplet state at +7.645 GHz

Linearly polarized light with the electric field in the *y*-direction has a transition matrix element that couples only to m_L=±1 P states, so starting from the state $\left|1\,^3S_1(+1)\right\rangle = \left|0,0\right\rangle_L \left|\uparrow\uparrow\right\rangle$ the light only couples 50% to the vector $\left|2\,^3P_2(+2)\right\rangle = \left|1,+1\right\rangle_L \left|\uparrow\uparrow\right\rangle$, which is a field independent eigen vector and does not quench, and 50% to $\sqrt{\frac{1}{6}}\left|2\,^3P_2(0)\right\rangle + \sqrt{\frac{1}{2}}\left|2\,^3P_1(0)\right\rangle + \sqrt{\frac{1}{3}}\left|2\,^3P_0(0)\right\rangle = \left|1,-1\right\rangle_L \left|\uparrow\uparrow\right\rangle$, which is an eigen vector in the high field limit. The light thus couples to each eigen vector with an amplitude equal to the inner product of that vector with $\left|1,-1\right\rangle_L \left|\uparrow\uparrow\right\rangle$.

Denote the zero field m=0 eigen vectors as $\hat{e}_1 = \left|2\,^3P_2(0)\right\rangle$, $\hat{e}_2 = \left|2\,^1P_1(0)\right\rangle$, and $\hat{e}_3 = \left|2\,^3P_0(0)\right\rangle$. The state $\left|2\,^3P_1(0)\right\rangle$ has no Zeeman coupling and is always an eigen state. The eigen vectors in the presence of a magnetic field are

$\hat{\eta}_i = \sum_{j=1}^{3} M_{ij}\hat{e}_j$.

The light couples to the i-th field eigen vector with amplitude $S_i = (\sqrt{\frac{1}{6}}\hat{e}_1 + \sqrt{\frac{1}{3}}\hat{e}_3)\cdot\hat{\eta}_i = \sqrt{\frac{1}{6}}M_{i1} + \sqrt{\frac{1}{3}}M_{i3}$. The amplitude for the i-th field eigen vector being in the singlet P state is M_{i2} so the probability of quenching to the singlet ground state given that there has been an excitation to the 2P states will be equal to $\left|S_i M_{i2}\right|^2 = \left|(\sqrt{\frac{1}{6}}M_{i1} + \sqrt{\frac{1}{3}}M_{i3})M_{i2}\right|^2$.

Denoting the Ps states as $n^{2S+1}L_J(M_J)$ we can easily see that an optical transition from the triplet m_s = 1 ground state $\left|1^3S_1(1)\right\rangle = \left|0,0\right\rangle_L\left|1,1\right\rangle_S$ (shown as a direct product of its orbital and spin components) can couple only to the following 2P states having both lepton spins up (↑↑) and with m_L determined by the light polarization:

$$\left|2^3P_2(+2)\right\rangle = \left|1,+1\right\rangle_L\left|\uparrow\uparrow\right\rangle$$

$$\sqrt{\tfrac{1}{2}}\overline{\overline{\left|2^3P_2(+1)\right\rangle}} + \sqrt{\tfrac{1}{2}}\overline{\overline{\left|2^3P_1(+1)\right\rangle}} = \left|1,0\right\rangle_L\left|\uparrow\uparrow\right\rangle$$

$$\sqrt{\tfrac{1}{6}}\overline{\overline{\left|2^3P_2(0)\right\rangle}} + \sqrt{\tfrac{1}{2}}\left|2^3P_1(0)\right\rangle + \sqrt{\tfrac{1}{3}}\overline{\overline{\left|2^3P_0(0)\right\rangle}} = \left|1,-1\right\rangle_L\left|\uparrow\uparrow\right\rangle.$$

In the high field limit these are pure eigenstates with field-independent eigen-energies; in zero field these are not eigenstates and the components of the compound P states will exhibit phase oscillations as a function of time. However in neither case is there any triplet-single mixing because the $^1P_1$ state is not involved. On the other hand, each of the states marked with a double overbar does contain a triplet m_s=0 component, for example

$$\left|2^3P_2(\pm1)\right\rangle = \sqrt{\tfrac{1}{2}}\left|1,0\right\rangle_L\left|1,\pm1\right\rangle_S + \sqrt{\tfrac{1}{2}}\left|1,\pm1\right\rangle_L\left|1,0\right\rangle_S,$$

which is coupled to the $^1P_1$ singlet states by a magnetic field in the *z*-direction, and which leads to the quenching in intermediate magnetic fields that we observe

	$^3P_2+2$	$^3P_2+1$	$^3P_20$	$^3P_2-1$	$^3P_2-2$	$^3P_1+1$	$^3P_10$	$^3P_1-1$	$^3P_00$	$^1P_1+1$	$^1P_10$	$^1P_1-1$	$^3S_1+1$	$^3S_10$	$^3S_1-1$	$^1S_00$
$^3P_2+2$	980															
$^3P_2+1$		980								αx						
$^3P_20$			980								γx					
$^3P_2-1$				980								αx				
$^3P_2-2$					980											
$^3P_1+1$						5365				$-\alpha x$						
$^3P_10$							5365									
$^3P_1-1$								5365				$-\alpha x$				
$^3P_00$									10851		βx					
$^1P_1+1$		αx				$-\alpha x$				3539						
$^1P_10$			γx						βx		3539					
$^1P_1-1$				αx				$-\alpha x$				3539				
$^3S_1+1$													7645			
$^3S_10$														7645		2x
$^3S_1-1$															7645	
$^1S_00$														2x		17778

Table 3.13 Coefficients 16x 16 of 2p states Ps

Underlined eigenvalues on the diagonal are negative, $\propto = \sqrt{\frac{1}{2}}$; $\beta = -\sqrt{\frac{4}{3}}$; $\gamma = \sqrt{\frac{8}{3}}$ and $x = \frac{1}{2} g \mu_B B_z = B_z \times [28.028\ \text{GHz/T}]$. The blank entries are zeros.

The m=±1 and m=0 sub spaces couple only within themselves:

	$^3P_2+1$	$^1P_1+1$	$^3P_1+1$
$^3P_2+1$	<u>980</u>	αx	
$^1P_1+1$	αx	<u>3539</u>	−αx
$^3P_1+1$		−αx	<u>5365</u>

	$^3P_20$	$^1P_10$	$^3P_00$
$^3P_20$	<u>980</u>	γx	
$^1P_10$	γx	<u>3539</u>	βx
$^3P_00$		βx	<u>10851</u>

Table 3.14 Coefficients of m=±1 and m=0 sub spaces.

The eigen value equation for the m=1 3x3 matrix is

$$(-980-\lambda)(-5365-\lambda)(-3539-\lambda)-(-980-\lambda)\alpha^2x^2-(-5365-\lambda)\alpha^2x^2=0\ .$$

The eigen values are determined by evaluating this expression for trial values of -60,000 MHz <λ< 60,000 MHz and picking out the values of λ at the three zero-crossing points.

The eigen vectors (1,a,b) corresponding to a given eigen value λ are found from the equations

$$b=(980+\lambda)/\alpha x\ \ c=-(980+\lambda)/(5365+\lambda)$$

The eigen value equation for the m=0 3x3 matrix is

$$(-980-\lambda)(-10851-\lambda)(-3539-\lambda)-(-980-\lambda)\beta^2x^2-(-10851-\lambda)\gamma^2x^2=0$$

The eigen vectors (1,a,b) corresponding to a given eigen value λ are found from the equations

$$b=(980+\lambda)/\gamma x\ \ c=\frac{\beta(980+\lambda)}{\gamma(10851+\lambda)}\ .$$

Fig 1S shows the eigen values and the $^1P_1$ amplitudes for the six eigen vectors.

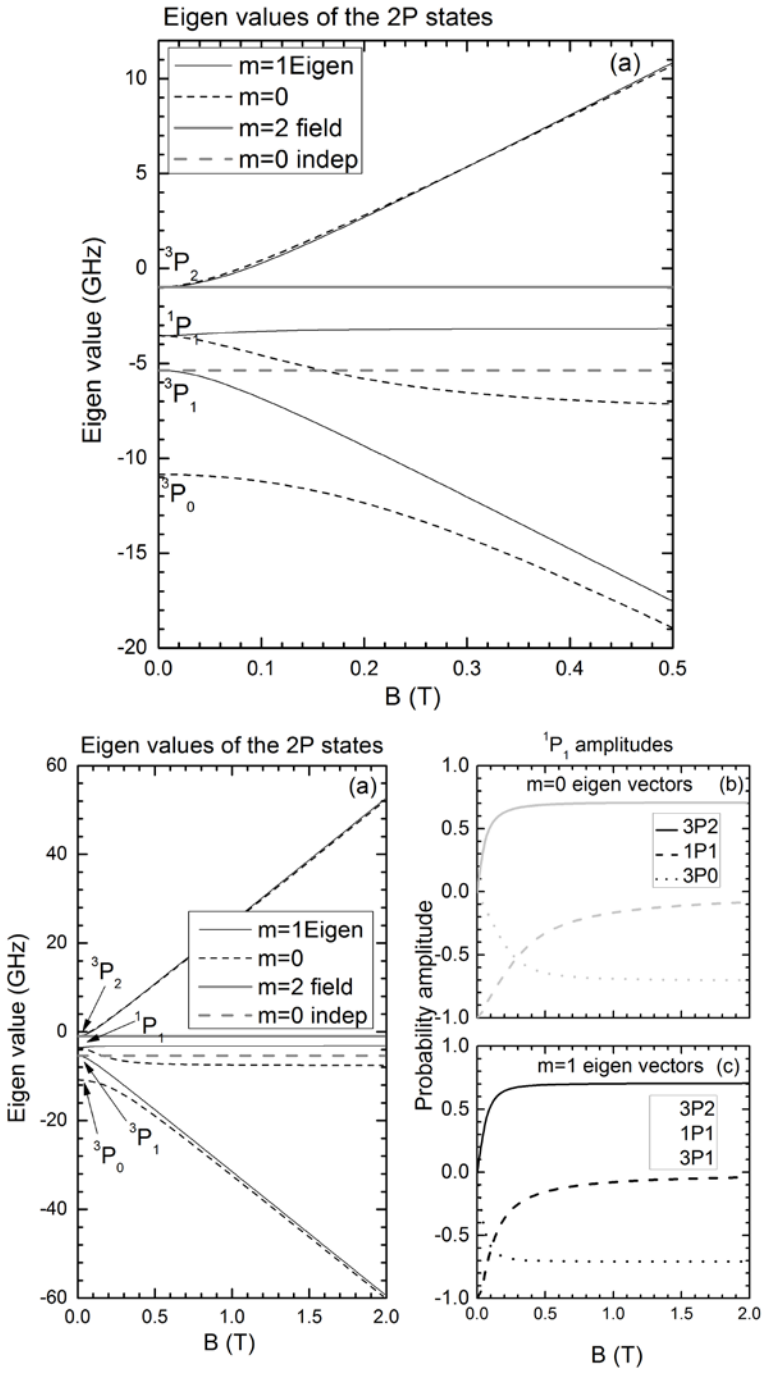

Figure 1S. Eigen values and $^1P_1$ amplitudes for the six eigen vectors that result from magnetic mixing of the triplet and singlet P states

References

[77]D.B. Cassidy, S.H.M Deng, H.K.M. Tanaka, and A.P. Mills Jr., Appl Phys. Lett. 88 194105(2006)

[78] D. B. Cassidy, K. T. Yokoyama, S. H. M. Deng, D. L. Griscom, H. Miyadera, H. W. K. Tom, C. M. Varma, and A. P. Mills Jr., Phys. Rev. B 75, 085415 (2007).

[79]H. Saito, T. Hyodo, New Directions in Antimatter Chemistry and Physics, edited by C.M. Surko and F.A. Gianturco (Kluwerm Dordrecht, 2001), p.101.

[80] F. Castelli, I Boscolo, S. Cialdi, M.G. Giammarchi, and D. Comparat, Phys. Rev A 78, 052512 (2008)

[81] T.W. Hansch, A. L. Schawlow, " Cooling of Gases by Laser Radiation,' Opt. Comm. 13,68(1975)

[82] V.I. Balykin, V.S. Letokhov, V.I. Mishin, " Cooling of Sodium Atoms by Resonant Laser Emission," Sov. Phys. JETP 51, 692 (1980)

[83]J. Prodan, A. Migdall, W.D. Phillips, I.So, H. Metcalf, J. Dalibard, " Stopping atoms with Laser Light," Phys. Rev. Lett. 54, 992 (1985).

[84] W. Ertmer, R. latt, J.L.Hall, M.Zhu," Laser manipulation of Atomic Beam Velocities: demonstration of Stopped Atoms and Velocity Reversal," Phys. Rev. Lett. 54,996(1985)

[85] V.I. Ballykin, V.S. Letokhov, and A.I. Sidorov, " Radiative collimation of an atomic beam by two-dimensional cooling by a laser beam,"JTEP Lett. 40. 1026, (1985)

[86] S. Chu, L. Hollberg, J.E. Bjorholm, A. Cable, and A. Ashkin, " Three-dimensional viscous confinement and cooling of atoms by resonance radiation pressure," Phys. Rev. Lett. 55, 48 (1985)

[87] P.D. Lett, R.N. Watts, C.I. Westbrook, W.D. Phillips, P.L. Gould, and H.J. Metcalf, " Observation of atoms laser cooled below the Doppler Limit," Phys. Rev. Lett. 61, 169 (1988)

[88] C. Salomon, J. Dalibard, W.D. Phillips, A. Clairon, S. Guellati: Laser Cooling of Cesium Atoms below 3uK" Europhysics. Lett. 12,683(1990)

[89] J.L Hall, M. Zhu, P. Buch ," Prospects for using laser prepared atoms fountains for optical frequency standards applications, " J. Opt. Soc. Am. B 6. 2194 (1989)

[90] W. Ertmer, R. Blatt, J.L. Hall " Some candidate atoms and ions for frequency standards research using laser radiative cooling techniques. Progr. Quantum Electron. 8, 249(1984).

[91] E. P. Liang, C.D. Dermer, Opt. Commun. 65, 419 (1988).

[92] Bill Phillips " Laser cooling and trapping of neutral atoms" Rev. Mod. Phys. 70(3), pg 721-741 (1998)

[93] S.M. Curry, Ph.D. Dissertation, Stanford University, Standford, CA, 1972.

[94] M. L. Lewis and V. W. Hughes, Phys. Rev. A **8**, 625 (1973).

[95] The raising and lowering operators are defined by $J_{\pm}|\, j,m\rangle = \sqrt{(j \mp m)(j \pm m + 1)}\,|\, j,m \pm 1\rangle$

[96]Lowering the above *P* state yields $\left|2\,^3P_2(1)\right\rangle = \sqrt{\frac{1}{2}}\left[|1,0\rangle_L|1,1\rangle_S + |1,1\rangle_L|1,0\rangle_S\right]$. Orthogonality of the *J*=1 triplet *P* state dictates $\left|2\,^3P_1(1)\right\rangle = \sqrt{\frac{1}{2}}\left[|1,0\rangle_L|1,1\rangle_S - |1,1\rangle_L|1,0\rangle_S\right]$, etc.

[97] F. Paschen and E. Back, Physica **1**, 261 (1921); E. U. Condon and G. Shortley, *Theory of atomic spectra,* Cambridge University Press, 1935) ch. 16.

[98] A. Rich, PhD Dissertation, University of Michigan, 1965 (University Microfilms, Ann Arbor, MI).

Chapter 5

Conclusion

Laser spectroscopy of Ps has advanced considerably due to the recent UCR experiments and we are in a position to explore many interesting topics, including ultrahigh precision 1^3S_1-2^3S_1, Rydberg Ps gravity, and Ps emission spectroscopy of the electronic states of metals.

With the Ps atoms emitted from p-doped Si surface has been shown in earlier chapters in context to Rydberg excitation, have speeds roughly equal to 200km/s. Each laser pulsed event provides $\Delta v = 1.60 km/s$. This implies at least 100 optical events to demonstrate laser cooling of Ps atoms. But it's up to the experimentalist to decide how many laser pulses is needed to provided a significant effect of laser cooling, and also what type of geometry should first be used. Should the laser excitation occur perpendicular to the target or parallel. It is not clear if multiple pulsed laser excitation should occur parallel to the target due to the Cosine angular emission dependence, but a 6Ghz shift was observed in the positronium hyperfine interval experiment [19]. 16 pulses only represents a shift of 100Ghz or 0.02nm. It is not clear which path to take for laser of Ps atoms, but the focus seems obvious in generating 100 pulses at around 100uJ per pulse, at 243nm with the ability to control the bandwidth.

Appendix A

Index Ellipsoid

The index of refraction of UV grade Fused Silica is the same for both s and p polarizations. But there are some materials in nature that have a different index of refraction depending on the polarization of light used with respect to the optical axis of a birefringent crystal. These materials are birefringent and have two indices of refraction given the input polarization, each the indices of refraction are called the ordinary and extraordinary index of refraction.

An example of a birefringent crystal is calcite, and when this crystal is placed over a sheet of paper with text everyone will notice that light will bend and form two images of the printed text from the paper. But if calcite crystal is lifted up and tilted so that the optical axis is aligned to your eye and you twist the crystal around the optical axis, you will see only one image. The index of refraction can be described for different angular orientation using the index ellipsoid. The index ellipsoid calculates the index of refraction of a crystal when the crystal is rotated away from its optical axis. We use the index ellipsoid as described in the [99]:

$$\frac{x^2}{\varepsilon_{11}/\varepsilon_o} + \frac{y^2}{\varepsilon_{22}/\varepsilon_o} + \frac{z^2}{\varepsilon_{33}/\varepsilon_o} = 1$$

For a uniaxial crystal, meaning $n_e < n_o$, we can define n_o and n_e as having the same indices of refraction along two of the crystal's axis, while the remaining third axis having a different value of the index of refraction n_e.

$$n_0^2 = \frac{\varepsilon_{11}}{\varepsilon_o} = \frac{\varepsilon_{22}}{\varepsilon_o} n_e^2 = \frac{\varepsilon_{33}}{\varepsilon_o}$$

The index ellipsoid then becomes

$$\frac{x^2}{n_0^2} + \frac{y^2}{n_0^2} + \frac{z^2}{n_e^2} = 1$$

If the wave was traveling parallel to the optical axis both polarizations of the wave will see no, as shown in the figure below. At angle pheta we need to take the cross section of the ellipse. The figure below shows the ponyting vector of the wave propagating at an angle pheta away from the optical axis. Taking the cross section of the ellipses at some angle pheta we have

$$n_e^2(\theta) = z^2 + y^2$$

$$\frac{z}{n_e(\theta)} = sin\theta$$

The equation of the ellipse is

$$\frac{y^2}{n_0^2} + \frac{z^2}{n_e^2} = 1$$

We finally obtain

$$\frac{1}{n_e^2(\theta)} = \frac{cos^2\theta}{n_0^2} + \frac{sin^2\theta}{n_e^2}$$

As the pontying vector reaches 90 deg the index of refraction approaches ne(90deg)=ne. If the light's polarization vector direction is rotated such that the electric field has components along the x and y axis, then the light will be rotated since the phase will differ between the two polarization with the thickness of the crystal.

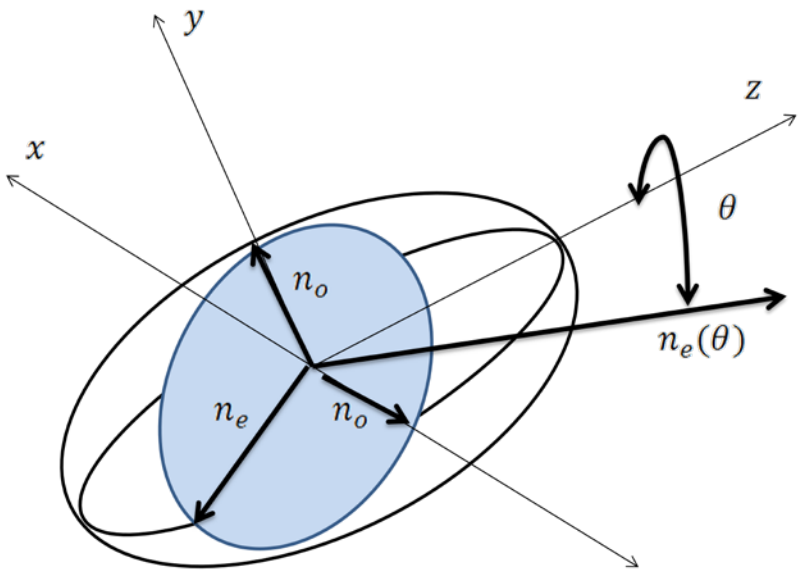

Fig. A.1: Index Ellipsoid of a crystal rotated away from the z-axis. Notice that when $\theta = 0\ deg$, that $n_e(\theta = 0) = n_o$.

In applying the diagram of the index ellipsoid it help to understand the how the SHG is generated in a uniaxial nonlinear crystal such as BBO. In Fig. A.2 we see the polarizations of the light going into the crystal and the resulting polarization output of the second harmonic generated light from the crystal.

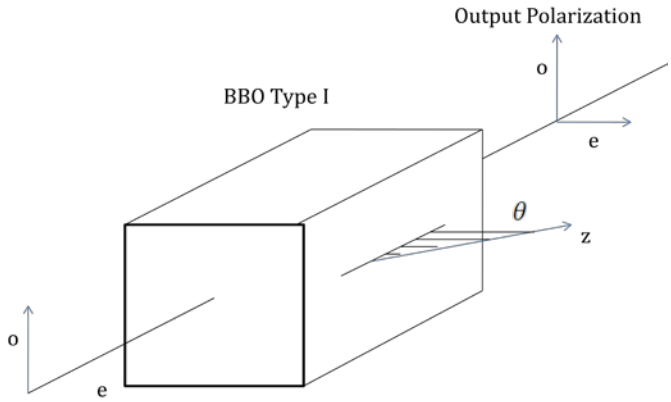

Fig A.2 Polarization of the input and output with the phase matching angle rotation in a Type I nonlinear crystal.

Reference

[99] A. Yariv, Optical Electronics in Modern Communications, 5th Ed. Oxford University, 1997